Connecting simulations of protoplanetary disks with forbidden emission lines observations

Lizxandra Flores-Rivera

Heidelberg, 2022

Dissertation

submitted to the

Combined Faculties of the Natural Sciences and Mathematics

of the Ruperto-Carola-University of Heidelberg. Germany

for the degree of

Doctor of Natural Sciences

Put forward by

Lizxandra Flores-Rivera

born in Ponce, Puerto Rico

Oral examination: November 30, 2022

Connecting simulations of protoplanetary disks with forbidden emission lines observations

Referees:

PD Dr. Mario Flock

Prof. Dr. Andreas Quirrenbach

Abstract

The big picture of the planet formation scenario is sought by understanding the interplay between the gas and dust dynamics in protoplanetary disks. In particular, the gas dynamics in accretion disks have been carefully studied in a purely hydrodynamical set up where the vertical shear instability (VSI) play a major role in the transport of the angular momentum and turbulence throughout the disk. Though, it is very difficult to directly measure the angular momentum transport, mechanisms that affect it are the launch of magneto centrifugal winds (MHD winds), outflows, and the launch of thermal photoevaporative winds. One way to pin point these processes is by identifying forbidden emissions lines in the disk spectrum and analyze their velocity components that are originating in highly ionized gas. The exact thermochemical conditions in active accreting disks that cause the emission of different forbidden emission lines is very challenging to determine. To understand such outflows, the wind launching mechanisms and their effects to the angular momentum transport require the knowledge of a full global picture of hydro- and thermal- dynamical configurations.

The work presented here covers a broad range of scenarios that are important for the evolution and dispersal of the protoplanetary disk. Our focus relies more on the dynamics and the thermo-chemistry conditions at the surface of the disk. We found that the VSI is active until the location of the wind base. The characteristic vertical velocity in this region is about a fraction of the sound speed. For the first time, we report small scale vortices appearing in VSI active disks which influence especially the dust evolution. From spectral and imaging observations obtained from the Multi-unit Spectroscopic Explorer (MUSE) instrument at the Very Large Telescope (VLT), high velocity components (HVCs; >100 km s^{-1}) are detected at the inner parts of the disks as outflows/jets that are aligned within 1 degree with respect to the outer disk. With our current and upcoming global hydrodynamical models including thermochemistry and observations, we will reveal the detailed chemical and physical conditions of protoplanetary disks with active winds at the surface.

Zusammenfassung

Um das Gesamtbild des Planetenbildungsszenarios zu erfahren, muss das Zusammenspiel zwischen der Gas- und Staubdynamik in protoplanetaren Scheiben verstanden werden. Insbesondere die Gasdynamik in Akkretionsscheiben wurde in einem rein hydrodynamischen Ansatz untersucht, bei dem die vertikale Scherungsinstabilität (VSI) eine wichtige Rolle beim Transport des Drehimpulses und für Turbulenzen in der Scheibe spielen. Obwohl es sehr schwierig ist, den Drehimpulstransport direkt zu messen, sind die Mechanismen, die ihn beeinflussen bekannt. Darunter zählen magneto-zentrifugale Winde (MHD-Winde), Ausströmungen und das Entstehen von thermischen Winden. Diese Prozesse lassen sich durch die Identifizierung verbotener Emissionslinien im Scheibenspektrum und die Analyse ihrer Geschwindigkeitskomponenten, die ihren Ursprung im hochionisierten Gas haben untersuchen. Die genauen thermo-chemischen Bedingungen in aktiven Akkretionsscheiben, welche die Emission der verschiedenen verbotenen Emissionslinien verursachen, sind sehr schwierig zu bestimmen. Um solche Ausströmungen zu verstehen, müssen wir die Mechanismen der Windauslösung und ihre Auswirkungen auf den Drehimpulstransport untersuchen, um damit ein vollständiges globales Bild der hydro- und thermodynamischen Konfigurationen zu erhalten.

Die hier vorgestellten Arbeiten decken ein breites Spektrum von Szenarien ab, die für die Entwicklung und Ausbreitung der protoplanetaren Scheibe wichtig sind. Unser Schwerpunkt liegt auf der Dynamik und der thermo-chemischen Bedingungen an der Oberfläche der Scheibe. Wir haben festgestellt, dass die VSI bis zum Ort der Windbasis aktiv ist. Die charakteristische Vertikalgeschwindigkeit in dieser Region beträgt einen Bruchteil der Schallgeschwindigkeit. Zum ersten Mal berichten wir über kleinräumige Wirbel, die in aktiven VSI-Scheiben auftreten und insbesondere die Staubentwicklung beeinflussen. Aus spektralen und bildgebenden Beobachtungen, die mit dem Multi-unit Spectroscopic Explorer (MUSE) am Very Large Telescope (VLT) gewonnen wurden, können wir Hochgeschwindigkeitskomponenten (HVCs; 100 km s^{-1}) in den inneren Teilen der Scheiben als Ausströmungen/Jets identifizieren. Damit können wir die Ausrichtung der inneren Scheibe bestimmen, welche innerhalb von einem Grad in Bezug auf die äuβere Scheibe liegt. Mit unseren aktuellen und zukünftigen globalen hydrodynamischen Modellen und den Beobachtungen, werden wir die detaillierten chemischen und physikalischen Bedingungen protoplanetarer Scheiben mit aktiven Winden an der Oberfläche aufdecken.

Contents

List of Figures

List of Tables

1 Overview of Structures in Protoplanetary Disks: Observations and Theory

"The most beautiful thing we can experience is the mysterious. It is the source of all true art and science."

by Albert Einstein

The collapse of a molecular cloud due to self-gravity is the beginning of star formation. During the rotational-collapse process in the first 0.1 Myrs, the angular momentum is conserved, where parts with low angular momentum form a protostar, while those with higher angular momentum settle into a disk in orbit around the protostar (Terebey et al., 1984). The gas and dust in the disk spiral inward through it, where a fraction of the material accretes onto the protostar (Flores-Rivera et al., 2021) and the other fraction of dust ends up onto pebbles and planetesimals to form planets (Pollack et al., 1996). The process of planet formation and the evolution of the disk has been of great interest. The work presented in this thesis will focus on a review and research on disk evolution. The relevant topics are 1) the prediction of some physical conditions processes that play an essential role in the angular momentum transport and the generation of turbulence, and 2) how it compares with the spectral observations on different protoplanetary disks.

1.1 Observations

A protoplanetary disk is a disk of hydrogen and helium (99% by mass) and dust (1%) that is orbiting the central forming star, so-called a protostar, from which planets are formed (Hogerheijde, 2011). Protoplanetary disks are classified by class based on their Spectral Energy Distribution (SEDs), in which their age, luminosity, and mass can be inferred from the excess infrared emission coming from the hot dust emitting at around 1 μm (see Figure 1.1).

The SED slope is measured between the K band (at 2.2 μm) and the N band (at 10μm) to quantify the infrared excess. Then, the spectral index is estimated, which describes the class to which the protoplanetary disk belongs. There are four types of classes: Class 0, Class I, Class II, and Class III. Class 0 objects are heavily embedded by their envelope,

where most of the infrared excess emission comes from. Class I objects are also embedded, but more features of the protoplanetary disks are seen together with outflows. In Class II, the envelope is mostly dissipated, being more transparent to see through protoplanetary disks. Class II objects are particularly interesting given that structures and substructures have been observed with high angular resolution (see, for example, Fig. 1.3). Class IIs host T Tauri stars that are named after young star systems, which were first discovered in the Taurus-forming region. The name has been adopted to describe all young systems that fall into the category of Class II, in general. T Tauri stars are less than 10 million years old and are part of the pre-main sequence stars, whose masses are a fraction of a solar mass. Protoplanetary disks have been widely observed in different classes, outside of Class II objects, in different molecular clouds. For example, in the Orion molecular cloud, there have been around 328 detections of Class 0, Class I, and flat spectrum disks that provide useful constraints about the disk properties for their formation and initial conditions for their evolution (Tobin et al., 2020). The detections of protoplanetary disks are usually based on the fit of Gaussian components that enable the measurement of the flux density, size, and orientation. Other ways of detection are possible, although they depend on the wavelength and distance of the source from the earth.

1.1.1 Dust: optical and infrared wavelength

Structures in protoplanetary disks around young stars have been imaged in infrared wavelengths by the Spectro-Polarimetric High-contrast Exoplanet REsearch (SPHERE) instrument on ESO's Very Large Telescope (VLT) in Chile. The instrument started operating in 2014, and most of the observing efforts have been dedicated to observing and characterizing protoplanetary disks. Observing at optical and infrared wavelengths can be pretty challenging due to the low contrast of the disk emission compared with the stellar host flux. For this reason, the instrument contains special techniques to handle this task. The Polarimetric Differential Imaging (PDI) in combination with extreme adaptive optics (AXO) module (Garufi et al., 2017) and the Zurich IMaging POLarimetric (ZIMPOL) (Schmid et al., 2018) are the best techniques to study the nature of the scattered light from the surface of the disk. In scattered light imaging, the stellar light is scattered off by micron-meter size dust grains, and the resulting light is partially linearly polarized (Benisty et al., 2022). The polarized state is described by the Stokes vector:

$$\vec{S} = \begin{bmatrix} I \\ Q \\ U \\ V \end{bmatrix}$$

where I is the total intensity, Q is the vertical and horizontal linearly polarization, U is the linearly polarized light rotated 45° with respect to Q, and V is the circularly polarized light. As seen in Fig. 1.2, the polarized light image shows complex structures coming from the surface of the disk. The dust is well coupled with the gas in most parts of the disk, and so their emission traces the gas structures. These images show features like inner gaps, large-scale spiral arms, broad and narrow shadows, rings and gaps, and ambient material.

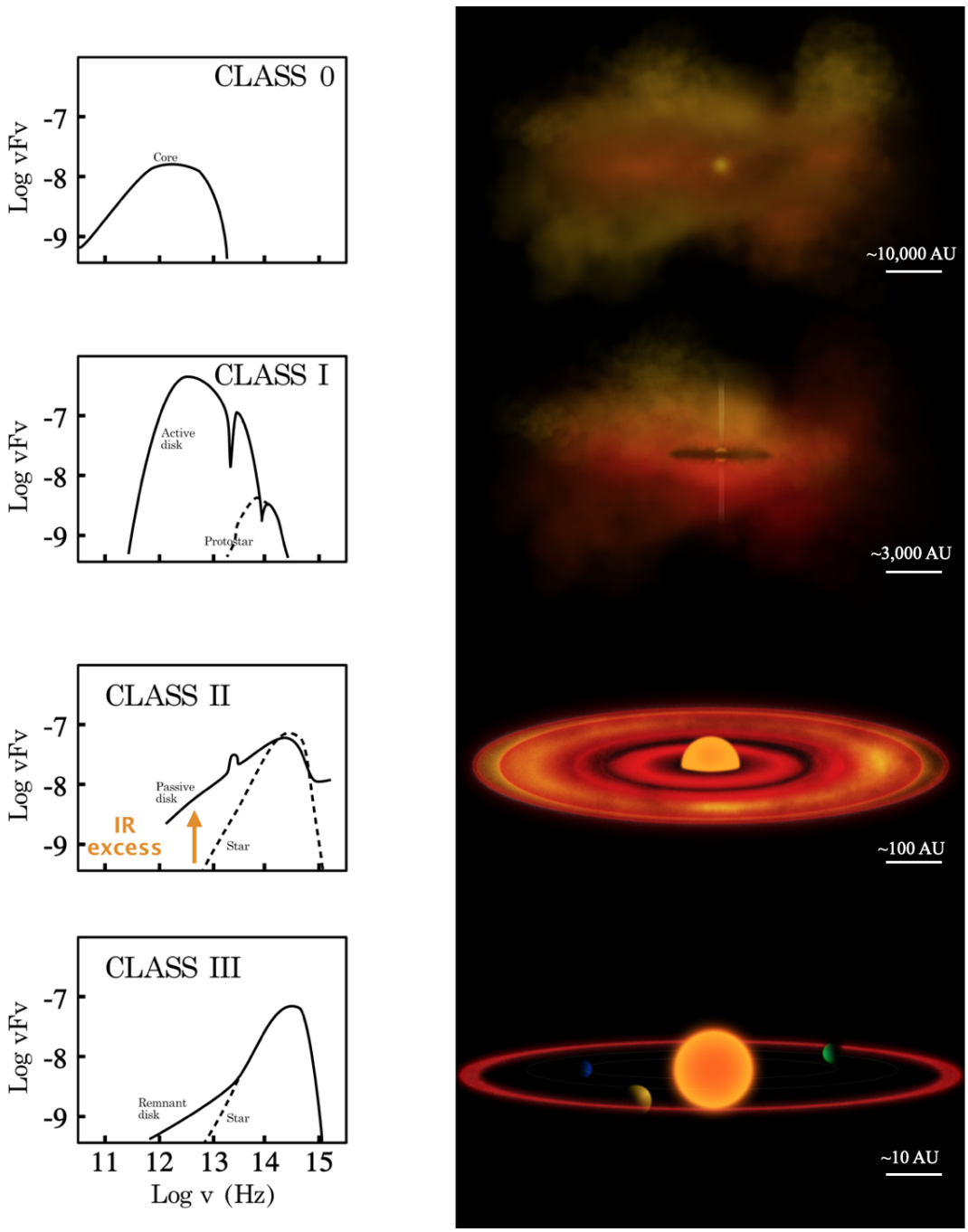

Figure 1.1: Schematic diagram of the different stages of the star and planet formation. The panels on the left represent the SEDs and, on the right, the visualization in the form of images of different stages. For a classical T Tauri star (see Class II), the peak emission of the disk occurs at just a few microns. The excess of infrared emission extends to longer wavelengths. The black dashed curve represents the black body radiation of the star.

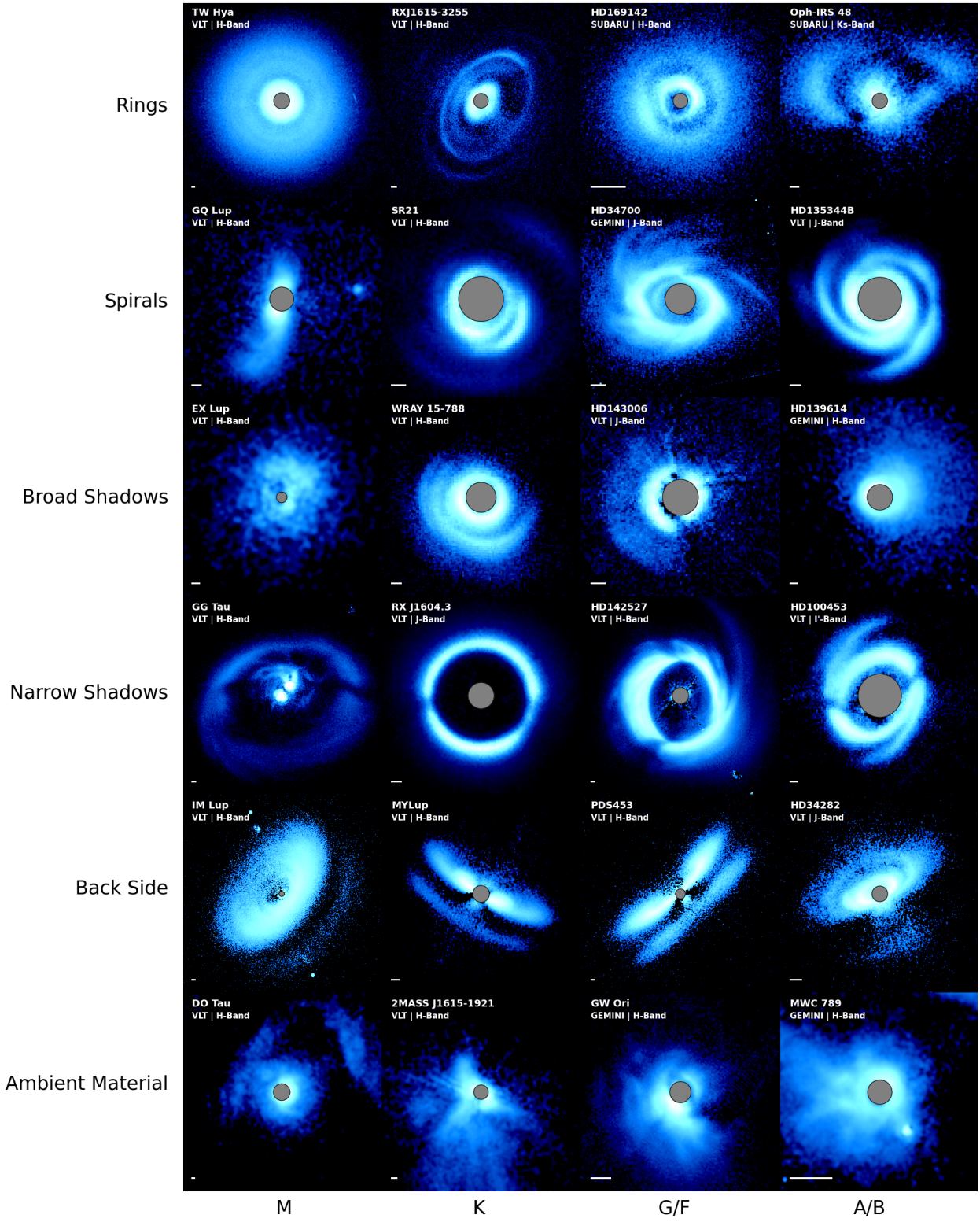

Figure 1.2: A collection of protoplanetary disks taken by SPHERE/VLT, Gemini GPI polarized data, HiCIAO, and the Subaru/HiCIAO at infrared and near-infrared wavelengths. Each column shows a different spectral type, in which morphology varies from source to source. Credit: Benisty et al. (2022) from Protostar and Planets VII.

How these structures are connected to what is happening in the midplane is not well known.

1.1.2 Dust: millimeter/sub-millimeter wavelength

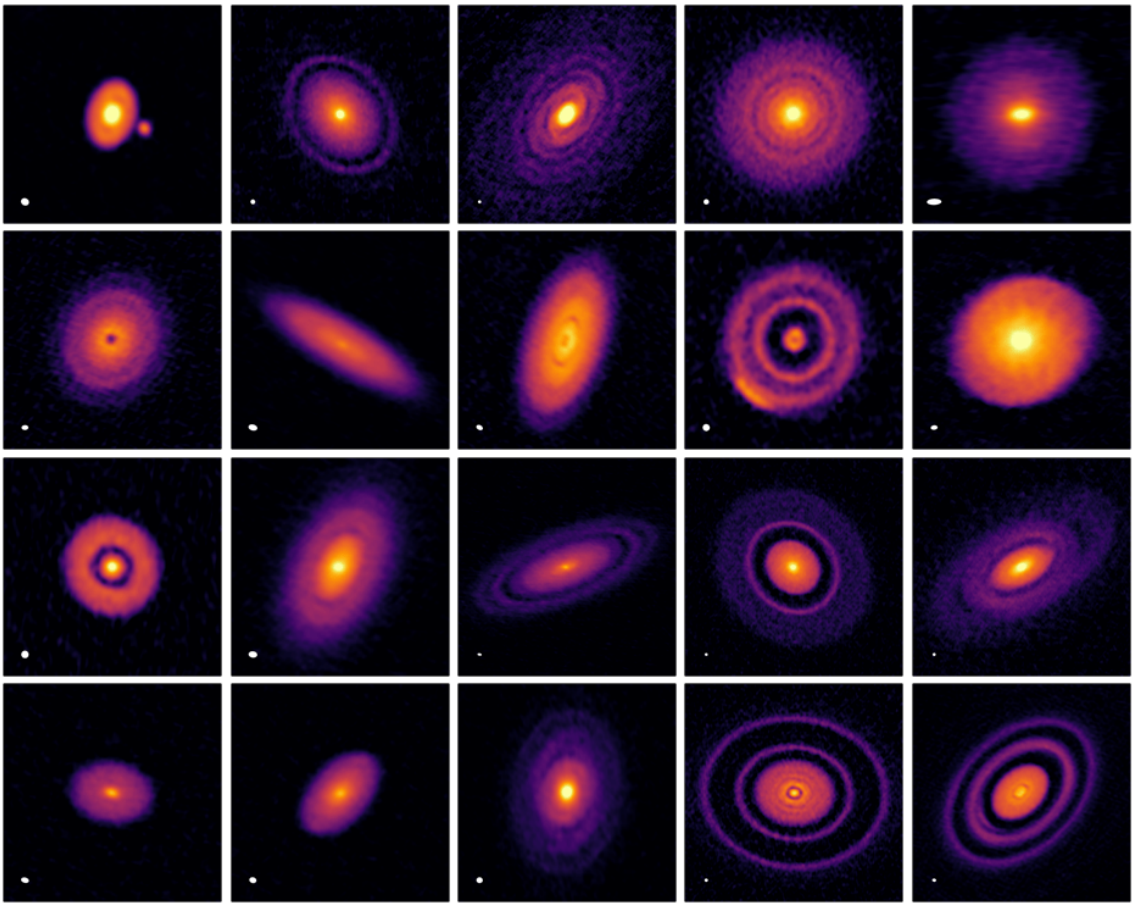

Figure 1.3: DSHARP gallery of nearby 20 protoplanetary disks with high resolution (35 mas, 5 AU) at 1.25 mm (240 GHz). Protoplanetary disks are found to have spatially distributed substructures that are relevant to the planet formation process. Credit image: ALMA Science/ESO.

Fig. 1.3 shows the dust continuum emission of different protoplanetary disks that have also been imaged in millimeter and sub-millimeter wavelengths. The Atacama Large Millimeter/submillimeter Array (ALMA) interferometer, located in Chile, has been one of the most powerful tools to assess the dust continuum that traces the midplane in protoplanetary disks. ALMA comprises 66 high-sensitivity and a high-resolution array of antennas operating at wavelengths of 3.6 to 0.32 millimeters. The array's orientation is aligned to the source's light path, and the phases and amplitudes change over time due to the rotation of Earth. A single antenna read the wavefront as pulses but an array of antennas read the visibilities over time. The light described in the visibility function, obtained from the array of antennas, is then combined by a correlator in which an average visibility response is produced. After

combining all visibilities, the visibility function is then described as the Fourier transform of the intensity of the source for a given baseline length and orientation

$$V(\vec{s}) = \iint I_\nu(\vec{s}) e^{-2\pi i \nu \vec{b}\cdot\vec{s}/c} d\Omega A(s) \tag{1.1}$$

where $I_\nu(\vec{s})$ is the source brightness along the optical path direction of the source $\vec{s}$, $\vec{b}$ is the baseline geometry, dΩ is the solid angle from where the radiation of the source is coming from, and $A(s)$ is the collecting area of each telescope in the $\vec{s}$ direction. This relationship describes the observable quantity, which is the visibility, and the quantity of interest, which is the source's brightness. The exponential term in the Fourier transform describes the fringe pattern on the sky with an angular separation of λ/b, where λ is the wavelength of the light source. In other words, the correlator multiplies the source intensity distribution of the sinusoidal fringe pattern of the sky and integrates the intensity over the sky. The fringe phase and period already sample a 2D light distribution of the source.

In 2014, at long baselines, ALMA produced a very high resolution (3.6 to 10 AU) dust continuum image of the HL Tau protoplanetary disk at 2.9, 1.3, and 0.87 mm (ALMA Partnership et al., 2015). These striking images demonstrate axisymmetric bright rings and gaps associated with high and low-density regions in the midplane. Other observations of protoplanetary disks have triggered many theoretical works about the formation of a planet interacting with the disk in evolution (Carrasco-González et al., 2016). HL Tau has also been imaged by the Very Large Array (VLA) National Radio Astronomy Observatory (NRAO) at 7 mm wavelength proving lower optical depth emission than what ALMA reproduces (Carrasco-González et al., 2016). Planet-induced scenarios seem to be likely significant to explain them. Later in 2018, the ALMA large program Disk Substructures at High Angular Resolution Project (DSHARP) was introduced to study the disk structures and substructures. With a very high angular resolution of 5 au (0.035″) at 1.25 mm, the program has found that substructures are ubiquitous and that most of them are seen as concentric and narrow emission of rings and gaps, as well as spiral arms in some samples (Andrews et al., 2018). For T Tauri sources at ∼1 Myr, the dust-based masses range between 0.01 to 0.3 $M_\odot$, although it is not the only constraint to determine the disk mass overall. Another common way to estimate the disk mass is through observations of ^{12}CO gas and isotopologues, but a challenge is raised due to the molecule depletion in the midplane.

1.1.3 Gas

Emission from molecules encodes information on the disk ionization levels, the temperature structures, the kinematics, and the gas surface density, which are all key ingredients for the disk evolution and planet formation (Öberg et al., 2021). Another large program from ALMA is the Molecules with ALMA at Planet-forming Scales (MAPS), in which observations were taken for 45 minutes to assess the relationship between dust structures and substructures and gas traced by some molecules (see Fig. 1.4).

Another two important factors when analyzing the gas content in disks are 1) to constrain the vertical structure to assess the optical depth of the molecule in the protoplanetary disk and 2) to determine how well the molecules can probe planet-forming or instability

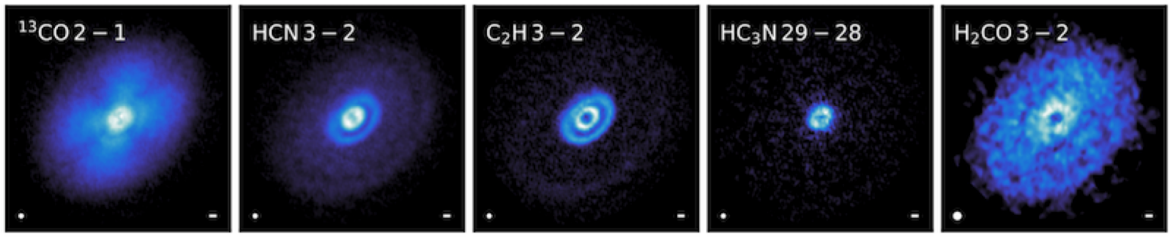

Figure 1.4: Five molecular gas tracers in HD 163296 protoplanetary disk. The observation was taken as part of the ALMA MAPS survey. As it is observed, each gas molecule show different structures like shadows, concentric gaps, and rings. Whether or not these gas structures are linked with the ongoing forming planet or any other turbulence, or if they are found in the same location as the structures we see in the dust continuum and infrared images, is not so well known. Gallery credit: Aikawa et al. (2021).

signatures. The analysis of the spatial distribution of the gas requires a good understanding of the gas time evolution, radial and vertical temperature profile, gas surface density, and ionization fraction. The variation of these constraints highly relies on chemical models and simulations describing the interaction between gas and dust. These frameworks, all together, are quite complex and computationally expensive. The gas motion in the disk is Keplerian, and the gas mass and radius could be estimated. However, not all gas emissions will trace Keplerian motions on the disk surface. Photoevaporation driven-winds, MHD winds, or planet-inducing motions can cause non-Keplerian molecular signatures across the structured disk.

Spatially and spectrally resolved line observations in the sub-millimeter regime are represented as a data cube. The data cube contains three axes: two for the spatial information containing the sky coordinates and one containing the frequency. The frequency can be converted to line-of-sight velocity via the Doppler shift formulation from its rest frequency. The maximum spectral resolution in ALMA, for example, is 30.5 kHz which translated to velocity resolution is 26 m s^{-1} and 40 m s^{-1} for the ^{12}CO J=3-2 and J=2-1 lines, respectively, where J is the rotational energy level of the molecule (Pinte et al., 2022). Nevertheless, the question is, how much can we rely on the gas dynamics to reveal what type of mechanism causes the different morphologies seen in the gas? The latter remains to be determined.

It is not a coincidence that ^{12}CO has been one of the most observed and studied molecules in the interstellar medium (ISM). It is one of the most abundant (10^{-4} relative to molecular hydrogen) and a stable molecule. It produces intense spectral emissions; therefore, it is invaluable to trace the presence of molecular hydrogen in envelopes and in protoplanetary disks. The ^{12}CO molecule has a small dipole moment and relatively small moment of inertia, so its rotational energy levels are closely spaced and easily excited at low temperatures (10-40 K) (Ward-Thompson & Whitworth, 2011). As the envelope is in the final stage of collapse, ^{12}CO is a good tracer because it is present in large amounts where a great amount of light is emitted. CO isotopologues like ^{13}CO and C^{18}O are two other common molecules, but they are less abundant (50 and 500 times less abundant than ^{12}CO, respectively). However, both molecules play an important role as they are optically thinner, probing even denser areas in the disk. Nevertheless, these molecules are depleted in the midplane right beyond the ice line.

The gas molecular structure can tell us a lot of information about the protoplanetary disk. The gas kinematics signatures could hint at the gas accretion into a planet forming, which has to be confirmed by other observational means. However, theory predicts that there could also be other mechanisms that can produce characteristic motions similar to what we could depict from gas accretion into a planet. Hydrodynamical instabilities and photoevaporation processes are two examples that we aim to explore in this work. The following chapters will show how these two mechanisms are critically important for the evolution of the disk.

1.1.4 Challenges

Previous observations show that protoplanetary disks vary widely in size and shape. They also differ depending on their orientation in the sky – from face-on to edge-on disks. Protoplanetary disks contain gas, dust, and potentially kilometer-size rocks called planetesimals that are building blocks of planets. The formation and evolution of planets take at least 12 orders of magnitude in spatial scale, from micrometer to kilometer size particles. The dust dynamics during the evolution of the planet, as the dust growth via coagulation, differs from that of the gas dynamics. It is thought that for a T Tauri disk, the forming planets are formed by planetesimal-like bodies that are massive enough to be decoupled from the gas and have small bodies gravitationally accreting onto it. It is extremely challenging to follow the observational constraints of planetesimals and planets since their scattered surface brightness is relatively small compared to the surface brightness that the disk emits. For this reason, the disk generally outshines the planet that is forming within it. Identifying point sources as planet candidates require high-contrast imaging observations with high angular differential techniques (Keppler et al., 2018) and other observational tools. There has been only one direct imaging detection with SPHERE/VLT of a forming planet (PDS 70b) in a transition disk named PDS 70 (Keppler et al., 2018). Later on, another planet companion, PDS 70c, was found in the same system, clearing out dust from the inner edge of the ring (Isella et al., 2019), and just recently Benisty et al. (2021) detected with high resolution ($\sim$20 mas, 2.3au) with ALMA a circumplanetary disk (CPD) around PDS70c. These discoveries have been supported by spectroscopy observations, in particular, by the Hα detection, which confirmed that such planets are still accreting material around their CPDs (Haffert et al., 2019).

Although planet-disk interaction simulations predict that a planet of a certain mass causes disk structures, there can certainly be other mechanisms that also play an important role not only in the gas structures but also in the gas dynamics that is mainly responsible for transporting the angular momentum. Turbulence is one of the key factors that leads the angular momentum transport, and it is thought that turbulence origins from different instabilities. The velocity field in the disk is mainly dominated by Keplerian motion, shown as a 'butterfly' shape in the channel maps from the data cubes. The deviations from Keplerian motions in the channel maps are visualized as 'velocity kinks.' These could indicate deviations in the meridional flow, e.g., by spiral wakes. The explanations for these deviations are pointed to possible gas accretion onto the planet. However, are planets (if not confirmed) the only cause of non-Keplerian motions in the gas? What else can we say about turbulence triggered by instabilities? Constraining the turbulence caused by instabilities is quite difficult since to look at the broadening that turbulence can cause, it requires resolutions close to the limit

of 30 kHz ($\sim$40 m s^{-1} at 230.538 GHz). These are needed to resolve the spectral emission line from molecular gas in disks (Pinte et al., 2022), and it is quite possible that it is not mutually exclusive from other physical scenarios happening simultaneously in the disk.

Other limitations are how the emission line is imaged; perhaps the development of new and different techniques and better fitting models are required to better localize non-Keplerian deviations from the gas. For example, precise velocity information can be nicely obtained by fitting moment maps one with EDDY (Teague et al., 2018a,b), or by fitting channel maps using statistical techniques (Izquierdo et al., 2021). These two techniques, in the end, attempt to fit the best disk values, such as stellar mass and disk inclination. Another important technique is to get a good fit of the surface emission of the disk, but in order to achieve this, good spatial resolution is needed. For optically thick molecules, such as ^{12}CO, it could often happen that there is cloud contamination, meaning that there could be foreground extinction hiding the true disk gas emission.

1.2 Disk model theory

Briefly, this section will focus on how models treat the geometrical structure of the disk. An important distinction when deriving the physical properties of a Classical T Tauri protoplanetary disk is that the stellar luminosity irradiates them. At the early stages of star formation, at Class 0 and Class I, the disk is actively generating internal energy from accretion stress. For a Class II disk, the typical mass accretion of the disk is 10^{-6} - 10^{-12} M$_\odot$ yr^{-1} (Pascucci et al., 2022). The next section will revise the conditions for an accretion disk to balance the gravity and the pressure force.

1.2.1 Vertical and radial hydrostatic equilibrium

The vertical profile of the gas density for the disk model is determined under the condition of vertical hydrostatic equilibrium. The conditions for the hydrostatic equilibrium are

- The disk is geometrically thin with a $H_R/R \ll 1$.
- The gas is supported by pressure.

The forces acting on the disk are the pressure and the gravity from the star. For simplicity, the hydrostatic equilibrium equations are represented in cylindrical coordinates to show later the temperature and the density profile solutions as a function of cylindrical radius. The force balance in the **vertical direction** is

$$F_Z = \frac{dP}{dZ} = -\rho g_Z \tag{1.2}$$

where ρ is the gas density and g_Z is the acceleration in the vertical component. The vertical force acting on the gas including the radial and vertical contribution can be written

as

$$F_Z = \vec{\nabla}\phi_Z = -\frac{GM_\star Z}{(R^2+Z^2)^{3/2}} \tag{1.3}$$

where G is the gravitational constant, $M_\star$ is the mass of the star, Z and R correspond to the vertical and radial cylindrical components, respectively. If we assume that the disk is thin, meaning that $z << R$, then $g_z = \frac{GM_\star}{R^3}Z$. It can be noted that the term $\sqrt{\frac{GM_\star}{R^3}}$ correspond to the Keplerian angular velocity, Ω_k.

Following the same prescription but in the **radial direction**, the hydrostatic equilibrium equation is

$$F_R = \vec{\nabla}\phi_R = -\frac{GM_\star R}{(R^2+Z^2)^{3/2}} \tag{1.4}$$

and is also balanced with the centrifugal force

$$F_{\mathrm{c}} = \frac{v^2}{R} = R\Omega_k^2 \tag{1.5}$$

Then, the equilibrium forces can be solved by equating both

$$\textbf{vertical forces:} \qquad -\frac{GM_\star Z}{(R^2+Z^2)^{3/2}} - \frac{1}{\rho}\frac{dP}{dZ} = 0$$

$$\textbf{radial forces:} \qquad R\Omega_k^2 - \frac{GM_\star R}{(R^2+Z^2)^{3/2}} - \frac{1}{\rho}\frac{dP}{dR} = 0$$

Considering the previous assumption that the disk is passive and thin, we can treat the equation of state as isothermal. Adopting an isothermal gas equation of state is an important equilibrium condition because it is used to describe the equilibrium solutions of the density and the angular velocity, Ω_k, profiles. For an isothermal configuration, the pressure

$$P = \rho c_s^2 \tag{1.6}$$

where c_s^2 is the constant sound speed. An isothermal configuration means that the gas is treated locally where the temperature is constant along the vertical direction, but in the radial direction, the temperature profile reads

$$T(R) = T_0\left(\frac{R}{R_0}\right)^q \tag{1.7}$$

and the midplane density

$$\rho_{mid}(R) = \rho_0 \left(\frac{R}{R_0}\right)^p \tag{1.8}$$

are power-law dependent on the disk radius. The q and p are the power-law fitting exponents for the temperature and the density, respectively. The isothermal sound speed is related to the temperature as $c_s^2 \sim T \sim \left(\frac{R}{R_0}\right)^q$. The profile of the density and azimuthal rotation in hydrostatic equilibrium are

$$\rho(R,Z) = \rho_0 \left(\frac{R}{R_0}\right)^p \exp\left(\frac{GM}{c_s^2}\left[\frac{1}{\sqrt{R^2+Z^2}} - \frac{1}{R}\right]\right), \tag{1.9}$$

$$\Omega(R,Z) = \Omega_k \left[(p+q)\left(\frac{H_R}{R}\right)^2 + (1+q) - \frac{qR}{\sqrt{R^2+Z^2}}\right]^{1/2}, \tag{1.10}$$

where H_R is the disk scale height (see §1.2.2 for more details). The **vertical forces** and **radial forces** equations are two first order differential equations, and the equilibrium solutions given in equation 2.3 and equation 2.4, represent the accretion disk in equilibrium. The same solution equations are shown in Nelson, R. P. and Gressel, O. and Umurhan, O. M. (2013).

1.2.2 Disk scale height

The disk scale height is a scaling parameter. It depends on the temperature (equation 1.7) and on the Keplerian angular velocity. The scale height first appears when solving the vertical pressure gradient force (equation 1.2), where the scale factor inside the exponential term is on the form of $H_R = c_s/\Omega_k$, where $\Omega_k = \sqrt{\frac{GM_\star}{R^3}}$. The disk scale height can also be compared with the disk thickness to the radius

$$h = \frac{H_R}{R} = \frac{c_s}{v_\phi}, \tag{1.11}$$

where $v_\phi = \sqrt{\frac{GM_\star}{R}}$, is the local orbital velocity. As mentioned before, since the c_s is related to the power-law function of the radius, then the disk shape will depend upon the disk scale height (equation 2.5). For a flared disk, the h will increase with radius. The power-law fitting exponent, q, is around -0.5 for passive disk models or around -1.0.

1.3 Turbulence and the angular momentum transport

After deriving the solutions for a passive accretion disk in equilibrium, now it is extremely important to understand its dynamical evolution. In order to agree with observations, physical models focused on mechanisms that would distribute the angular momentum thoroughly

in the disk. The idea behind this concept has a foundation in conserving angular momentum in the disk. In accretion disks, most potential energy is converted to kinetic energy that is then dissipated into heat by the effective viscosity; therefore, the disk angular momentum is lost. Because the angular momentum in the disk must be conserved, the loss of angular momentum in the inner disk must be compensated by increasing the angular momentum outwards in the disk. Shakura & Sunyaev (1973) proposed that turbulence can provide an effective viscosity.

1.3.1 Turbulent viscosity

An isotropic turbulence on scale of h, can be characterized as viscosity (Shakura & Sunyaev, 1973),

$$\nu = \alpha c_s h, \tag{1.12}$$

where α is a constant that measures how efficient the turbulence is transporting angular momentum (Armitage, 2007). It was proposed that magneto-rotational instability (MRI; Balbus & Hawley (1991)) in regions where the gas is highly ionized was the main source of turbulence in the disk. The MRI is a linear instability and applies to magnetic field lines in the ionized gas. The MRI has been found to lead to turbulence, effectively transporting angular momentum outwards in the disk. To better explain this dynamic process, let us assume that two gas parcels in the disk are connected by a massless spring that would represent the magnetic field tension. In the rotating accreting disk, the inner gas parcel would move faster than the outer gas parcel, causing the spring to stretch out (magnetic tension increases). The spring then forces the inner gas parcel to slow down, reducing its angular momentum and causing the inner gas parcel to move to a lower orbit. In contrast, the outer gas parcel is pulled forward and sped up, increasing its angular momentum, causing the outer gas parcel to move to a higher orbit. An obstacle sets in wherever there are low ionization parts ("dead zones") in the disk. Low ionization limits the conductivity necessary for the magnetic field to couple to the disk. Such consequence leads to non-ideal MHD effects such as ambipolar diffusion, Hall effect, and Ohmic resistivity. These non-ideal MHD effects will suppress the MRI turbulence leaving the space for hydrodynamical instabilities to take over turbulence in the disk (Lesur et al., 2022).

In the dust, best fit models of dust settling and vertical mixing in the disk model have been used to describe the turbulence (for example, Pinte et al. (2016)). With this method, the α has been found to be 10^{-4}. This is a reasonable approach; however, the α is assumed to be constant vertically. Although constant α is an acceptable approximation for T Tauri sources, there are no physical reasons why α should be constant vertically throughout the disk.

The other way to constrain α is by determining the turbulent diffusivity from the dust structures seen in mm wavelengths. For example, the radial width of the rings has been used to describe the turbulent mixing of particles inside the rings (Dullemond et al., 2018). The turbulent mixing is responsible for stirring up the dust particles, opposing radial concentration at the gas pressure maxima. The turbulent mixing parameter is related to α viscosity as α/Sc, where Sc is the Schmidt number that describes the ratio between the turbulent vis-

cosity and the turbulent diffusivity. The Schmidt number is usually taken to be Sc=1, which is a reasonable value to compare with DSHARP ALMA images, that found α to be 10^{-4} but larger values are more consistent with the data (Johansen & Klahr, 2005; Dullemond et al., 2018). Both methods previously mentioned should be treated carefully as it is not known exactly how and what turbulent sources generate an effective turbulent diffusivity (see Zhu et al. (2015)).

In 3D hydrodynamical simulations of the gas in protoplanetary disks, the effective alpha viscosity is rather measured from the Reynolds stress-to-pressure ratio

$$\alpha_{r\phi} = \frac{\int T_{r\phi} dV}{\int P dV} = \frac{\int \rho v_r' v_\phi' dV}{\int \rho c_s^2 dV} \tag{1.13}$$

Note that the Reynolds stress-to-pressure ratio depends on the velocity perturbation in the radial and azimuthal components. For observations of the gas, the α turbulent parameter is determined by measuring the broadening of the molecular line that depends on the temperature, gas density, and abundance distribution. The α viscosity of the gas, using 3D simulations to resolve for the VSI (see §1.4 for more details), is estimated to be around 10^{-4} (Barraza-Alfaro et al., 2021) which is fair to compare it with the effective viscosity that is derived from dust continuum best-fit models. Barraza-Alfaro et al. (2021) also found that when post-processing the 3D hydro simulations with radiative transfer predictions and synthetic observations, the VSI produces observational features in CO kinematics that are observable with ALMA. Furthermore, Blanco et al. (2021) predicted dust substructures undergoing VSI and concluded that the next generation Very Large Array (ngVLA; Murphy et al. (2018)) would have the potential to resolve these structures with a resolution of $\sim$1 au. In 2D, there could be a way to get an effective viscosity similar to equation 1.13 but instead considering the velocity perturbations in the radial and vertical direction to get $\alpha_{r\theta}$ from VSI. Manger et al. (2020) attempted to obtain an α viscosity including all 3D components and found that the α viscosity is $\alpha \sim 10^{-3}$ for a high disk scale height ($H_R/R = 0.1$) and $\alpha \sim 10^{-5}$ for a low disk scale height ($H_R/R = 0.03$). However, this interpretation should be taken carefully as vertical perturbation does not transport material outwards but instead lift them. This could have very important implications for photoevaporative winds launching at the surface of the disk.

1.3.2 The loss of angular momentum

The gas dynamics in accretion disks have been carefully studied both in a purely hydrodynamical setup (Nelson, R. P. and Gressel, O. and Umurhan, O. M., 2013) and in configurations where the magnetic field governs the evolution of the gas (Lesur et al., 2014). In either case, the angular momentum transport is effectively determined based on the turbulence level that instabilities, as previously mentioned, trigger in accretion disks. However, the angular momentum transport does not stay constant infinitely. In fact, in accretion disks, the angular momentum is lost via the launch of magneto centrifugal winds (MHD winds), outflows, jets, and the launch of thermal photoevaporative winds. One way to pinpoint these processes is by identifying forbidden emissions lines in the disk spectrum and analyzing their velocity components originating in the highly ionized gas.

The innermost part of the disk ($\sim 0.5-5$ AU) is strongly influenced by stellar radiation. The stellar radiation is characterized by Extreme Ultra Violet (EUV; 13.6 eV $< h\nu <$ 100 eV), Far Ultra Violet (FUV; 6 eV $< h\nu <$ 13.6 eV), and X-ray ($h\nu >$ 100 eV). The column density describes how deep these stellar photons penetrate the disk. The column densities, determined based on the frequency-dependent cross-sections, of EUV goes until 10^{19} cm^{-2} and the FUV/X-ray penetrate deeper until 10^{20-22} cm^{-2} (Nakatani et al., 2018a,b) at temperatures that can reach beyond 6,000 K (Simon et al., 2016). The FUV photons ionize the gas, the most common elements, and molecules, up to levels of ion abundances of 10^{-4} relative to H nuclei. FUV ionization is not tied to heating rates. The FUV heating rate is well coupled to the ejection of electrons via photo-electric processes from small dust grains (size of a few μm) (Pascucci et al., 2022). This makes the small dust a key ingredient for generating disks winds. Deeper in the FUV/X-ray layer (close to the midplane), FUV can provide additional heating due to electrons collisions by de-excitation of H_2 from energy levels $n = 2-1$ (Hollenbach et al., 1994; Pascucci et al., 2022). EUV photons can boost wind launching since they are the main precursors of heating in the disk upper atmosphere. X-ray photons are also important for winds and are more associated with stars actively accreting and having a high chromospheric activity.

Each of the mechanisms provides heat into the gas emitting the forbidden emission lines as we see in the spectra have origin depending on the thermochemistry, temperature, and gas density of the inner parts of the disk. Starting with jets, they show high-velocity components (HVC; 100 km s^{-1}), and their origin relies more on the stellar-radiation activity and star-disk interaction, where an MRI plays an important role (Ferreira et al., 2006; Armitage, 2011; Flock et al., 2017). Disk winds are very likely to happen during the jet launch.

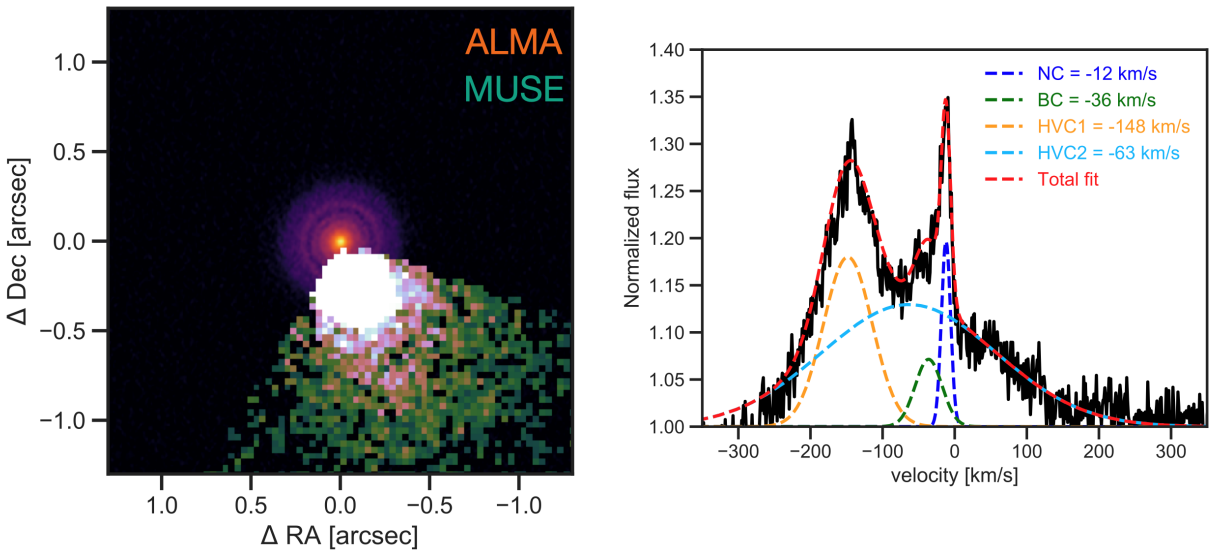

Figure 1.5: *Left.* Composite image of the RU Lup dust continuum at 1.23 mm (Huang et al., 2018a) and superimposed is the [OI]λ6300 taken by MUSE/VLT. Currently the MUSE data for this source is been analyzed by Birney et al. *inPrep.* Dashed grey lines show the north, position angle measured from the dust, and position angle measured from the jet/outflow. *Right.* High-resolution spectral data from Banzatti et al. (2019) of RU Lup showing complex line profiles. Each component (NC=Narrow Component, BC=Broad Component, and HVCs=High Velocity Components) show its centroid velocities associated with different disk dispersal mechanisms.

1.4 Hydrodynamical instabilities

Hydrodynamical instabilities are thought to be responsible for generating turbulence in accretion disks. The Reynolds stress measures the total stress or turbulent velocity fluctuations and the sound speed in the fluid momentum. This said, evaluating the level of turbulence in hydrodynamical instabilities highly relies on numerical simulations.

1.4.1 Linear stability for hydrodynamical disk models

The linear regime of the instability can be studied from the analytical perturbational analysis. The standard condition for linear hydrodynamical stability in a fluid that is rotating with Keplerian angular velocity is called the Rayleigh criterion, which establishes that the disk is hydrodynamically stable if (Goldreich, P. and Schubert, G., 1967; Nelson, R. P. and Gressel, O. and Umurhan, O. M., 2013)

$$\frac{d(R^2\Omega_k)}{dR} > 0, \tag{1.14}$$

For a Keplerian rotating disk, $R^2\Omega_k \sim R^{1/2}$ and the fluid is linearly stable according to the Solberg-Høiland criteria (e.g., Rüdiger, G. et al. (2002)). This means that for vertical

and radial gradients, the stability condition must satisfy

$$\frac{\partial(R^2\Omega_k)^2}{\partial R}\frac{\partial S}{\partial Z} - \frac{\partial(R^2\Omega_k)^2}{\partial Z}\frac{\partial S}{\partial R} > 0, \tag{1.15}$$

where S is the entropy of the system. This means that the stability of Keplerian rotating disks requires two conditions: 1) a positive vertical entropy gradient, $\frac{\partial S}{\partial Z} > 0$, and 2) a negative radial entropy gradient, $\frac{\partial S}{\partial R} < 0$, that balances the angular momentum gradient. By taking into account that the disk is thin ($H_R/R < 1$), then equation 2.4 gives $\frac{\partial R^2\Omega_k}{\partial Z} \sim q(\frac{H}{R})\frac{\partial R^2\Omega_k}{\partial R}$. Inserting the latter equation into equation 1.15 gives $\frac{\partial S}{\partial Z} - q(\frac{H}{R})\frac{\partial S}{\partial R} > 0$. The stability criteria satisfy

$$\frac{\partial S}{\partial Z} < q\left(\frac{H}{R}\right)\frac{\partial S}{\partial R}, \tag{1.16}$$

This condition tells us that a non-zero vertical shear can give rise to turbulence throughout the disk. This is the "**vertical shear instability**" or the VSI and is characterized as the upward and downward velocity perturbations operating in regions where the radiative cooling time scale is relatively short (Nelson, R. P. and Gressel, O. and Umurhan, O. M., 2013). It was first referred to the Goldreich-Schubeert-Fricke instability of differential rotating stars (Goldreich, P. and Schubert, G., 1967; Fricke, 1968). There has been a lot of interest in the last decade about how this instability could potentially be one of the main drivers of turbulence, therefore, angular momentum transport in the disk.

The potential level of turbulence caused by the VSI have important implications to the evolution of the disk. However, some people have carefully studied the VSI and found that the main characteristics of the VSI are: 1) it is present in short relaxation timescales, 2) it requires a vertical gradient of the rotational velocity, and 3) it produces a stress-to-pressure of $\alpha = 10^{-3}$ to $\alpha = 10^{-4}$ (Urpin, 2003; Arlt & Urpin, 2004; Stoll & Kley, 2014a; Barker, A.J. and Latter, H.N., 2015; Stoll & Kley, 2016; Lin & Youdin, 2015; Umurhan et al., 2016a). High resolution (≥ 50 cells per H_R) simulations have found the VSI to operate throughout the entire disk until reaching out turbulent regions where the heated boundary layer at $H_R = 6$ is located (Flores-Rivera et al., 2020). Figure 1.6 shows the VSI present in the disk as corrugated-shape structures resembling the body modes (the non-linear growth phase) where the VSI is most turbulent.

1.4.2 Other hydrodynamical instabilities

In the absence of MRI, other hydrodynamical instabilities can be present as well. These include

- *Subcritical Baroclinic Instability (SBI).*
  Baroclinic instability refers to the process where the gas density is subject to instability driven by the temperature and pressure gradients. It is subcritical because it refers to non-linear instability. The growth of this instability depends on the kinetic energy that is drawn from the initial thermal perturbation that results in a generation of a

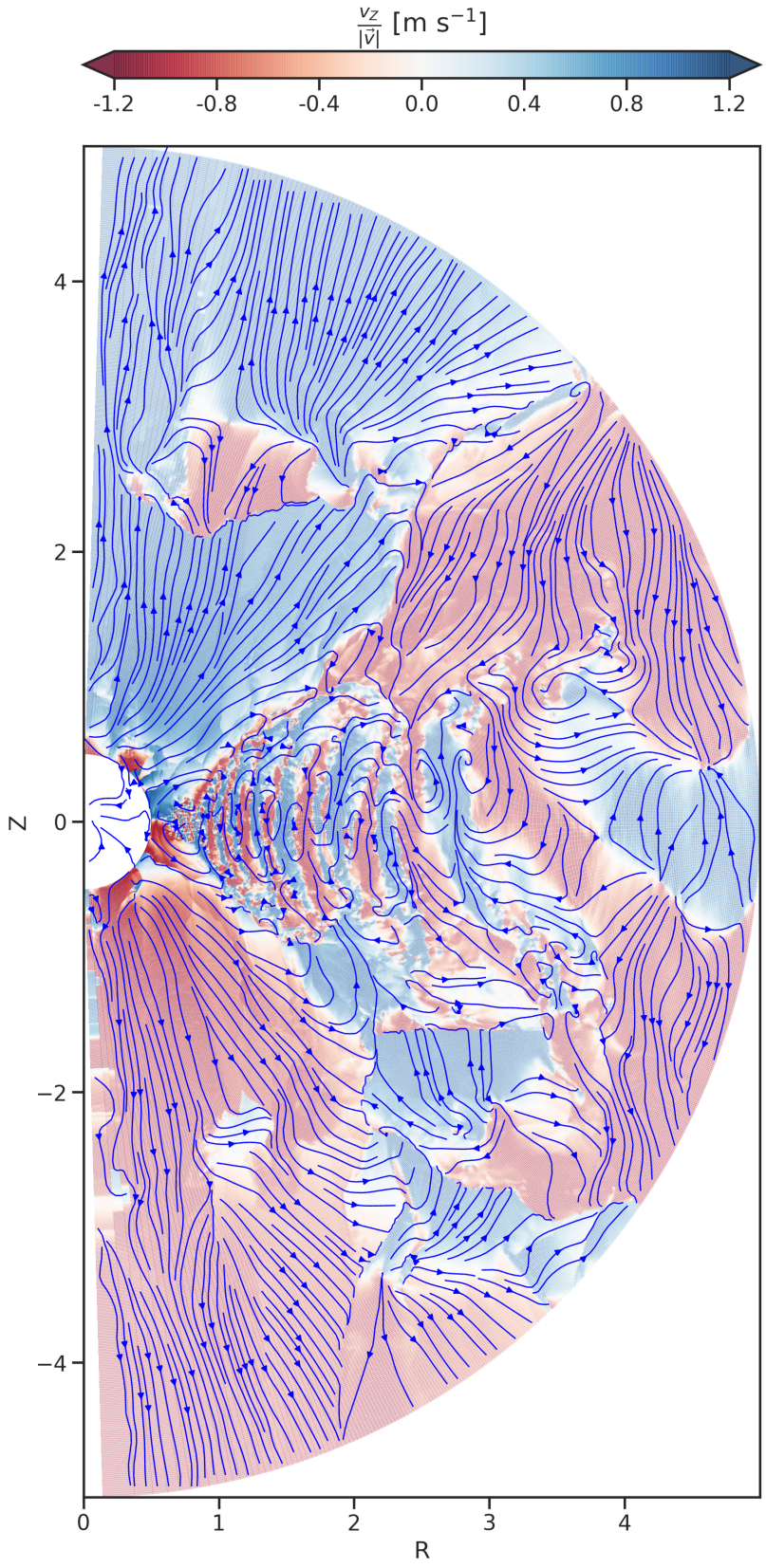

Figure 1.6: A high-resolution snapshot of the meridional velocity normalized to the magnitude of the velocity at 200 orbits highlighting the upward and downward velocity perturbations (blue streamlines) associated with the VSI.

vortex (Lesur & Papaloizou, 2010; Petersen et al., 2007). Vortices are particularly important because they have been observed already in some protoplanetary disks. They can transport angular momentum and trap particles into their core that could go under the formation of pebbles and eventually planetesimals (Barge & Sommeria, 1995). However, they can go under disruption caused by other instabilities (Barranco & Marcus, 2005; Lesur & Papaloizou, 2009; Lithwick, 2009).

- *Convective Overstability (COS).*
  It is a linear instability that depends on the radial entropy in rotating stabilized disks. Like the SBI, it is also driven by thermal diffusion that is described as radial convection epicycles (small circles whose centers move around the circumference of a larger one). After a thermal perturbation is initially applied, the gas parcel goes under half an epicycle and returns to the initial radius but at a different temperature than its surroundings. At the same time, the gas parcel experience acceleration due to buoyancy, amplifying the initial oscillation (Klahr & Hubbard, 2014; Pfeil & Klahr, 2020).

- *Zombie Vortex Instability (ZVI).*
  The ZVI (Marcus et al., 2015; Umurhan et al., 2016b) is a non-linear instability that depends on the dust size and gas properties such as the opacity (Barranco et al., 2018). In principle, it can operate at a disk scale height greater than 1.5, where the dust is thermally decoupled from gas, with a thermal relaxation that allows vertical internal gravity waves to start operating the formation of ZVI (Pfeil & Klahr, 2020).

- *Vertical Convective Instability (VCI)*
  The VCI arises due to the superadiabatic vertical temperature stratification caused by the internal heating from the effective viscosity (Pfeil & Klahr, 2020). It does not drive angular momentum transport itself, but the vertical convection could release some α viscosity, but it requires a stable temperature gradient (Klahr, 2007). The vertical buoyancy generated by this instability supports the growth of the VSI, which is important for disk stability.

1.4.3 Streaming instability

Another substantial instability in Keplerian disks is the Streaming Instability (SI). The SI is thought to be one of the main precursors of planet formation. The formation of SI occurs when there is a combination of radial dust drift and sufficient drag between dust and gas, leading to a spontaneous concentration of dust clumps that can eventually collapse gravitationally (Youdin & Goodman, 2005). The growth rate for the SI depends on the local dust-to-gas mass ratio and radial drift of solids in the rotating disk (Armitage, 2015; Squire & Hopkins, 2018; Pan & Yu, 2020; Flock et al., 2020). This instability has been studied in local shearing box (Goldreich & Lynden-Bell, 1965; Yang & Johansen, 2014; Yang et al., 2017) and then in quasi-global simulations (Flock & Mignone, 2021). The analysis for the SI considers a vertical unstratified system in which a gas interacts with a particle fluid via gas-dust drag (Armitage, 2015).

The first section shows that protoplanetary disks observed in scattered light, millimeter, and centimeter wavelengths show different structures and substructures. The connection

between disk structures seen at different wavelengths is pretty challenging (see Fig.1.7). The initial process that leads to high-density regions or initial pressure dust clumps of small particles is suspected to be caused by the SI.

1.4.4 Planet formation scenarios

- via core accretion

The theory of the core accretion scenario proposes how in a high-density region, the dust agglomerate grows and develops into a small core made of heavy elements (Pollack et al., 1996). In a way, the formation of the core is analogous to the formation of the core of rocky planets. This is what the first phase of the core accretion scenario is. The dust growth can result through the coagulation process from small particles or through collision by pebbles or small planetesimals (a few meters in size). In this theory, the core is assumed to accrete planetesimals only, but small bodies could significantly contribute to core growth as well (Ormel & Klahr, 2010; Chambers, 2014; Lambrechts & Johansen, 2012). As the planetary core evolves, all the dust and gas around it will form a local envelope or a cloud where all the material within it is subject to the formation of the potential gravitational field of the planetary core. When the solid core is massive enough, let us say the mass of the rocky core is slightly approximated to the mass of the envelope, then the runaway gas accretion by gravity happens. As the gas in the envelope cools down, the envelope contracts, and the runaway gas accretion (where the accretion is mostly my gas) is eventually halted when there is no more gas to accrete around the planetary core. However, when the runaway gas accretion is halted is not fully known as it requires some disk dispersal mechanisms (Bergez-Casalou et al., 2020).

- via fragmentation

The other way planets can form via disk fragmentation. In this case, the disk has to be massive enough ($> 10\%\ M_{\odot}$) or, in other words, gravitationally unstable to form a clump of cold gas that eventually becomes a self-gravitating planet (Cameron, 1978; Kuiper, 1951). A condition for a disk to be gravitationally unstable must satisfy that the Toomre parameter, Q, is low enough, specifically,

$$Q = \frac{c_s \Omega_k}{\pi G \Sigma} < Q_{crit.} \sim 1 \tag{1.17}$$

where Σ is the local surface density. For $Q = 1$, the $\Sigma = 1.5 \times 10^3$ g cm^{-2} at 10 au and $H_R/R = 0.05$, a value that is much larger than the estimates for the minimum mass Solar nebula (Armitage, 2015). Protoplanetary disks are suspected of going under gravitational instability at their earliest epoch of formation when the mass of the disk is comparable with the mass of the star. Gammie (2001) determined the time that the disk would go under fragmentation by adjusting the cooling timescale for a star ($t_{cool} = \frac{U}{2\sigma T_{disk}^4}$) as the control parameter in the simulations. This expression is analogous to the Kelvin-Helmholtz time that is needed to radiate away a great amount of thermal energy, U, from the star. Its been found that the boundary for fragmentation is when $t_{cool} \leqslant 3\Omega^{-1}$. This said, spiral arms resulting from the disk self-gravity compress patches of gas in the disk on a timescale that is to orders of magnitude Ω^{-1} (Armitage, 2011).

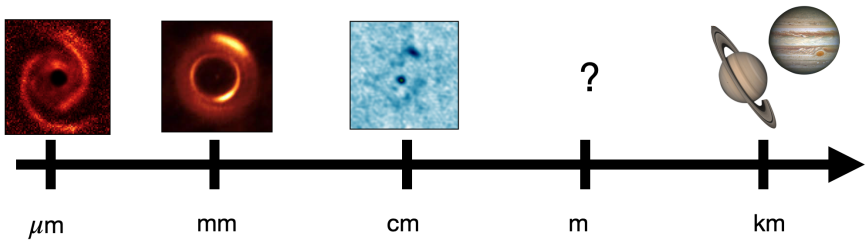

Figure 1.7: MWC 758 disk observed at different wavelengths showing different morphologies. An indication of dust growth is seen in the cm wavelength as a dark spot in the northwest part of the disk. The images are not on scale. SPHERE polarized scattered light disk image credit: Benisty et al. (2015), ALMA 0.87mm dust continuum disk image credit: Dong et al. (2018), and VLA at 345 GHz disk image credit: Casassus et al. (2019).

1.5 Motivation

The chemical state of the gas, which describes the line cooling and emission, and sets the gas temperature in the disk, is highly influenced by the stellar photons at the surface of the disk. The photoevaporative winds, one of the main agents of disk dispersal, are potentially launching in regions where the photoelectric heating and photo-ionization caused by EUV, FUV, and X-ray are the dominating reactions. The work presented here intends to sort the interplay between the VSI activity, responsible for transporting angular momentum, with photoevaporative winds. It is still not well described how photoevaporation winds affect the extraction of angular momentum. We aim to establish how to set the thermochemical conditions that cause the emission of different atomic or molecular gas tracers of disk winds. Understanding how the mass is lost via photoevaporative winds and its role in angular momentum transport requires the knowledge of a complete global picture of hydro- and thermal- dynamical configurations. Figure 1.8 shows an excellent artistic visualization of the focus of this thesis, emphasizing different regions in the disk.

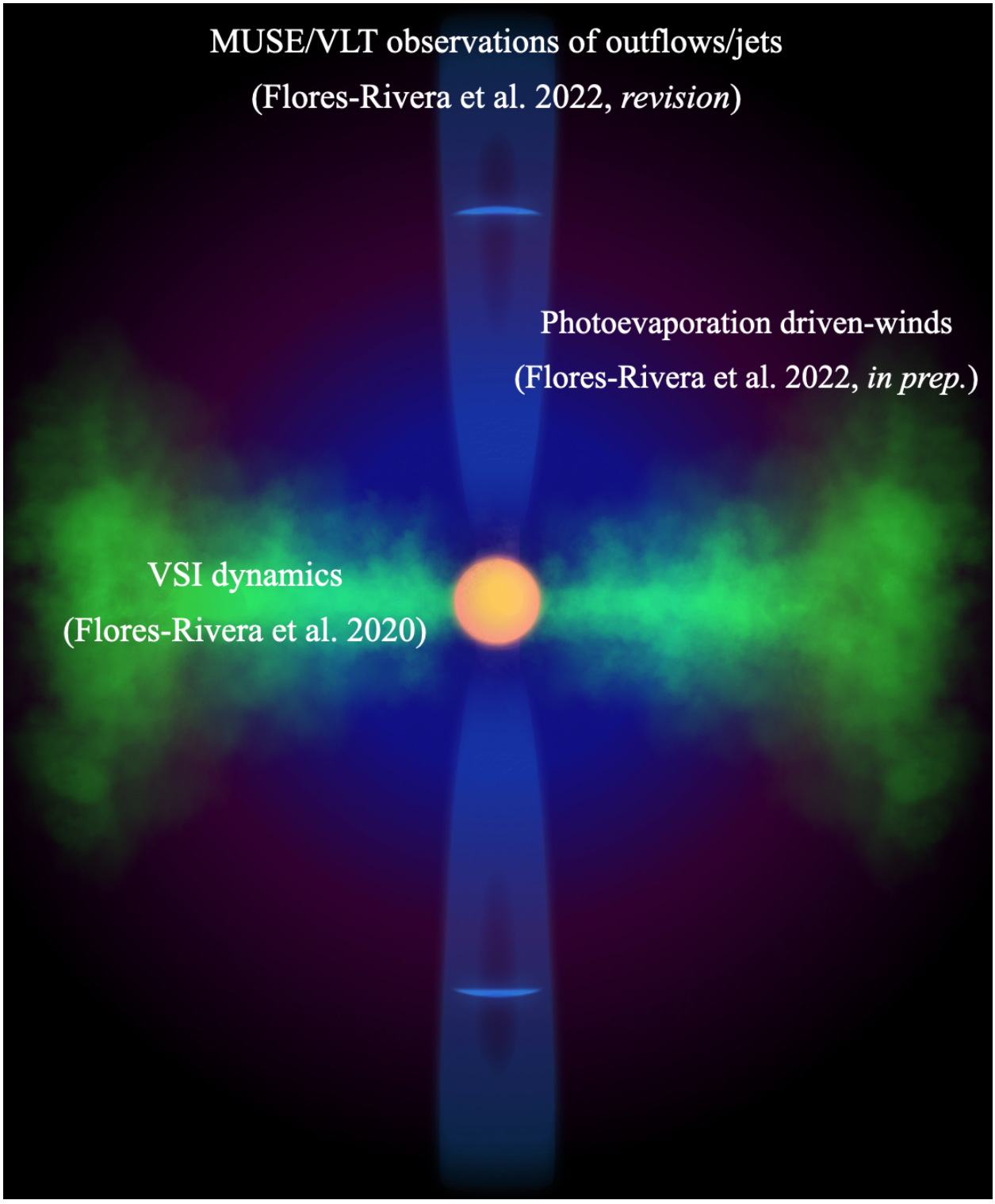

Figure 1.8: Artistic representation of the focus of this thesis. The T Tauri star is at the center, where the influence stellar photons appear as blue and purple color halos in the background. The green shaded region resembles the gas density, and the bipolar collimated outflow/jet appears in light blue.

2 Disk Dynamics and the Vertical Shear Instability

"*Science is a way of thinking much more than it is a body of knowledge*"

by Carl Sagan

2.1 Context

Hydrodynamical (HD) simulations in protoplanetary disks have gained substantial attention during the last decades. Due to the low coupling between the magnetic field and the gas in a large fraction of the disk (Turner et al., 2014; Dzyurkevich et al., 2013) we expect that HD instabilities play a more important role in the gas kinematics and the overall gas evolution in protoplanetary disks. In theory, the presence of vertical shear instability (VSI) (Goldreich, P. and Schubert, G., 1967; Fricke, 1968) in purely HD accretion disks has been well studied by careful perturbational analysis and numerical simulations in several works (e.g., Nelson, R. P. and Gressel, O. and Umurhan, O. M. (2013); Stoll & Kley (2014b); Barker, A.J. and Latter, H.N. (2015); Lin & Youdin (2015)). Several works have shown the importance of this instability to explain the turbulence and angular momentum transport in the disk (Arlt & Urpin, 2004; Nelson, R. P. and Gressel, O. and Umurhan, O. M., 2013; Stoll & Kley, 2014b). The main ingredients of the VSI are a short thermal relaxation timescale and a vertical gradient of the rotational velocity in the disk. However, the effect of the VSI together with realistic thermal profiles in the disk are not well known. The evolution of the VSI has been tested in the context of planet formation and disk evolution. Recent simulations conducted by Lin (2019) have found that the VSI can be suppressed by dust settling and grain growth; however, the streaming instability (SI) may be present when VSI is active in the turbulent disk (Schäfer et al., 2020a). In the context of disk evolution its been proposed that photoevaporation by energetic photons is a potential agent of disk dispersal (e.g., Shu et al. (1994); Hollenbach et al. (1994); Clarke et al. (2001); Owen et al. (2012); Alexander et al. (2006a,b, 2014); Ercolano & Pascucci (2017)). Investigating the effect of high-energy radiation on protoplanetary disks can be quite complex, but recent efforts have attempted to explain the effect of high-energy radiation onto the disk through observations of winds (e.g., Ercolano et al. (2008); Gorti et al. (2009); Owen et al. (2010, 2011)). A

prominent signature of photoevaporation processes is the detection of forbidden lines in the protoplanetary disk spectrum. The detection of the NeII line from the surface of TW Hya at around 10 AU (Pascucci et al., 2011), shows the important influence of high-energy photons on the surface layers of the disk; however, the vertical extension of the wind is still quite inconclusive. Moreover, Ballabio et al. (2020) found the synthetic line profile of NeII to be consistent with thermally driven winds, while other forbidden molecules such as OI, OII, and SII require a different scenario, possibly magneto driven winds (Fang et al., 2018; Banzatti et al., 2019). A photoevaporative process in the inner disk (< 5 AU) has been tested by Wang et al. (2019) and Gressel et al. (2020) that considered hydromagnetic diffusive effects, thermochemistry, and ray-tracing radiative transfer, but the wind description in terms of the Keplerian rotation and mass loss rate is different. Gressel et al. (2020) determine that the deviation of the winds caused by the magneto-centrifugal mechanism are super-Keplerian, while Wang et al. (2019) found it to be sub-Keplerian. The mass loss in Gressel et al. (2020) is $\sim 10^{-7} M_\odot$ yr^{-1}, whereas Wang et al. (2019) is $\sim 10^{-8} M_\odot$ yr^{-1}.

The coexistence between the VSI and photoevaporation processes by stellar photons is of particular interest, especially in regions where we expect a steep temperature profile and fast thermal relaxation timescales, which few have found that the VSI might operate down to ∼1 AU (e.g., Klahr et al. (2018); Lyra & Umurhan (2019); Pfeil & Klahr (2019, 2020)). The effect of viscous heating in the disk remains relatively small, making it plausible to use passive irradiated disk models to accurately represent the thermal structure (Flock et al., 2019). As a first step towards including photoevaporation processes in our HD simulations, our aim in this first paper is to study the convergence, the strength, and the region where the VSI operate in the disk, using the full meridional domain.

2.2 PLUTO

We performed our HD simulations using PLUTO 4.3[1] by Mignone (2007). The dynamics of the fluids is described by the conservation laws accounting for the divergence of mass density and momentum density. The HD fundamental equations in our setup are

$$\frac{\partial \rho}{\partial t} + \nabla \cdot (\rho \mathbf{v}) = 0, \tag{2.1}$$

$$\frac{\partial (\rho \mathbf{v})}{\partial t} + \nabla \cdot (\rho \mathbf{v}\mathbf{v}) + \nabla P = -\rho \nabla \Phi, \tag{2.2}$$

where ρ is the mass density, $\mathbf{v}$ is the velocity vector, $\rho\mathbf{v}$ is the momentum density vector, and P is the gas pressure. We select the isothermal equation of state with $P = c_s^2 \rho$, where c_s is the isothermal sound speed. The code solves consistently the HD equations in a 2D geometry and considers the system in spherical coordinates (r, θ, ϕ) with axisymmetry in the azimuth. The grid cells are set up with a logarithmic increase in the radial domain and a uniform spacing in $\cos(\theta)$ for the meridional domain (e.g., Ormel et al. 2015) in order to have a better resolution around the midplane layers. The simulations are scale free. We set

the radial domain extending from 0.5 to 5.0 and the vertical domain covering approximately 180°.

2.2.1 Disk model and boundary conditions

Protoplanetary disks, rotating with Keplerian angular velocity and vertical stratification are dynamically stable according to the Solberg-Høiland criteria (e.g., Rüdiger, G. et al. (2002)). The accretion disk setup in equilibrium in cylindrical coordinates (R, Z) was first described in Nelson, R. P. and Gressel, O. and Umurhan, O. M. (2013), also introduced in equation 2.3 and in equation 2.4, and are defined as

$$\rho(R,Z) = \rho_0 \left(\frac{R}{R_0}\right)^p \exp\left(\frac{GM}{c_s^2}\left[\frac{1}{\sqrt{R^2+Z^2}} - \frac{1}{R}\right]\right), \tag{2.3}$$

$$\Omega(R,Z) = \Omega_k \left[(p+q)\left(\frac{H_R}{R}\right)^2 + (1+q) - \frac{qR}{\sqrt{R^2+Z^2}}\right]^{1/2}, \tag{2.4}$$

where $\rho_0 = \frac{\Sigma_0}{\sqrt{2\pi}\ H_0\ R_0}$=4.5×10^{-10}g cm^{-3} = 2.7×10^{14} cm^{-3} is the initial density at the midplane, and Σ_0 is the initial surface density (see Table2.1), R_0 is the reference radius, H_0 is the reference scale height, G is the gravitational constant, M is the mass of the star, p is the power-law fitting exponent of the density profile, and $\Omega_k = \sqrt{GM/R^3}$ is the Keplerian frequency. The disk scale height in terms of the radius is

$$H_R = H_0 \left(\frac{R}{R_0}\right)^{(q+3)/2}, \tag{2.5}$$

where the reference scale height ratio is $H_0/R_0 = 0.1$ (see Table 2.1) and c_s is related to the temperature through the power-law fitting exponent q. The radial profile of c_s is given based on eq.2.5 so that c_s=$H_R\ \Omega_k$. The scale length of the vertical mode is proportional to H_0.

In order to compute the fluxes in each cell, we employ second-order piece-wise linear spatial reconstruction. This reconstruction method is appropriate for both uniform and non-uniform grid spacing based on the approach presented in Mignone (2014). We use the Harten, Lax, Van Leer (HLL) Riemann solver. For the time integration we adopt a second-order Runge-Kutta algorithm and we set the Courant-Friedrichs-Lewy (CFL) number to 0.25. Table 2.1 summarizes the model parameter and the different runs for each resolution. For 101 and 203 cells per H_R, the θ inner limit is shifted slightly inwards due to the high computational precision issue when increasing the resolution at the θ boundary. We also use the third-order piecewise parabolic method (PPM3) reconstruction method to compare with the linear reconstruction method analysis. The PPM3 results show that the configuration

*PLUTO 4.3 is an open source code available for download:
http://plutocode.ph.unito.it/download.html

is not stable yet, therefore, we focus our VSI analysis using the linear method. In §2.4.1 we demonstrate a preliminary result using this method.

Table 2.1: Grid setup and initial parameters for the different runs.

$N_r \times N_\theta \times N_\phi$	Δr $[AU]$	$\Delta\theta$ $[AU]$
256 × 256 × 1	0.5:5	0.001:3.1405
512 × 512 × 1	0.5:5	0.001:3.1405
1024 × 1024 × 1	0.5:5	0.001:3.1405
2048 × 2048 × 1	0.5:5	0.01:3.1315
4096 × 4096 × 1	0.5:5	0.02:3.1216
Initial parameters		
p	-1.5	
q	-1.0	
R_0	1.0	
H_0	0.1	
Σ_0 [g cm^{-2}]	1700	

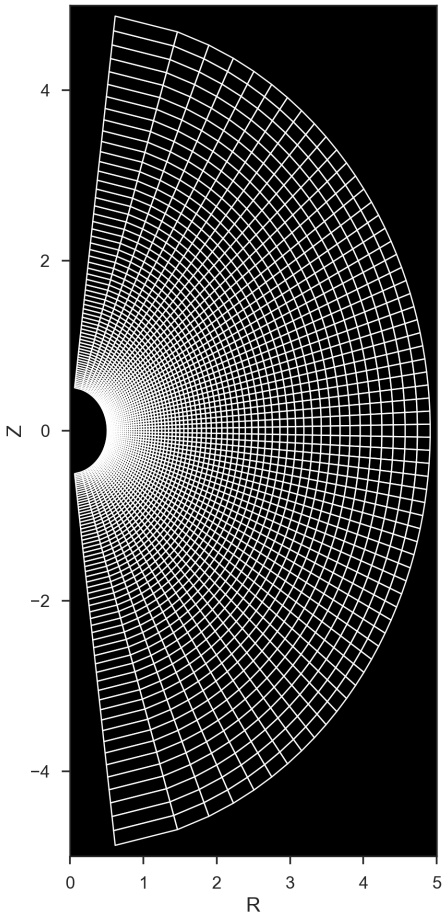

Figure 2.1: Our grid set up in PLUTO.

2.3 EUV, FUV, and X-ray column density

The inner parts of the disk are highly influenced by the stellar radiation potentially ionizing the upper layers of the disk. As a first step to implement photoheating processes caused by stellar EUV, FUV, and X-ray photons, we calculate the radial column density locally to predict at what scale height the EUV and X-ray–FUV heated layers are most dominant. The radial column density is calculated by integrating the hydrogen nuclei column density along the radial line of sight

$$\Sigma_r(r) = \int_{R_*}^{r} n_\rho dr, , \tag{2.6}$$

where R_* is the star radius and n_ρ is the number density of hydrogen nuclei. For this first paper in the series, since we do not consider detailed chemistry or the frequency of UV photons, we determine the boundaries in terms of Σ_r by post-processing. We focus on the definition of the radial column density to locate the boundary of the ionized region (EUV heated region) and the neutral layer (X-ray–FUV heated layer) which is empirically determined from the simulations of Nakatani et al. (2018a,b). We select the boundary between the ionized or EUV heated region, namely the H–H^+ boundary, to be located at Σ_r=10^{19} cm^{-2}, assuming the EUV stellar luminosity is $\sim 10^{30}$ erg s^{-1}. The EUV heated region typically has temperatures of orders of magnitude between 10^3 to 10^4 K and the hydrogen is fully ionized here. The boundary of the X-ray–FUV heated layer is defined at Σ_r=10^{22} cm^{-2}, where the gas is heated to 10^3 K and it dominates in the neutral layers. While soft X-rays are considered to be an important component for photoevaporation, the locations of FUV and X-ray heated layers are nearly identical $\Sigma_r \leq 10^{21-22}$ cm^{-2} (Gorti & Hollenbach, 2008; Nakatani et al., 2018b). Therefore, setting the boundary of the neutral photo-heated layer at $\Sigma_r \leq 10^{21-22}$ cm^{-2} is valid even in cases where X-rays effects are included. The surface density analysis for the determination of the EUV heated region and X-ray–FUV heated boundary layer are shown in Figure 2.2. Overplotted are the contour lines tracing the radial column density for the two regions of interest. It should be noted that we neglect scattered light in our ray-tracing. For more information about the effects of stellar photons and the launch of winds, see §2.5.1 and §2.5.2.

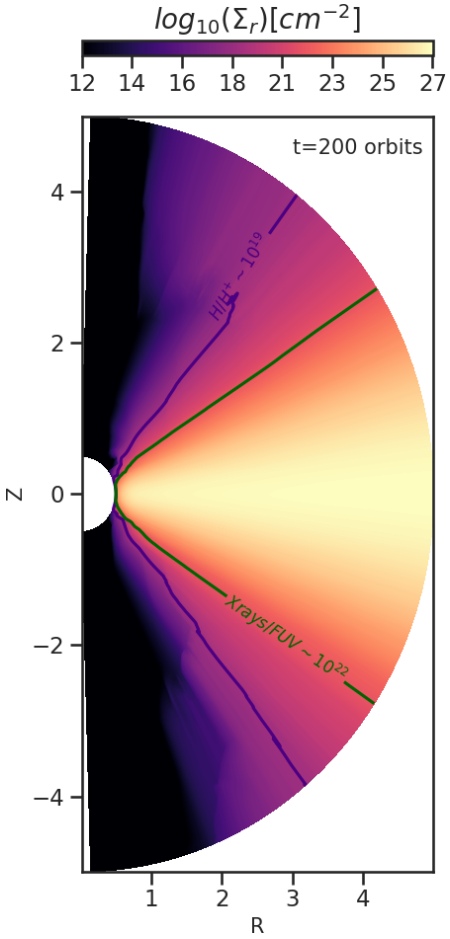

Figure 2.2: Radial column density in cm^{-2}. Overplotted are solid lines where Σ_r=10^{19} cm^{-2} represents the EUV heated region (in purple), and Σ_r=10^{22} cm^{-2} represents the X-ray–FUV heated boundary layer (in dark green).

2.4 Gas dynamical evolution

In order to investigate the kinematics we start by looking at the time evolution of the kinetic energy. Figure 2.4 shows the average kinetic energy at different grid cell resolutions. Our prescription of the global kinetic energy follows

$$E_{kin} = \frac{1}{2}\int_v \rho v_Z^2 dV, \tag{2.7}$$

where v_Z= $v_r$cos(θ) - $v_\theta$sin(θ) is the vertical component of the velocity and E_{kin} is normalized with respect to

$$E_{norm} = \frac{1}{2}\int_v \rho v_k^2 dV, \tag{2.8}$$

where v_k is the Keplerian velocity. Due to our large global domain, it becomes necessary to transform our spherical velocity components to cylindrical when describing the vertical kinetic energy. For the resolution analysis we simulate a large parameter space, starting from 12 cells per scale height until 203 cells per scale height. At the lowest resolution we observed that the VSI is not resolved as the kinetic energy is not growing (see Fig.2.4). We observe that the initial perturbations are damped and the kinetic energy is decreasing leading to a fully laminar disk. For resolutions higher than 12 cells per scale height, the growth seen at $\geq$25 orbits is characteristic of the initial increase phase of the kinetic energy as the disk become unstable to the VSI, as found by Nelson, R. P. and Gressel, O. and Umurhan, O. M. (2013). The 25 cells per scale height case is often used in the literature as a standard resolution to perform global simulations. However, we note that this resolution does not fully solve the VSI in accretion disks. It reaches an energy saturation slightly lower than 10^{-5}, and after that it starts to increase monotonically without reaching a steady state, at least within the first 200 orbits. Because it is characteristic for all resolutions, the first energy saturation $\sim 10^{-5}$ is a consequence of the linear phase of the instability spreading throughout the system. The second phase of increasing kinetic energy might be related to the slower growth of the body modes that start to become visible after 25 orbits, when the quickly growing finger modes have already saturated. During this second phase, the body modes grow in the disk until they reach saturation after around 90 orbits. Our results show that at a resolution of about 100 cells per scale height the kinetic energy levels converge. For even higher resolutions, which are computationally very expensive, we predict the same convergence trend.

Our total kinetic energy follows the same trend as the perturbed kinetic energy from Nelson, R. P. and Gressel, O. and Umurhan, O. M. (2013). The resolution for the VSI used by Cui & Bai (2020) lies between 96 and 108 cells per scale height, which is in good agreement with our resolution study as well. Figure 2.3 shows a snapshot of the three main physical quantities in our analysis: the number density, the vertical velocity, and the kinetic energy in physical units. Overplotted are the contour lines in which the EUV heated region and the X-ray–FUV heated boundary layer are defined, based on our definition of Σ_r (§2.3).

The density (Fig.2.3 panel (a)) has a smooth profile until it reaches the upper layers. Our density floor starts to become important at $H_{\rm R}$=13, which lies in a region where we do not expect VSI activity. As expected, the FUV photons penetrate deeper than EUV photons within the first 5 AU (Fig.2.3). The X-ray–FUV heated layer and EUV heated region reach $H_{\rm R} = 6.2$ and $H_{\rm R} = 9.7$, respectively. At this photoevaporation region we predict that HI regions become optically thick against EUV with a Σ_r=10^{19} cm^{-2} to Σ_r=10^{22} cm^{-2} (Fig.2.2).

The profile of the vertical velocity (Fig.2.3 panel (b)) shows clearly the upward motion shaded in blue and the downward motion shaded in red. In this region, the vertical velocity reaches a fraction of the sound speed.

The kinetic energy profile (Fig.2.3 panel (c)) shows the highest concentration present as corrugated wavy structures resembling the body modes in the disk. In the next section we investigate this in detail from a more local perspective.

We have investigated the characteristic radial wavelength in terms of scale height for the lowest and highest resolution. Fig. 2.5 and Fig. 2.6 shows the radial profile of the vertical velocity in terms of the sound speed. We determine approximately the characteristic radial wavelength by measuring the mean distance between consecutive VSI wavelength depicted

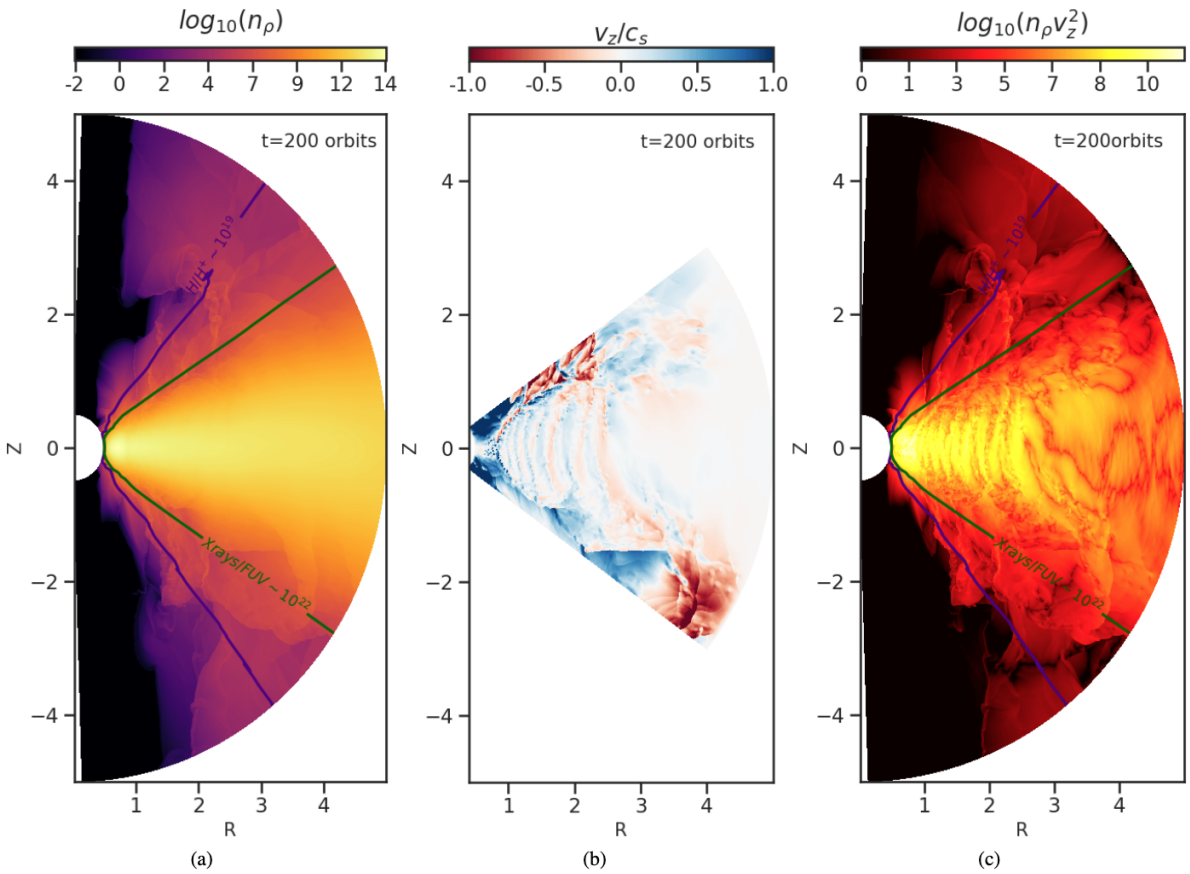

Figure 2.3: Snapshot of the three main global variables in the simulation. Panel (a) shows the number density in cm^{-3}. Panel (b) shows the vertical velocity normalized with respect to the sound speed. For better visibility of the midplane region, we show only an extent of $\pm 53°$ with respect to the midplane. Panel (c) shows the vertical kinetic energy in g cm^{-1} s^{-2}. Overplotted are contour solid lines where the column density of the EUV-heated region is defined by Σ_r=10^{19} cm^{-2} (in purple), and the column density of the X-rays/FUV-heated boundary layer is defined by Σ_r=10^{22} cm^{-2} (in dark green). The number density of hydrogen nuclei at the H/H$^+$ boundary is $\sim 10^9$ cm^{-3} and at the X-rays/FUV-heated layer is $\sim 10^{12}$ cm^{-3}.

in blue. For the 25 cells per scale height, the mean wavelength is 2.8 H_R and for the 203 cells per scale height, the mean wavelength is around 0.7 H_R.

2.4.1 Piecewise Parabolic Method

We investigated the PPM3 spatial order of integration (Colella & Woodward, 1984) using third-order Runge-Kutta (RK3) for the time integration for all resolution cases. We found that the PPM3 could resolve the VSI for even lower resolutions; however, our PPM3 configuration is currently is not yet stable. For high resolution, the preliminary results can be seen in Fig. 2.7.

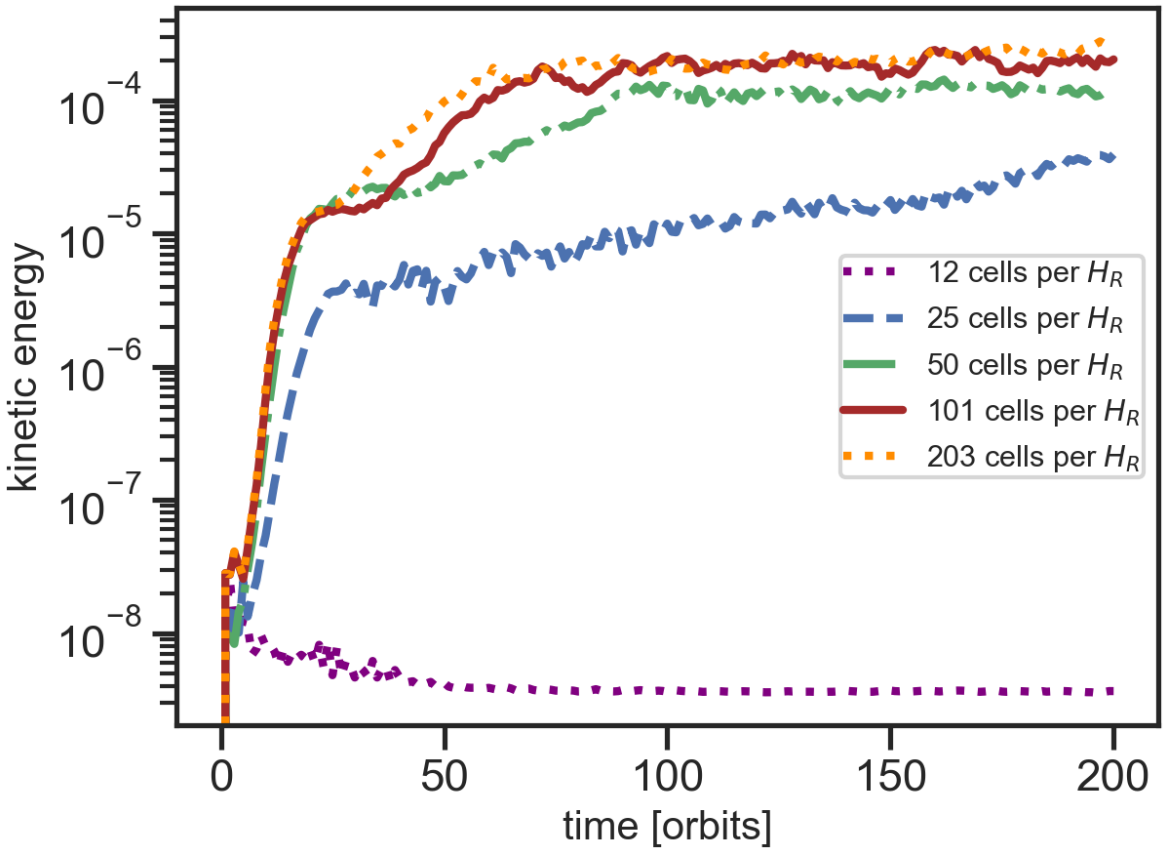

Figure 2.4: Time evolution of the kinetic energy for different resolutions and space averaged at $R_0 = 1$ AU. The kinetic energy is normalized with the kinetic energy from pure Keplerian velocity. The different resolutions are color-coded (see inset).

2.4.2 Local kinetic energy over height and time

We show the time-evolution of the kinetic energy over H_R at R_0 in Fig.2.8. We transform the velocity vectors to cylindrical and, in order to see the local kinetic energy in a more continuous spatial structure, we then use a cubic method to interpolate the data on a new grid space with a Z direction between -1 and 1 AU at R_0. Figure 2.8 shows that the kinetic energy within few first orbits represents the fast growth of the finger modes in the upper layers of the disk, which is expected. At the midplane, there is no VSI activity since the vertical shear vanishes right at the midplane. Once the body modes grow, the large-scale velocity perturbations threaten the upper and lower hemisphere. At this stage the kinetic energy at the midplane also grows.

Two important features are depicted from all resolution cases in Fig.2.8. The first is the presence at the beginning of vertical lanes of kinetic energy. We refer to these vertical kinetic energy lanes as finger modes, and they are consistent with the linear energy increase phases from Fig.2.4. The second feature corresponds to the appearance of the body modes. As seen in Fig.2.8, the growth rate of the body modes increases with resolution. For the 203 cells

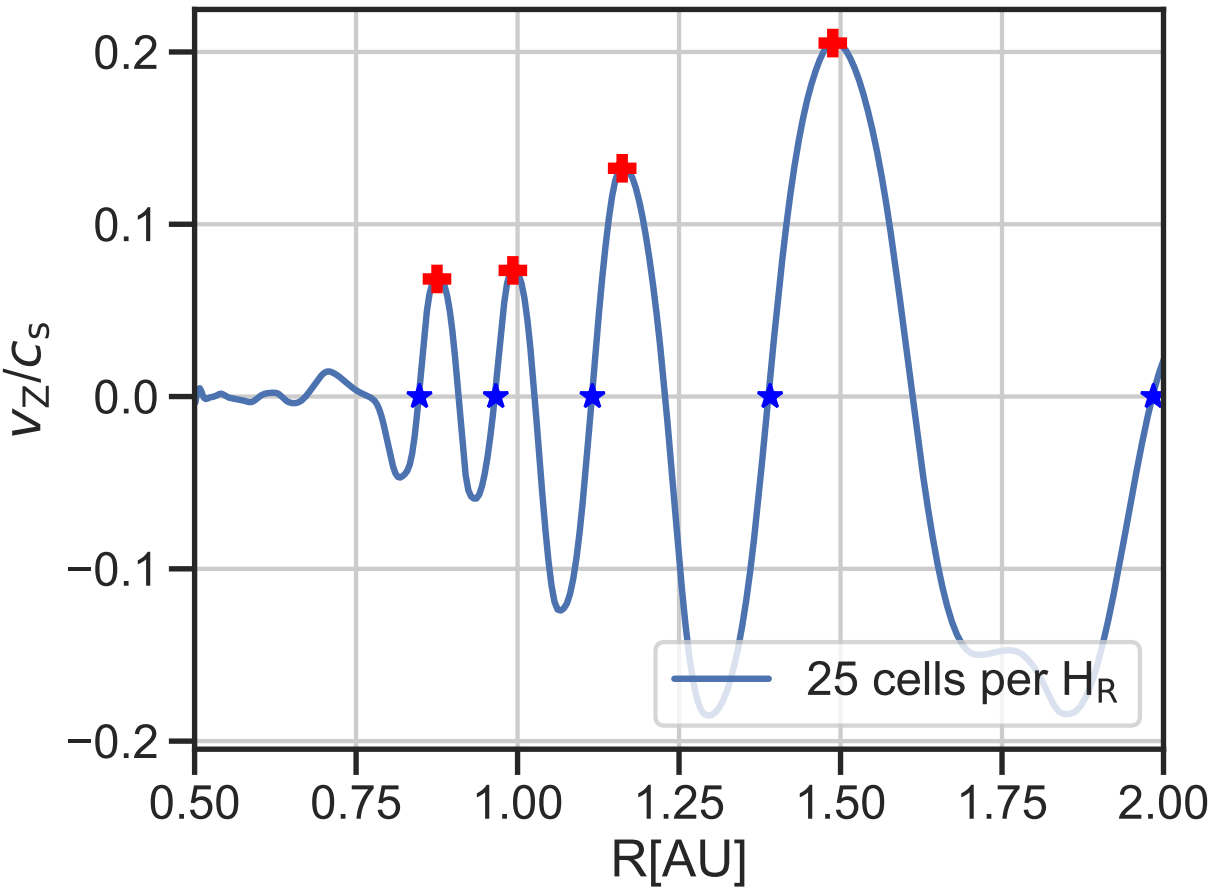

Figure 2.5: Radial profile of the vertical velocity in terms of the sound speed for the 200 orbits. The size of the VSI modes are specified in blue and the amplitude in red. We focused in the radial scale of the linear regime to determine the approximate radial wavelength of the VSI flow.

per scale height, the body modes saturate at around ∼70 orbits. At H_R=0 (midplane), the kinetic energy is very low but even more detailed analysis in the midplane is performed in the last paragraph.

Figure 2.9 shows the time averaged vertical profile of the kinetic energy. The vertical profile follows a trend similar to that of the density profile. Only for the lowest resolution case do we observe a plateau feature, which is due to the insufficient resolution to solve for the VSI. The VSI seems to operate in the full vertical extent. We expect a physical boundary for the VSI to be the high-temperature region caused by the FUV radiation. We also expect this position to be where the X-ray–FUV heated boundary layer is located at H_R=6.2 (see Fig.2.9 and Fig.2.10). Figure 2.10 shows that the time averaged vertical velocity increases above 60% of the sound speed at the expected wind base at H_R around 6.2. In the midplane layers the time averaged vertical motions remain small, at a level of around 1%.

Figure 2.11 shows the time-evolution of the local kinetic energy at the midplane at R_0. The local kinetic energy at the midplane replicates the same two growth regimes as the averaged global kinetic energy seen in Fig.2.4. The fast growth from the finger modes can even be seen at the vertical velocity at the midplane, and the slow growth of the body modes.

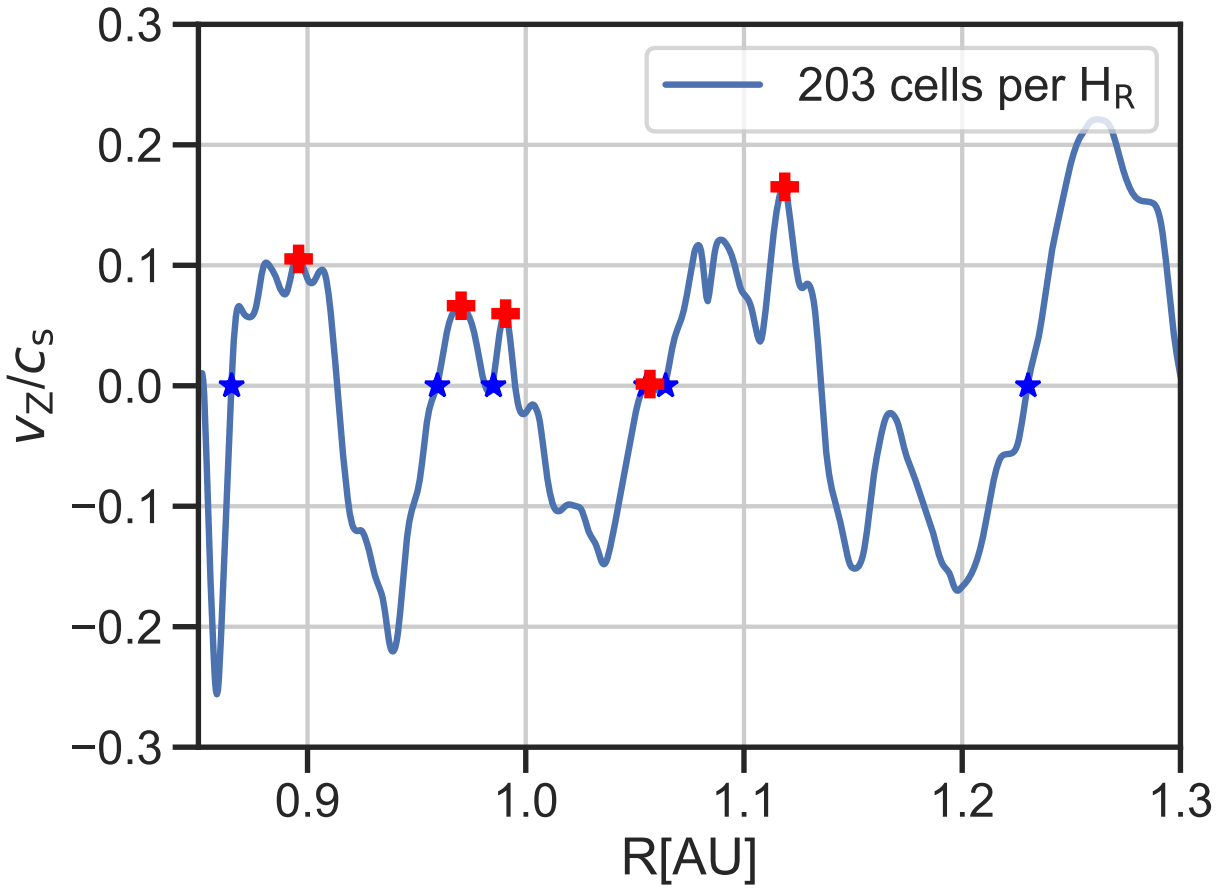

Figure 2.6: Same as Fig. 2.5 but for the 203 cells per scale height resolution case.

During the growth phase of the generation of the body modes, the local kinetic energy in the midplane in all three resolutions follow a linear growth rate of ∼0.13 orbits. This growth phase persists within the first ∼70 orbits; it corresponds to the slow growth rate of the body modes until reaching a saturation level of $\sim 10^{-4}$ and it is 2 times slower compared to the general growth rate found by Nelson, R. P. and Gressel, O. and Umurhan, O. M. (2013). The 203 and 101 cells per scale height generate the body modes faster than the 50 cells per scale height, which is the same tendency as found in Fig.2.8. We conclude that we need more than 50 cells per scale height to solve the VSI in accretion disks.

2.4.3 Small scale vortices

Fig. 2.12 and Fig. 2.13 show the result of the line integral convolution (LIC) method (e.g., Cabral & Leedom (1993)) to visualize the velocity magnitude vector field associated with velocity perturbations from the VSI, for the lowest and highest resolutions. The velocity magnitude includes the velocity field in every component and follows the ordinary prescription of $v_{\rm mag} = \sqrt{v_{\rm Z}^2 + v_{\rm R}^2}$, where $v_{\rm R}$=$v_r$sin(θ) + $v_\theta$cos(θ). From the LIC method, we find small-scale vortices in both resolution cases; however, these small-scale vortices are not featured in the lowest resolution case.

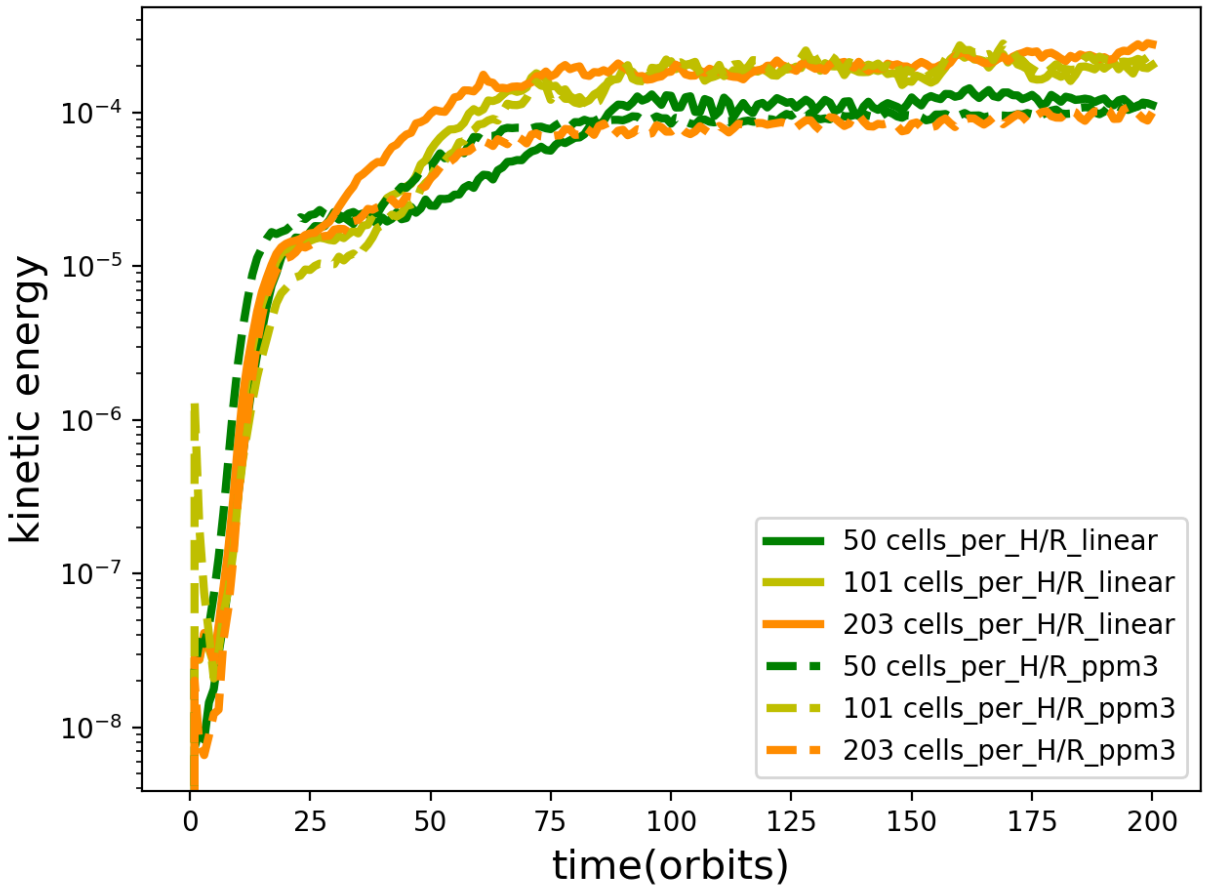

Figure 2.7: Same as in Figure 2.4 but with the PPM3 reconstruction method. Time evolution of the kinetic energy for different resolutions and space averaged at $R_0 = 1$ AU. The kinetic energy is normalized with the kinetic energy from pure Keplerian velocity. The different resolutions are color-coded (see inset).

The possibility of the presence of vortices formed by VSI was first found by Richard, Samuel and Nelson Richard P., and Umurhan Orkan M. (2016) in the $r - \phi$ plane. These vortices can be long-lived locally around 500 orbits (Manger & Klahr, 2018) with an $H_{\mathrm{R}} = 0.1$ and with an azimuthal and radial extension of about 40 and 4 au (Flock et al., 2020), respectively. In our case the vortices appear in the $r - Z$ plane, mostly inside the region between two large-scale upward and downward motions. They might be related to Kelvin-Helmholtz instabilities appearing between these large-scale motions as was described by Latter & Papaloizou (2018). Moreover, these small-scale vortices happen in an $H_{\mathrm{R}} < 5$, and are therefore more important for dust evolution.

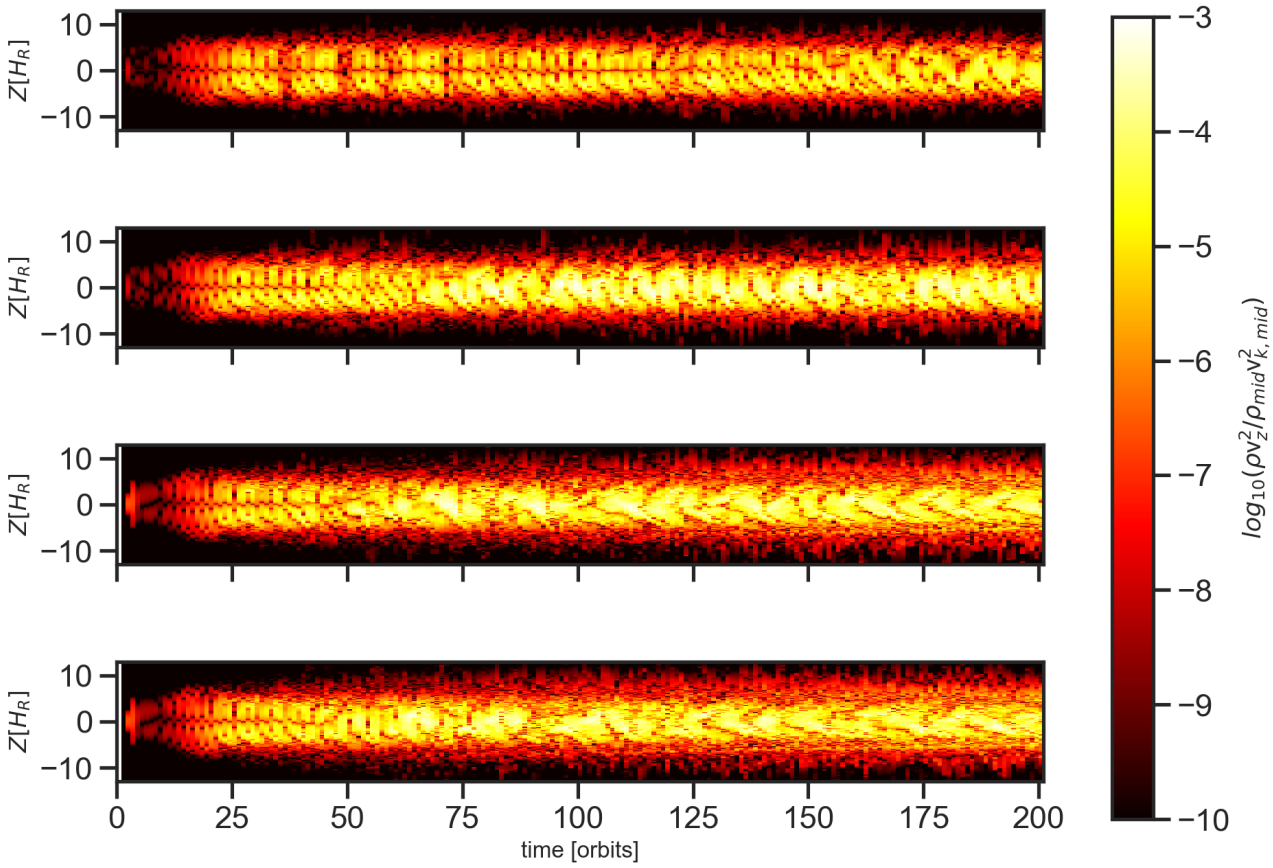

Figure 2.8: Time-evolution of the local kinetic energy at $R_0 = 1$ over height for different resolutions (from top to bottom: 25, 50, 101, 203 cells per scale height). The local kinetic energy is normalized to the global kinetic energy (see eq.2.8).

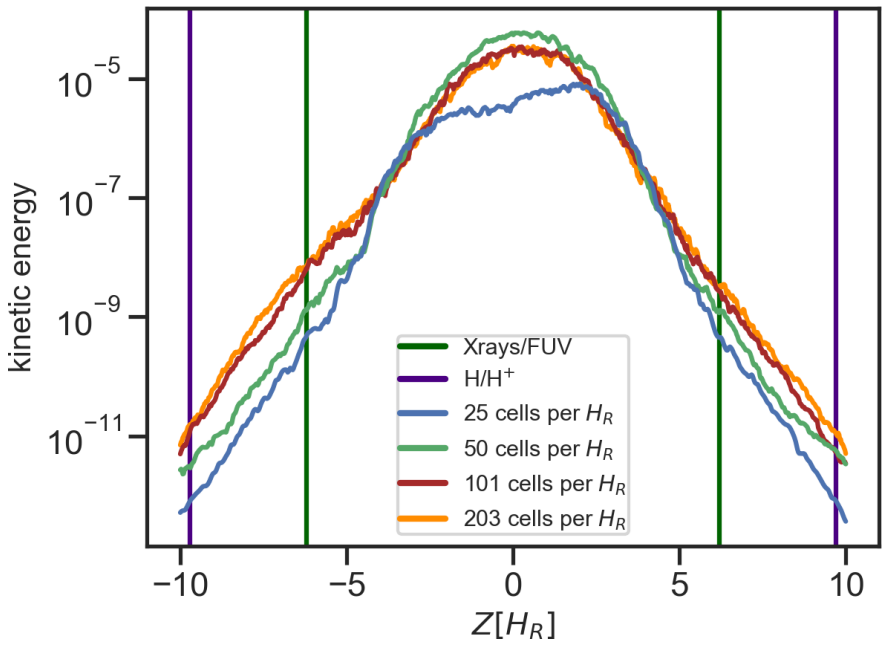

Figure 2.9: Averaged profile of the local kinetic energy normalized with respect to the kinetic energy in the midplane for the 25, 50, 101, and 203 cells per $H_{\rm R}$ at $R_0 = 1$ AU. The vertical colored lines represent $H_{\rm R} = 6.2$, where the X-ray–FUV heated boundary layer is (in dark green), and the $H_{\rm R} = 9.7$, where the EUV heated region is located (in purple) (same as in Fig. 2.3). The models for 101 and 203 cells per $H_{\rm R}$ are in good agreement. The density floor is located $H_{\rm R}$=13, and therefore does not influence our result.

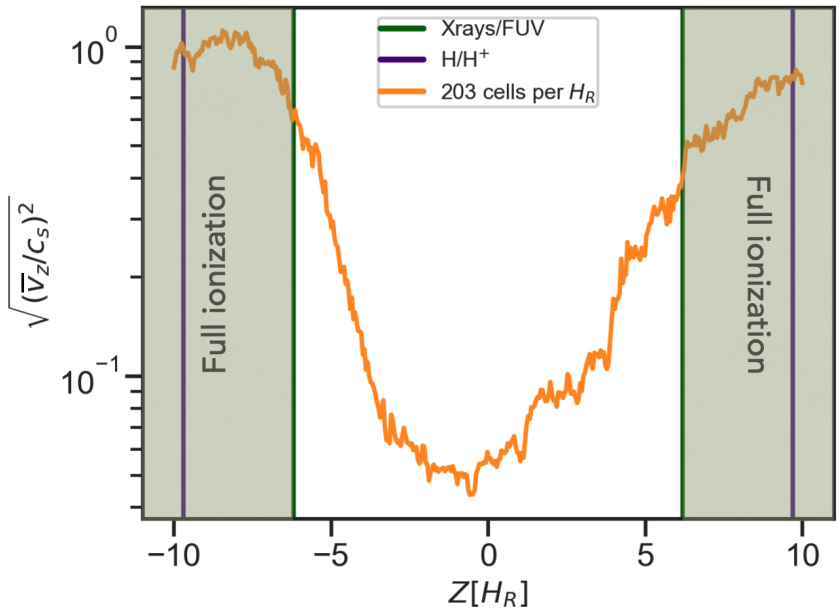

Figure 2.10: Averaged profile of the vertical component of the velocity normalized with respect to the sound speed for the 203 cells per $H_{\rm R}$. The vertical colored lines are the same as in Fig.2.9. At $H_{\rm R}$ =6.2 the vertical velocity reaches $0.3c_{\rm s}$. The hot ionized region is expected to start beyond $H_{\rm R} > 6.2$.

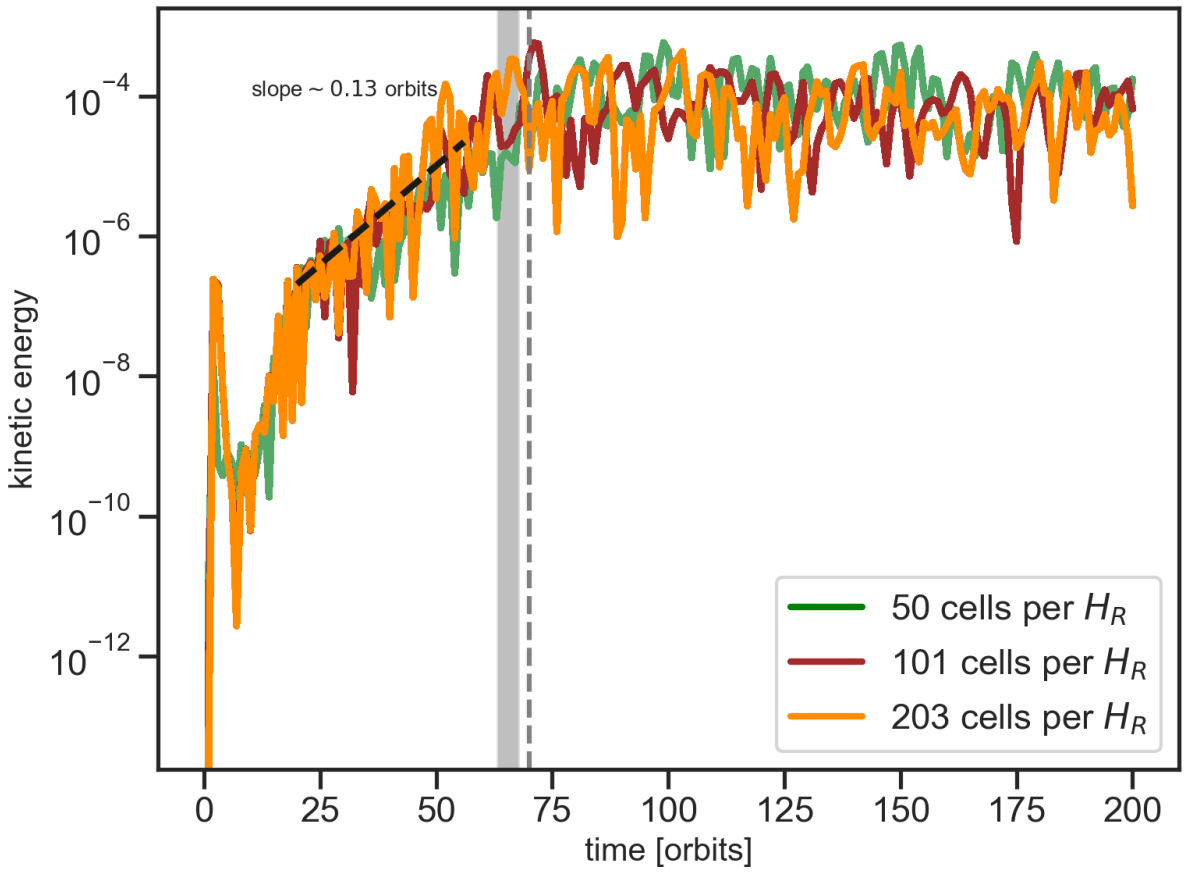

Figure 2.11: Averaged profile of the vertical component of the velocity normalized with respect to the sound speed for the 203 cells per $H_{\rm R}$. The vertical colored lines are the same as in Fig.2.9. At $H_{\rm R}$ =6.2 the vertical velocity reaches $0.3c_{\rm s}$. The hot ionized region is expected to start beyond $H_{\rm R} > 6.2$.

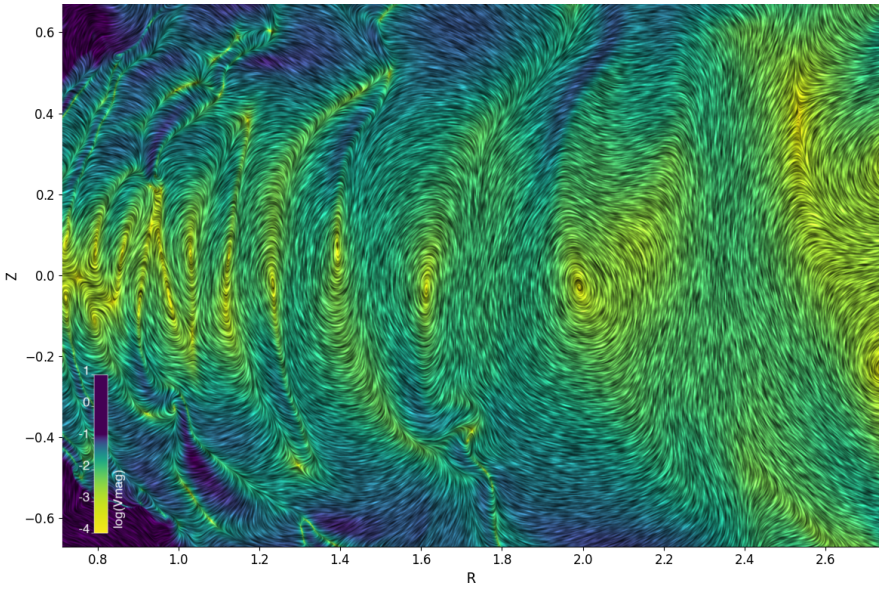

Figure 2.12: Snapshot of v_{mag} for the 25 cells per scale height at 200 orbits. The colored contour plot shows v_{mag} and the streamlines show the velocity flow pattern when applying the LIC method. The v_{mag} range (from 0 to 0.2 in code units) is narrowed down to highlight the low-velocity perturbations close to the midplane associated with the VSI. Visualization rendering credit: Andre Muller (HdA).

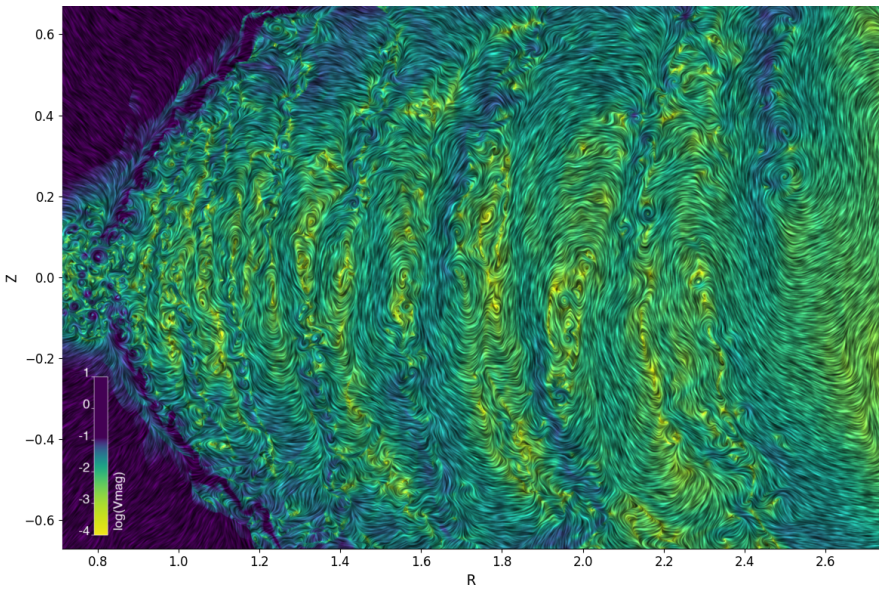

Figure 2.13: Same as Fig. 2.12 but a snapshot of v_{mag} for the 203 cells per scale height to be compared to the lowest resolution of 25 cells per scale height at 200 orbits. Visualization rendering credit: Andre Muller (HdA).

2.5 Implications of planet formation and the launch of winds in disks

The VSI is a large-scale global instability that potentially plays an important role in the evolution and dynamics of protoplanetary disks. In the midplane the dust settling overcomes the VSI, and as the dust concentrates and grows to millimeter size and greater, these particles settle against VSI and eventually undergo SI to favor planet formation (Lin, 2019). However, the VSI in combination with the SI leads to radial dust concentration in long-lived accumulations which are significantly denser areas than those formed by the SI alone (Schäfer et al., 2020a).

We observe symmetric features, which have not been observed before, after 100 orbits in the time evolution of the kinetic energy (Fig. 2.8). Furthermore, we refer to the LIC plots (Fig. 2.13) that show the presence of small vortices along the midplane, where grains can be concentrated. We encourage further analysis of this manner and its effect on planet formation in the future.

2.5.1 Frequency-integrated cross-section

The VSI can maintain small particles (< 100 μm) floating (Lin, 2019) until they eventually become ionized by FUV photons at the disk surface and contribute to heating in the atmosphere. Both the photoionization effects and the high temperature in this region make the surface of the disk and atmosphere an optimal scenario for photoevaporation processes, resulting in the launch of winds. In the disk atmosphere the MHD winds are likely favorable (Cui & Bai, 2020) at less than 5 AU. Cui & Bai (2020) showed that VSI and MHD winds can coexist, while magnetized winds being the dominant process to transport angular momentum. However, this would depend on 1) the so-called wind base, which depends mainly on the position of the EUV and FUV layers, and 2) a realistic thermal profile. By considering the initial flux and the extinction along the radial line of sight we can determine the location and extension of the wind in the future work. The detailed role of the VSI in the mechanism of wind launching has to be investigated, especially because the magnetic coupling to the gas remains low in the FUV shielded region ($H_{\mathrm{R}} < 6.2$). Recent improvements by Wang et al. (2019) and Gressel et al. (2020), aimed at including more realistic scenarios, have included thermochemistry and irradiation in their global magnetohydrodynamical simulations.

2.5.2 Electron density

The temperature and electron number density can be inferred from thermally excited forbidden lines (e.g., [OI] 5577/6300 line ratio) in regions where high temperatures (> 5000 K) lead to collisional excitations of electrons (Simon et al., 2016). Including or not the effects of X-rays, the electron relative abundance between the EUV heated layer and the X-ray–FUV heated layer is still $\sim 10^{-4}$, which comes from atomic carbon ionization by FUV. The electron density in this region can be as high as $\sim 10^4$-10^5 cm^{-3} at $\sim$1 AU (Nakatani et al., 2018a,b). We expect that at < 1 AU, the X-ray, EUV, and FUV fluxes are higher; therefore, photons penetrate deeper in the disk and the electron density can be higher. On the

other hand, farther from the star the electron abundance decreases, and as does the electron density.

2.6 Conclusions

We performed 2.5D (axisymmetric) hydrodynamical simulations for an isothermal accretion disk with different resolutions, up to 203 cells per scale height to fully resolve for the VSI. Resolution study for the VSI is important to assess its effect in different regions of the disk. We determine that the standard resolution of 50 cells per scale height is the lower limit to resolve the VSI. This determination is based on the total kinetic energy saturation level. Our key points can be summarized as follows:

1. We found the VSI to operate throughout the entire disk until reaching our density floor 0.003 cm^{-3} at around $H_\mathrm{R} = 13$ at R_0=1 for resolutions ≥ 50 cells per scale height. We expect turbulent scenarios where the X-ray–FUV heated boundary layer at $H_\mathrm{R} = 6.2$ is located, whereas the EUV heated region reaches $H_\mathrm{R} = 9.7$. Nevertheless, we encourage the use of high resolution (≥ 50 cells per scale height) to properly conduct the analysis of VSI.

2. We found at a resolution of 25 cells per H_R the appearance of a plateau around the midplane when looking at the local kinetic energy over height. This could serve as a diagnostic to check whether or not the VSI is fully resolved.

3. We observe a clear dependence on the growth rate of the body modes with resolution. For the highest resolution the growth of the body modes saturates after 70 orbits.

4. We diagnose the presence of small-scale vortices between the large-scale motion of the VSI when performing the LIC method. These small-scale vortices reach $H_\mathrm{R} < 5.0$; therefore they are more important for dust evolution. The vertical kinetic energy shows a more symmetric oscillation for the upper and lower hemisphere for the highest resolution. In the future we will fully investigate the dynamical influence of the heated layers on the VSI and the disk evolution. A resolution of 50 cells per scale H_R seems to capture the main characteristics of the VSI, and so is suitable for future studies.

3 Forbidden Emission Lines in Protostellar Outflows and Jets with MUSE

"Qunatum physics tells us that no matter how thorough our observation of the present, the (unobserved) past, like the future, is indefinite and exists only as a spectrum of possibilities"

by Stephen Hawking

3.1 Context

The detection of forbidden emission lines in different samples of T Tauri stars has provided access to different physical conditions depending on their line-of-sight (LOS) velocity information. Performing a line decomposition has led to the classification of different velocity components that originate from different physical mechanisms (Hamann, 1994; Hartigan et al., 1995; Ercolano & Pascucci, 2017; Fang et al., 2018; Banzatti et al., 2019; Pascucci et al., 2020). All these different physical mechanisms, that may include jets, accretion shock heating by magnetospheric accretion, and/or thermal photoevaporative winds, play an important role on the angular momentum transport and extraction of the material from the protoplanetary disk (i.e., Blandford & Payne (1982); Casse & Ferreira (2000); Casse & Keppens (2002); Sheikhnezami et al. (2012); Stepanovs & Fendt (2016); Mattia & Fendt (2020); Rodenkirch et al. (2020)). It was thought that turbulence due to magneto-rotational instability (MRI; Balbus & Hawley (1991)) is the main mechanism that drives the angular momentum transport within the first 1-5 au but, it is almost completely suppressed by non-ideal MHD effects (Bai & Stone, 2013) because of the low coupling between the gas and the magnetic field in weakly ionized gas, resulting in a magnetically driven wind. Disk winds are presumably generated in the surface of the disk where surrounding gas must be highly ionized, enough for electrons to be thermally excited; temperatures can be greater than 5,000 K with densities between 10^5-10^6 cm^{-3} (Simon et al., 2016). Therefore, the study of forbidden emission lines can provide clues about what main processes are taking place in the inner disk.

Although T Tauri sources show complex line profiles, velocity components mostly trace photoevaporative or magnetohydrodynamic winds by the narrow and broad low-velocity component (LVC). A small percentage (∼30%; Nisini et al. (2018)) show a high-velocity

component (HVC) associated with jets. Though winds and outflows/jets are formed by different mechanisms, collimated disk winds could form the base to a outflow/jet-like structure. Many surveys (i.e., Hamann (1994); Hartigan et al. (1995); Hirth et al. (1997); Antoniucci et al. (2011); Rigliaco et al. (2013); Natta et al. (2014); Simon et al. (2016); Nisini et al. (2018); Fang et al. (2018); Banzatti et al. (2019)) have shown that the HVC of the [O I] λ6300 excitation line is common and likely probing outflows, jets, or MHD winds (Edwards et al., 1987; Hartigan et al., 1995; Bacciotti et al., 2000; Lavalley-Fouquet et al., 2000; Woitas et al., 2002). Moreover, the HVC in T Tauri disks has been spatially confirmed to be associated with jets. Their emission reach a greater extension from the star than those lines with the LVC (Dougados et al., 2000). Other lines such as [N II] λ6583 and [S II] λ6731 have also been reported to probe outflows/jets (Solf & Boehm, 1993; Dougados et al., 2000; Lavalley-Fouquet et al., 2000; Woitas et al., 2002; Natta et al., 2014; Nisini et al., 2018), in which the detailed kinematic structure has been determined from the analysis of such intrinsic line profiles. Another important line is Hα that also traces velocity fields of outflows/jets (Edwards et al., 1987; Bacciotti et al., 2000; Woitas et al., 2002), as well as accretion processes in the accretion flow onto a planet and in the circumplanetary disk (i.e., Haffert et al. (2019); Hashimoto et al. (2020); Marleau et al. (2021)).

Studying the connection between the inner disk and the outer disk has attracted a lot of attention lately. Despite the rings and gaps that are seen in protoplanetary disks, shadows could indicate some degree of misalignment between the inner disk and the outer disk (Marino et al., 2015; Stolker et al., 2016; Debes et al., 2017; Benisty et al., 2017; Casassus et al., 2018; Benisty et al., 2018; Pinilla et al., 2019; Muro-Arena et al., 2020). Resolving the inner parts of the disk is quite challenging. A recent study by Bohn et al. (2021) has combined near-infrared and submillimeter interferometric observations to assess the innermost disk and measure possible misalignment in a sample of T Tauri disks and Herbig Ae/Be disks. In their paper, they emphasize the great difficulty to measure a possible misalignment between inner and outer disks in T Tauri disks, particularly due to the limited angular resolution of VLT/GRAVITY and/or the specific geometry orientation of the disks.

3.2 MUSE/VLT observations and data reduction

The observations were carried out between November 2019 and January 2020 with VLT/-MUSE in the NFM under program-ID 0104.C-0919 (PI: A. Müller). MUSE is an optical integral field spectrograph covering the spectral range from 4650–9300 Å at a resolving power of ∼2000 at 4600 Å and ∼4000 at 9300 Å (Bacon et al., 2010) with a spectral sampling of 0.125 nm per pixel. The adaptive-optics assisted NFM has a field of view (FOV) of 7.4×7.4 arcsec^2 with a spatial scale of 0.025 arcsec per pixel, which is about 10 times smaller pixel scale than the wide field mode. With this spatial resolution we are able to recover the spatial extension, by means of x and y pixels, of the emission that is coming from the outflow/jet. The VLT adaptive optics system uses four laser guide stars whose wavelengths are ranging from 5781 Å to 6048 Å. This spectral range is removed from the MUSE spectra to avoid the presence of additional lines that comes when the laser interact with air molecules.

The MUSE-NFM observations were reduced with the standard ESO pipeline v2.8.1 (Weilbacher et al., 2012, 2014, 2016) which includes bias subtraction, spectral extraction, flat-

fielding, wavelength calibration, and flux calibration. Although the NFM includes an atmospheric dispersion corrector (ADC), the centroid variations can still be a few spatial pixel along the entire wavelength range. Therefore, we corrected the calibrated pixel tables for each exposure based on the centroid shifts with wavelength measured on intermediate cube reconstructions. The corrected pixel tables are then used to create the fully combined cube of all calibrated exposures.

The wavelength calibration is done by using a Helim-Argon ARC lamp from the day before each night of observations. Due to temperature variations, the wavelength solution for a given spectrum can be offset and an empirical wavelength correction using bright sky lines should be applied (Weilbacher et al., 2020). Sky lines are, however, faint in the NFM, so this wavelength correction is hard to apply. These offsets can vary from target to target and are of the order of fractions of a pixel, up to a pixel in extreme cases (5-50 km s^{-1}; see also Xie et al. (2020)). We report eight data cubes that were obtained over 0.5 h each.

3.2.1 Rotational offset analysis in MUSE

We carried a residual rotation analysis for the NFM data of globular clusters in order to get the accuracy of the MUSE field of view orientation (see Kamann et al. (2018)). This analysis is done with PampelMuse software (Kamann et al., 2013) which uses the centers of dense star clusters, which have been pre-imaged with Hubble Space Telescope (HST), and then the stars available are identified in the astrometric reference catalogues in the MUSE cubes. This is done using a coordinate transformation with six parameters that takes into account shifts along the x- and y-axes, while others parameters are measure of distortions and rotations. Figure 3.1, shows the residual rotation for all the wide field mode (WFM) observations (blue) taken until late 2021 and the NFM observations (red). From the first sight, there is no systematic difference between the results derived from WFM and NFM cubes, which is reassuring and the resulting uncertainty is less than 1 degree for both modes, less than 0.2 degrees for the NFM particularly. The same analysis is used by Emsellem et al. (2021) where the MUSE field of view orientation is of the order of a few 10th of a degree. Based on this residual analysis, we consider the rotational accuracy of MUSE NFM to be 0.2 degrees, which is a conservative selection. As expected this uncertainty value does not change the actual uncertainty estimates for our $PA_{outflow/jet}$ reported on Table 3.1.

3.2.2 MUSE and ALMA image registration

When comparing the MUSE images with ALMA data, we focus on the comparison between the geometry of the dusty disk plane, as measured with ALMA, and the position angle of the outflow/jet, as measured with MUSE. With the assumption that the disk is circular and the star is at its center, the ALMA observations can be used to recover the inclination and the position angle of the disk relative to the fitted disk center. In our sample, the systems have their disk geometry calculated through visibilities (Long et al., 2018) or through image fitting (Huang et al., 2018b). We adopt those values already recovered as the referenced inclination and position angle for the outer disk plane. As both of those works fitted the center of the disk under the previously mentioned assumptions, the PA_{dust} already includes the observational and instrumental uncertainties, which remains fixed in this work.

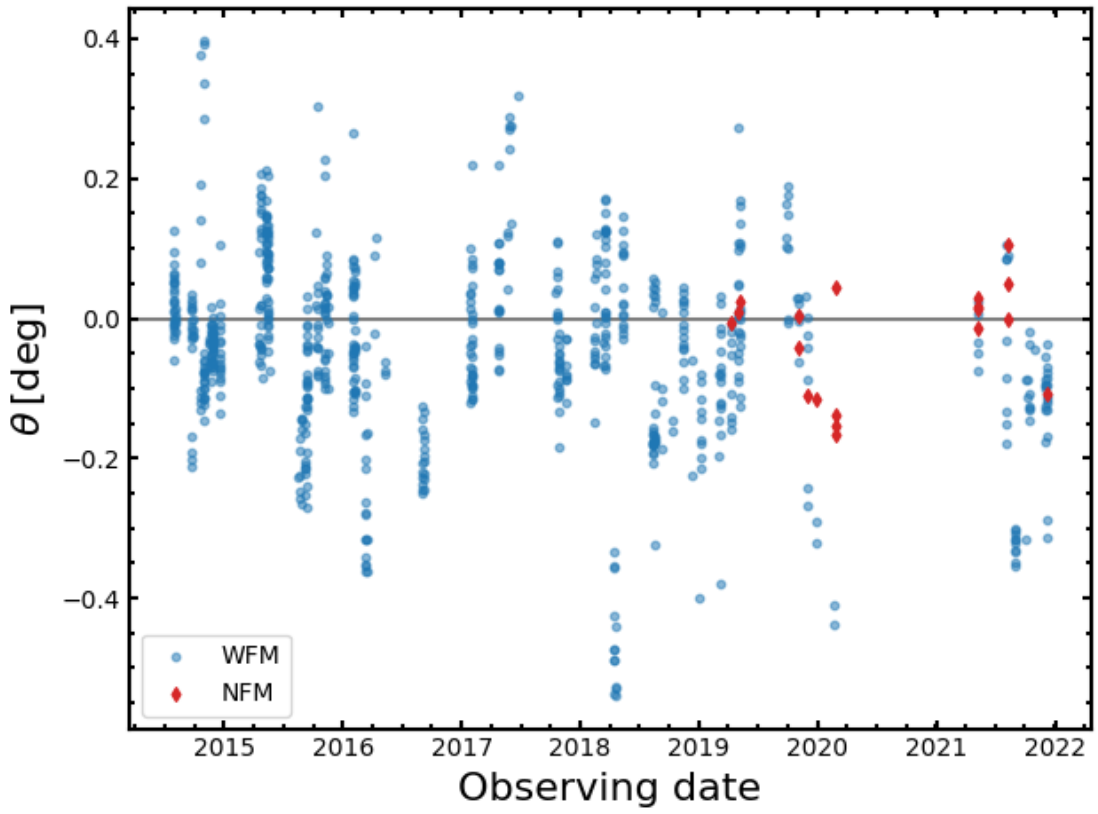

Figure 3.1: Residual rotation of the WFM observations (blue) taken until late 2021 and the NFM observations (red). Note the NFM residuals are less than 0.2 degrees.

With MUSE, our assumption to recover the $PA_{outflow/jet}$ is that the star is centered in the image frame. In order to confirm this, we fit a 2D circular Gaussian to the specific channels that we used to analyze the $PA_{outflow/jet}$. We do this to the reduced data cube without PSF subtraction under the assumption that the outflow/jet emission is negligible compared to the stellar emission. We found that for each channel the Gaussian centers are less than 1 pixel (or smaller than 25mas given that this value is the pixel scale of the MUSE image) from the center of the images for all sources. Therefore, we measured the $PA_{outflow/jet}$ relative to the center of the image where the star is. An additional assumption when comparing ALMA with MUSE is that the outer disk plane has not changed even if both images were taken at different epochs. The comparison of the geometry of the disk with different instruments is similar to the work done by Bohn et al. (2021) where they combined the K-band from GRAVITY/VLTI to constrain the geometry of the inner disk by finding the best parametric SED solution to the squared visibilities. They use ALMA ^{12}CO and ^{13}CO data to constrain the geometry of the outer disk. Their determination of potential misalignment between the inner and outer disk is narrowed down by comparing the inclinations and position angles defined by the planes of the inner and outer disks, respectively. For MUSE, we include the rotational accuracy to be 0.2° when propagating the error for each $PA_{outflow/jet}$ estimate (see Appendix **??**).

3.3 Dust continuum parameters

The disks presented here have been well studied and are well known to have dust substructures detected at millimeter wavelengths. We adopt some disk properties such as the inclination, and PA_{dust} from previous work that performed the disk model fitting, based on the dust morphology and the origin of the substructures. The distance of each source is obtained from the Gaia Collaboration et al. (2020).

The disk properties were obtained and analyzed from three different datasets. The disk properties from IM Lup and GW Lup were obtained from the Disk Substructres at High Angular resolution Project (DSHARP) at 1.25 mm continuum observations with a high spatial resolution of $0\farcs12$ (Andrews et al., 2018; Huang et al., 2018b). For the disks in the Taurus star-forming region, we considered the ALMA Cycle 4 observations (ID: 2016.1.01164.S; PI: Herczeg) that were observed at 1.33 mm and a resolution of $\sim0\farcs12$ (Long et al., 2018; Long et al., 2019).

3.3.1 Sample spectrum

We identified seven forbidden emission lines: [O I] $\lambda\lambda$6300, 6363, [N II] $\lambda\lambda$6548, 6583, Hα, [S II] $\lambda\lambda$6716, 6730, that are seen to be originating from the innermost part of the disk as outflow/jet-like structures (Fig.3.2, Fig.3.13, Figure 3.4, Figure 3.7, and Figure 3.9). Some of these lines have been reported in some of the sources we analyzed here (i.e., Simon et al. (2016); Fang et al. (2018); Banzatti et al. (2019)). We use Natta et al. (2014), Podio, L. et al. (2006), and the NIST atomic spectra database * for the line identification and line uncertainty. The $PA_{outflow/jet}$ is defined as the position angle of the outflow/jet measured in degrees, that lie approximately in direction perpendicular to the rotational axis of the disk. In the next section, we will cover in detail about how the geometrical derivation of the $PA_{outflow/jet}$ is conducted. It is very likely that we are not solely seeing jets, but also outflows and perhaps winds that are unrevealed due to the low spectral resolution of MUSE. Any description and/or analysis of winds is out of the scope of the present work, as it is necessary to asses the few km s^{-1} velocity components that characterize them. We perform a Gaussian fit to the emission lines to study their velocity components, and finally, we measure the length of the jet, to estimate the mass loss from the [O I] λ6300 line.

Figure 3.4, Figure 3.7, and Figure 3.9 show the spectrum by spatially summing the area enclosed to the jet over all channels, for all sources presented in this work. In the upper right we zoom into the wavelength range where the seven forbidden emission lines are identified and analyzed here. DL Tau shows the best signal-to-noise emission in all of the seven lines analyzed here. The DL Tau spectrum shows the presence of just a couple of more emission lines in the blue regime such as Hβ λ4861 and a weak one at $\sim$5156 Å (see Fig. **??**). We also found very faint emission of Hβ in DS Tau and CI Tau. We report emission lines in the red optical regime as well at around [Ca II] λ7288, [O II] $\lambda\lambda$7320,7329, 7373, and [Fe II] $\lambda\lambda$ 8619, 8892 for DL Tau and CI Tau, that host strong outflows/jets. We encourage further analysis of these other lines that lie out of the scope of this paper. The strong outflow/jet is seen very clear and collimated in all seven emission lines in DL Tau, reaching close to 200 au in

*https://physics.nist.gov/PhysRefData/ASD/lines_form.html

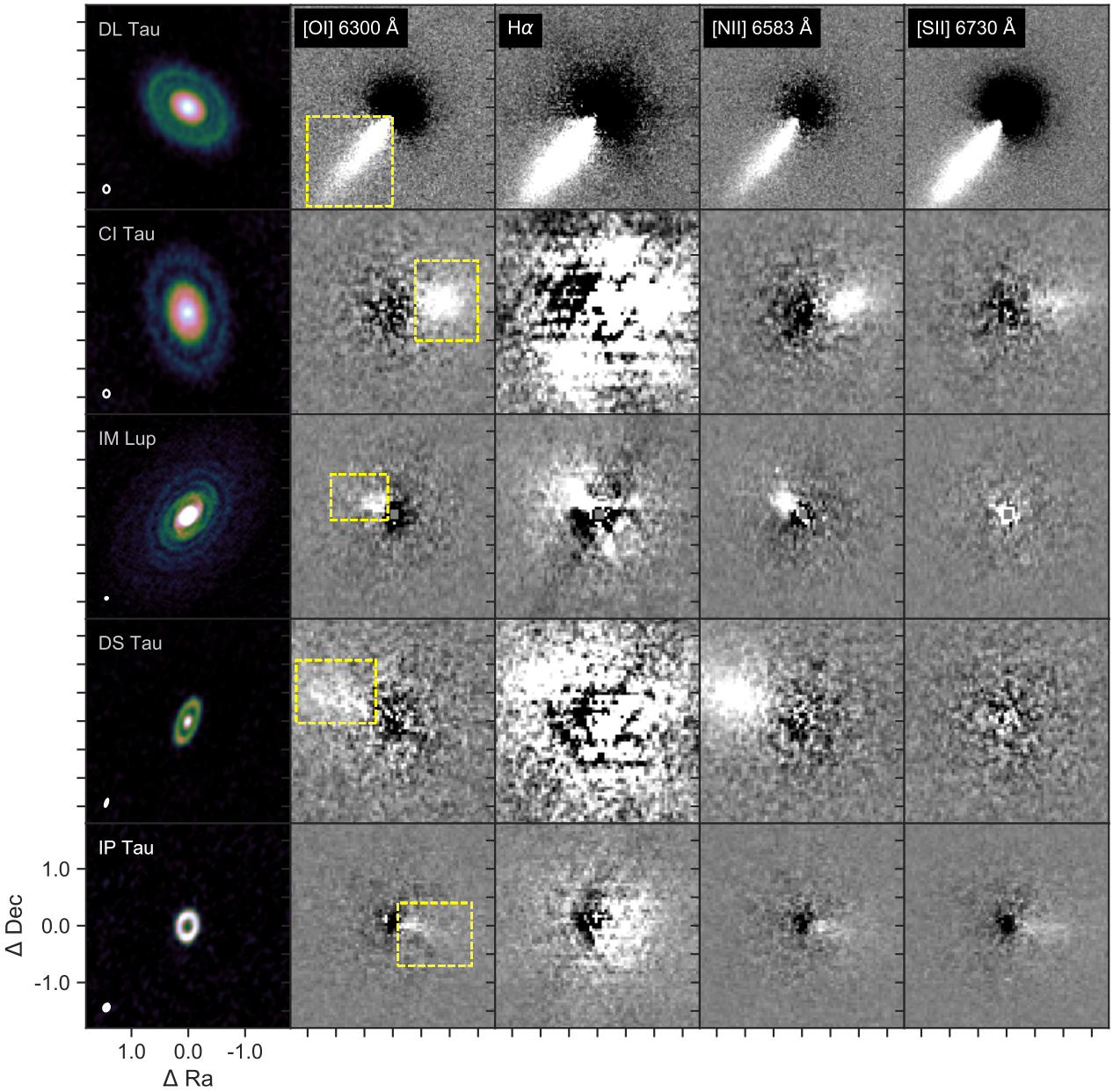

Figure 3.2: Composite image of different protoplanetary disks at four different forbidden emission lines. The first column shows the dust continuum emission at 1.3 mm from ALMA cycle 4 (Long et al., 2018; Long et al., 2019). The other columns show the different forbidden emission lines from MUSE as labeled in the top left, in the first row. The dashed yellow rectangles mark the area from where we gather the spectrum of the jet; by summing over the spatial axes within the dashed yellow frame in the image.

extension. As a comparison, the extension of the outflow/jet in CI Tau only reach around 60 au.

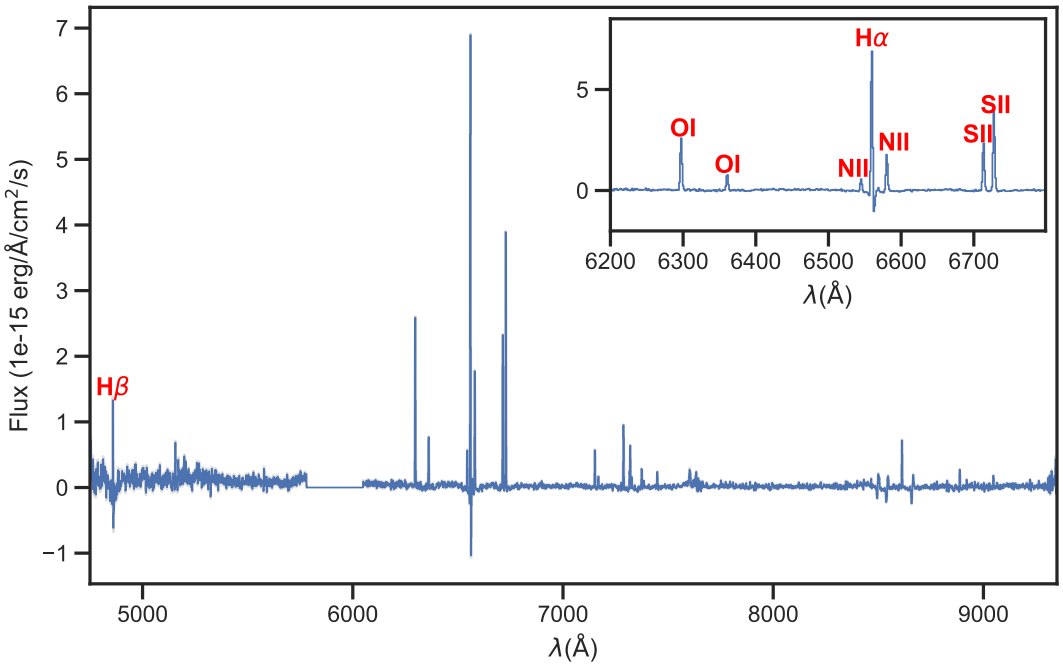

Figure 3.3: Spectrum in the area enclosed to the jets of DL Tau.

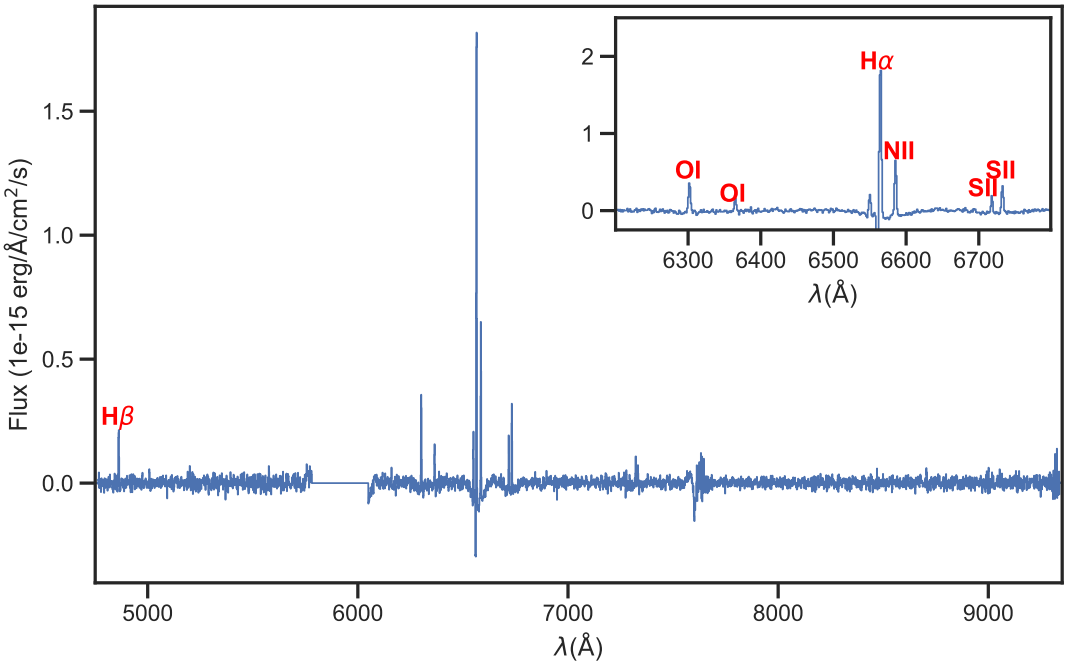

Figure 3.4: Spectrum in the area enclosed to the jets of DS Tau.

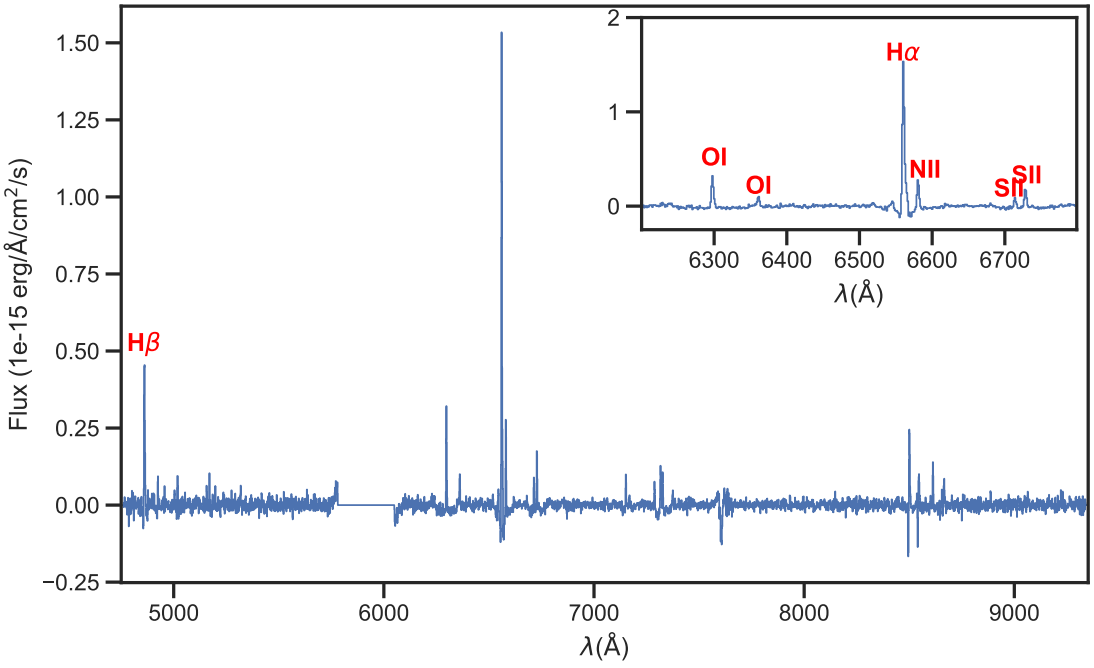

Figure 3.5: Spectrum in the area enclosed to the jets of CI Tau.

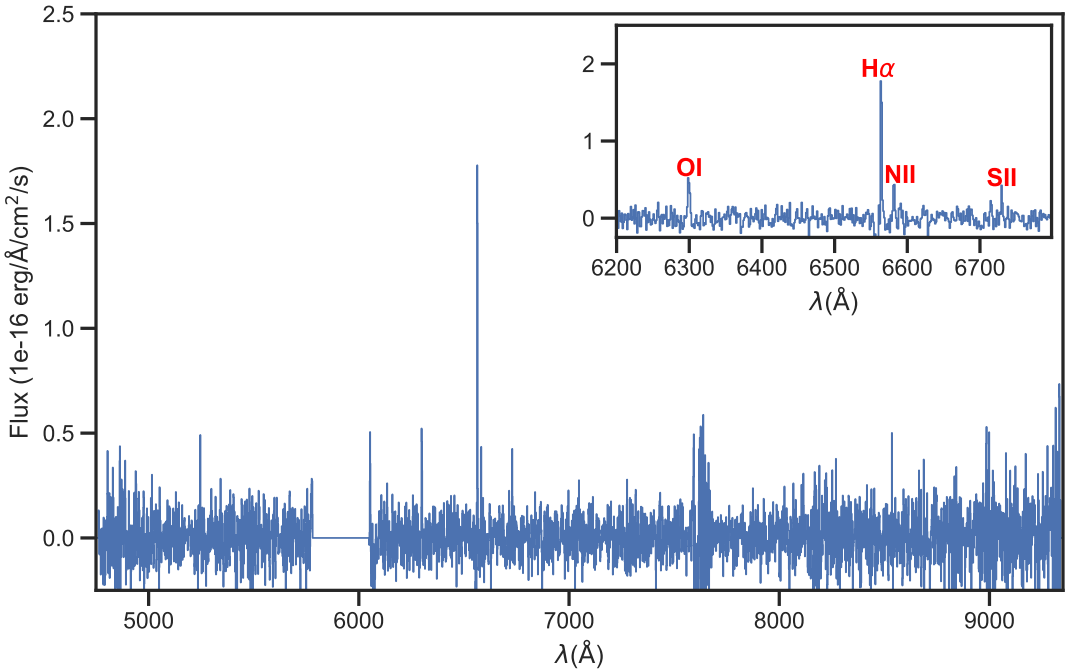

Figure 3.6: IP Tau

Figure 3.7: Spectrum in the area enclosed to the jets of IP Tau.

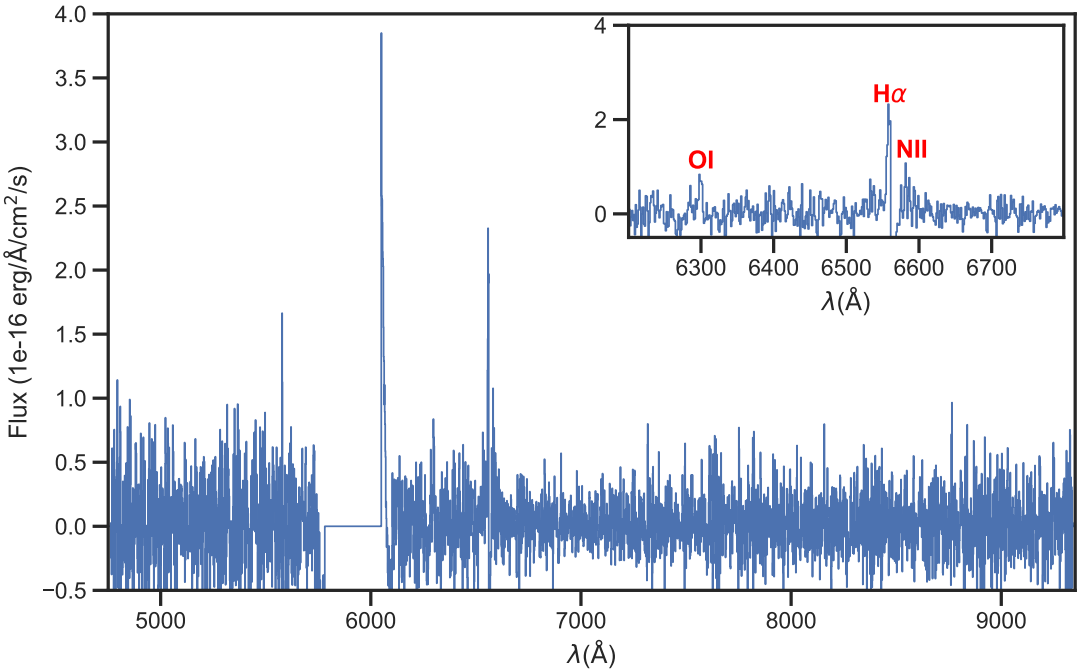

Figure 3.8: IM Lup

Figure 3.9: Spectrum in the area enclosed to the jet of IM Lup.

3.4 Geometrical fitting of the outflows/jets

In order to derive the $PA_{outflow/jet}$ for each spectral line in all disks, we fit the jet intensity peaks with a linear function. We read the maximum value across the outflow/jet for the forbidden emission lines detected on each source, and store the x and y positions that correspond to the jet emission into a new array. These are then converted into polar coordinates where $r = \sqrt{x^2 + y^2}$ and $\theta = \arctan(y/x)$. Jet intensity peaks are only considered if they are above 5σ of the background. For other imaging parameters and wavelengths see Table 3.3. The retrieved positions contain the angular information to be used to calculate the $PA_{outflow/jet}$. In order to fit a line along these retrieved positions of the jet, we employ a fitting method or routine called the orthogonal distance regression (ODR; Brown et al. (1990)) that gathers the retrieved data and the linear model function all together in order to produce the best linear parameters for the jet. The linear model function follows the simple ordinary prescription of a line, $f(x_i; \vec{\beta}) = \beta_1 x + \beta_0$, where, x_i is the position in pixels, and β_0 and β_1 are the unknown parameters to be found by the ODR routine. We assign an initial standard deviation for each jet peak position to be 1 pixel. Choosing a 1 pixel is a conservative selection for the initial standard error as we found that when estimating the $PA_{outflow/jet}$, the corresponding error of the Gaussian center is smaller than 1 pixel. As the function we used for the fit, $f(x_i; \vec{\beta})$, is said to be linear in variables, x_i, and linear in parameters, $\vec{\beta}$, the total error is estimated by applying the linear least squares method. That is, by finding the set of parameters for which the sum of the squares of the n orthogonal distances from the $f(x_i; \vec{\beta})$ curve to the n data points is minimized. This error associated at the end of the fit follows: min $\sum_{i=1}^{n} [y_i - f(x_i + \delta_i; \vec{\beta})]^2 + \delta_i^2$, where δ_i is the error associated to each n data point.

Table 3.1: Disk properties (geometric parameters).

Name	α(J2000)	δ(J2000)	d_{pc} (pc)	incl (°)	PA_{dust} (°)	$\overline{PA}_{outflow/jet}$ (°)	difference (°)	ref.
DL Tau	04 33 39.07	+25 20 38.09	159.9	-45.0±0.2	52.1±0.4	143.00±0.31	0.9±0.5	[a]
CIDA 9	05 05 22.86	+25 31 31.23	165.6	45.6±0.5	102.7±0.7	not clear	–	[a]
CI Tau	04 33 52.01	+22 50 30.09	160.3	50.0±0.3	11.2±0.13	79.04±0.68	0.2±0.7	[a]
DS Tau	04 47 48.59	+29 25 11.18	158.4	-65.2±0.3	159.6±0.4	70.25±0.44	0.7±0.6	[a]
GO Tau	04 43 03.07	+25 20 18.70	142.4	53.9±0.5	110.9±0.24	not clear	–	[a]
IP Tau	04 24 57.08	+27 11 56.54	129.4	$-45.2^{+0.9}_{-0.8}$	173.0±1.1	83.28±1.55	0.3±1.9	[a]
IM Lup	15 56 09.17	-34 30 35.67	155.8	-47.5±0.5	143.9±0.6	56.89±0.56	2.9±0.8	[b]
GW Lup	14 46 44.72	-34 30 35.67	155.2	38.7±0.3	127.6±0.5	not clear	–	[b]

Notes. The inclination, and PA_{dust} are obtained from [a]Long et al. (2019), and [b]Huang et al. (2018b)

The distances, d_{pc}, are from the third release of the Gaia Collaboration et al. (2020)

The $\overline{PA}_{outflow/jet}$ represents the average among the lines we measure a $PA_{outflow/jet}$ in Table 3.2

Symbol '–' means no detection

For the iterative routine to estimate the $PA_{outflow/jet}$ for each emission line, we use as initial estimate the $PA_{outflow/jet}$ from the locations of the jet intensity peaks from the first part. Then, we use this first value for the $PA_{outflow/jet}$ as a seed for a second iteration, where we fit Gaussians to profiles that are orthogonal to the axis defined by the first $PA_{outflow/jet}$. A comparison between the peak intensity locations and the Gausssian centers are shown for

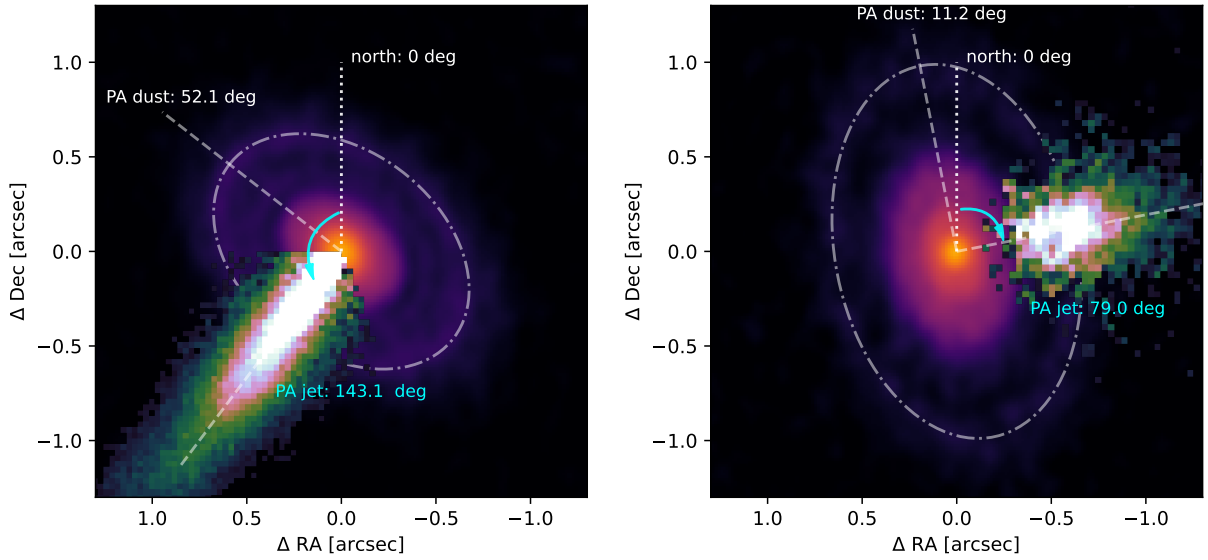

Figure 3.10: Example of the estimated $PA_{outflow/jet}$ of DL Tau (*left panel*) and CI Tau (*right panel*) outflow/jet. Both MUSE outflow/jet images are averaged from the different emission lines used to estimate the $\overline{PA}_{outflow/jet}$. We adopt the geometrical configuration visually demonstrated in Figure 3 from Piétu et al. (2007) for the disks that have positive and negative inclination. For DL Tau, the disk inclination is negative, and the $PA_{outflow/jet}$ is measured from north going counterclockwise. Unlike CI Tau, the disk inclination is positive and the $PA_{outflow/jet}$ is measured going clockwise.

DL Tau in Fig. 3.12 as an example. Those Gaussian centers are then used to calculate the final $PA_{outflow/jet}$ for each emission line. The final $PA_{outflow/jet}$ for the disks that we detect bright emission lines are shown in Table 3.2. Then, we take the average, $\overline{PA}_{outflow/jet}$, from the $PA_{outflow/jet}$ estimates of different emission lines in Table 3.2 and we add the corresponding errors in quadrature including the rotational accuracy of MUSE, that is 0.2°, to obtain a robust $\overline{PA}_{outflow/jet}$ value for each source. This $\overline{PA}_{outflow/jet}$ value for each source is then used to compared with the PA_{dust} (see Table 3.1). Note that CIDA9, GO Tau, and GW Lup jets were too compact at the center, making it difficult to estimate any $PA_{outflow/jet}$ properly. Before doing the comparison between the $\overline{PA}_{outflow/jet}$ and the PA_{dust}, it is important to understand the side of the disk plane to which the emission line is coming from. We use the same geometrical convention as in Figure 3 from Piétu et al. (2007) to indicate the real disk plane configuration through the inclination for each disk system.

In Fig. 3.10, we portray this convention by superimposing the outflows/jets to the mm dust continuum of the protoplanetary disk. It shows a better visualization of the measured $\overline{PA}_{outflow/jet}$, in comparison with the PA_{dust}, for DL Tau (*left panel*) for the negative inclination case, and CI Tau (*right panel*) for the positive inclination case. The PA_{dust} follows the usual standard definition of the position angle of the major axis counted in degrees, from 0° to 180°, from north to east. Since DL Tau has a negative inclination, the $PA_{outflow/jet}$ values are measured counterclockwise from north, and it is similar to say that the disk is flipped. On the other hand, CI Tau have a positive inclination then the $PA_{outflow/jet}$ values are measured clockwise from north. Having identified the inclination of the disks, we were able to determine

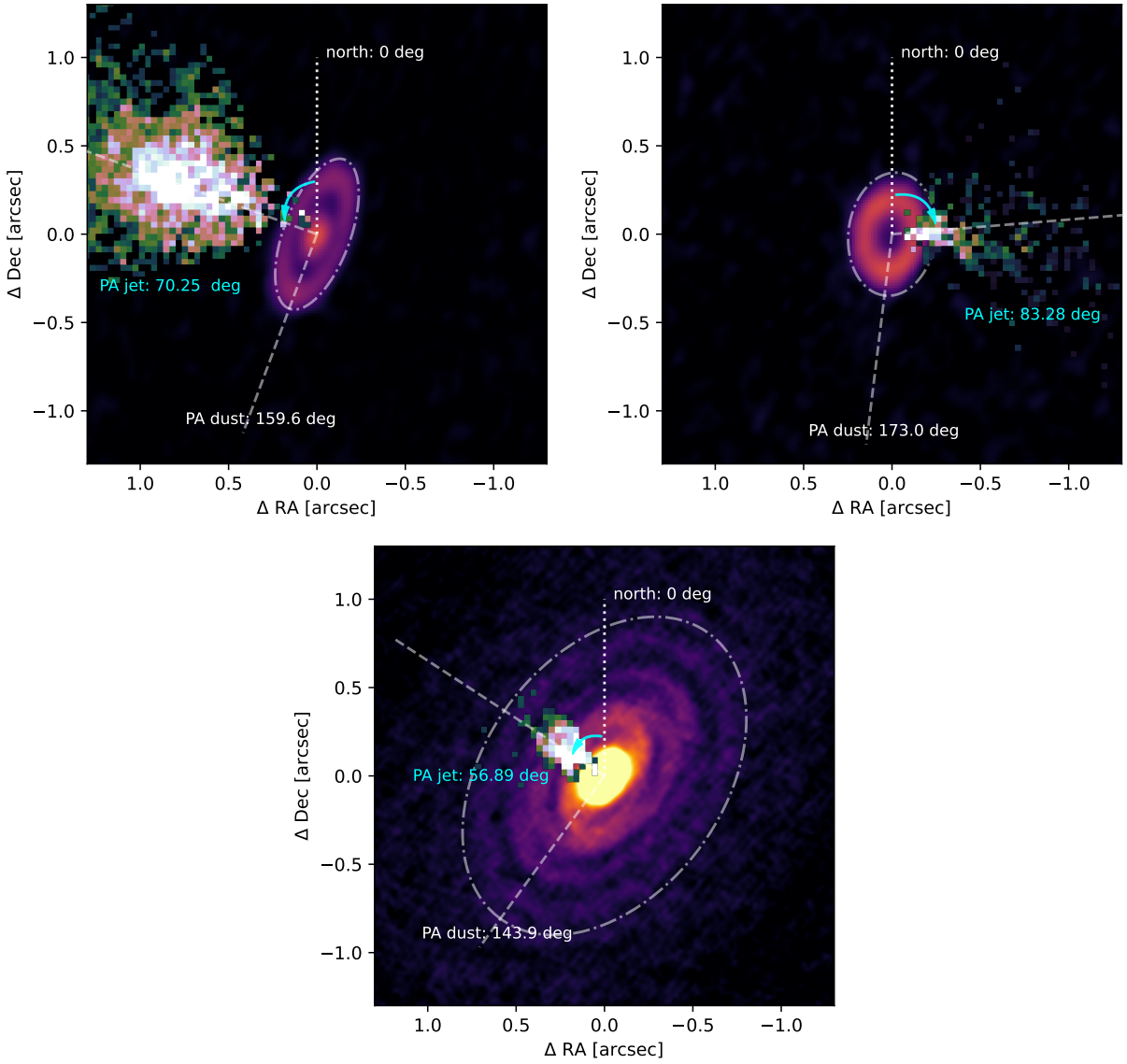

Figure 3.11: Same as Figure 3.10 but for DS Tau, IP Tau, and IM Lup.

the rotation of protoplanetary disk-outflow/jet system (see Fig. 3.13). We recognize that DL Tau, IM Lup, DS Tau, and IP Tau have the disk inclination negative, and CI Tau has the disk inclination positive (see also Fig. 3.11. Once having identified the disk plane through the inclinations, we take into account the difference between the $\overline{\mathrm{PA}}_{\mathrm{outflow/jet}}$, that is related to the PA of the innermost disk, and the $\mathrm{PA}_{\mathrm{dust}}$. For this, we follow

$$\text{difference} = \begin{cases} ||\mathrm{PA}_{\mathrm{jet}} - \mathrm{PA}_{\mathrm{dust}}| - 90°|, & \text{if incl.}<0 \\ ||\mathrm{PA}_{\mathrm{jet}} + \mathrm{PA}_{\mathrm{dust}}| - 90°|, & \text{if incl.}>0 \end{cases} \tag{3.1}$$

We found that the difference between the $\mathrm{PA}_{\mathrm{outflow/jet}}$ and the $\mathrm{PA}_{\mathrm{dust}}$ to be small in general (see Table 3.1). For the sources analyzed here, the estimation of the $\mathrm{PA}_{\mathrm{outflow/jet}}$ and their associated errors lie within the estimation of the $\mathrm{PA}_{\mathrm{dust}}$ and its associated error range. The spread of values between different emission lines for the each source in Table 3.2 comes from the Gaussian fits and they do not reflect the uncertainty in the difference of the possible misalignment. It is the case that the estimation of the $\mathrm{PA}_{\mathrm{outflow/jet}}$ for IM Lup was more difficult because of the low signal-to-noise level. The intensity variations in the outflow/jet are very close to noise variation level resulting in a $\mathrm{PA}_{\mathrm{outflow/jet}}$ difference of 7.7° between the [O I] λ6300.30 and [N II] λ6583.45 lines. By calculating the difference between $\mathrm{PA}_{\mathrm{outflow/jet}}$ and $\mathrm{PA}_{\mathrm{dust}}$ we get $6.82° \pm 0.78°$ and $0.87° \pm 0.68°$ for [O I] λ6300.30 and [N II] λ6583.45 line, respectively. It is the source in our sample that shows a higher difference of 2.9° between the $\overline{\mathrm{PA}}_{\mathrm{outflow/jet}}$ and $\mathrm{PA}_{\mathrm{dust}}$. Since 2.9° lies within the range of 0.87° and 6.82° we measure for IM Lup, we consider no misalignment. We understand that the Gaussian fit is underestimating the real $\mathrm{PA}_{\mathrm{outflow/jet}}$ and this result could be even better improved by increasing the signal-to-noise.

We clearly detect two essential geometrical features. One is a broadening of the respective intensity distribution with distance, indicating that the jet width increases with distance from the star. The other feature is the variation of the location of the intensity maximum, indicating a wiggling of the jet axis. A periodic pattern in these changes may hint a precession or orbiting jet (Fendt & Zinnecker, 1998). In Fig. 3.26, the wiggle patterns are marked by the Gaussian centers as navy color dots. We further investigate how these Gaussian centers vary in position with respect to their distance from the jet axis (see Fig. 3.12). In order to check whether or not these successive Gaussian centers have periodicity, we calculate the deviation of them from the jet axis. Applying a simple sinusoidal function in a periodogram does not provide significance, even if essentially by eye there seems to be some type of quasi-periodic behavior in the Gaussian centers. In §3.9, we further discuss how the patterns of the Gaussian centers could possibly hint a sign of jet precession.

3.4.1 The linear model function

Figure 3.12 shows an example of the linear function model for [O I] λ6300 in DL Tau to estimate the $\mathrm{PA}_{\mathrm{outflow/jet}}$. As mentioned in Sect. 3.4 we perform a Gaussian fit to maximum jet intensity peaks locations in each row in order to avoid any bias by noise in the data. These Gaussian centers are orthogonal with respect to the line model function in light blue. We carried the same methodology for the other sources in our sample.

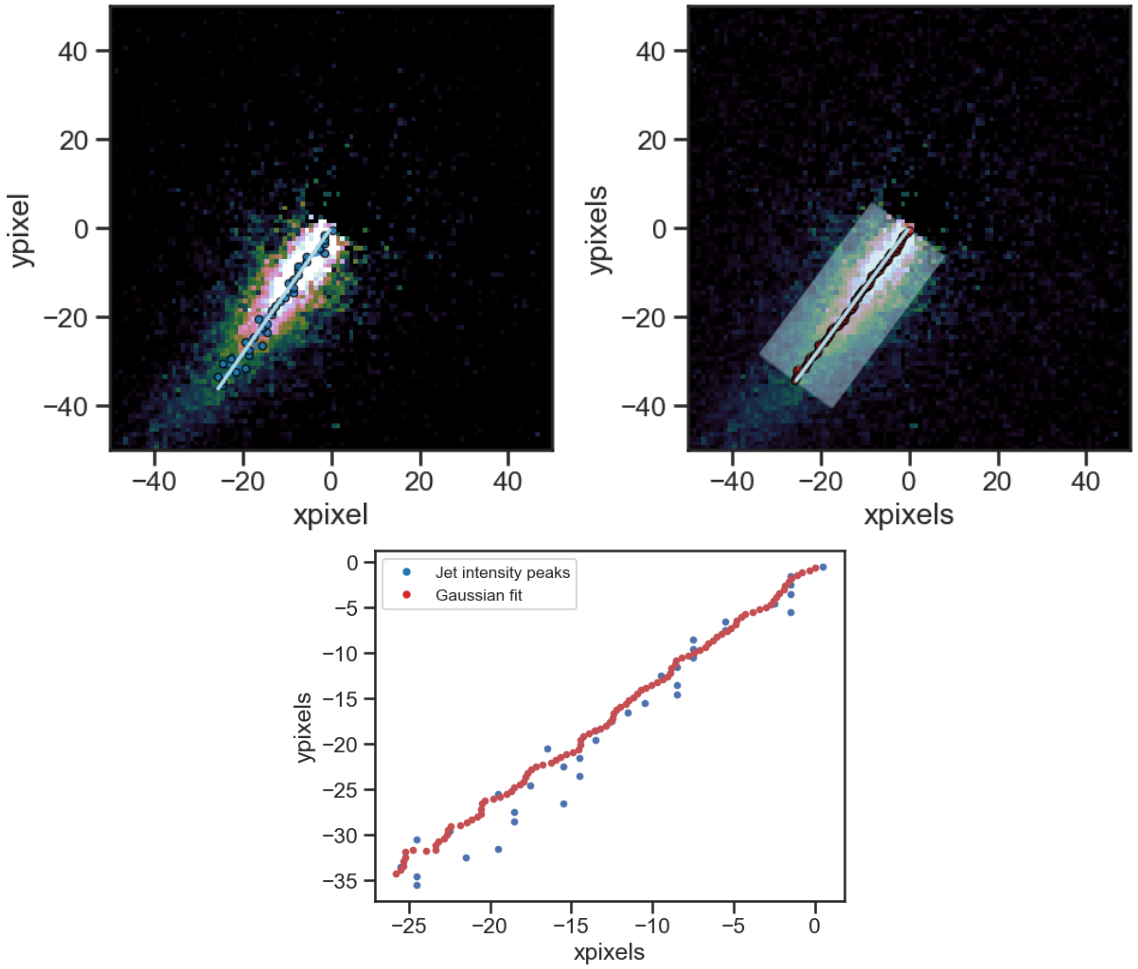

Figure 3.12: (*Top left*) DL Tau [O I] λ6300 jet as an example of the linear model function (light blue) based on the Gaussian centers (grey dots). (*Top right*) We fit 100 crossing lines in order to estimate the width across the outflow/jet. (*Bottom*) [O I] λ6300 successive outflow/jet intensity peaks across the jet axis in blue. Overplotted are the Gaussian centers from the fit in red, that is used to estimate the $PA_{outflow/jet}$. The deviations of the outflow/jet intensity peaks could be caused by noise in the data.

3.4.2 Disk inclination and rotation

In Figure 3.13 we have identified whether these disk-outflow/jet systems have positive or negative inclination to determine the direction to where the disk is rotating. We look at the rotation of the system based on the ^{12}CO channel maps. For IM Lup, we use Pinte et al. (2020). Also, the inclination of IM Lup was easily seen by looking at the bright side of the disk in near-infrared image from Avenhaus et al. (2018). For CI Tau, we use Rosotti et al. (2021). For IP Tau and DS Tau, we use Simon et al. (2017). For DL Tau, there is no evidence of the ^{12}CO channel maps in the literature nor any observations taken and posted in the ALMA archive. By looking at the blue-shifted outflow/jet in the MUSE image, it is intuitive that we are looking at the back side of the disk in DL Tau. For PDS 70 we use Keppler et al. (2019) and Isella et al. (2019).

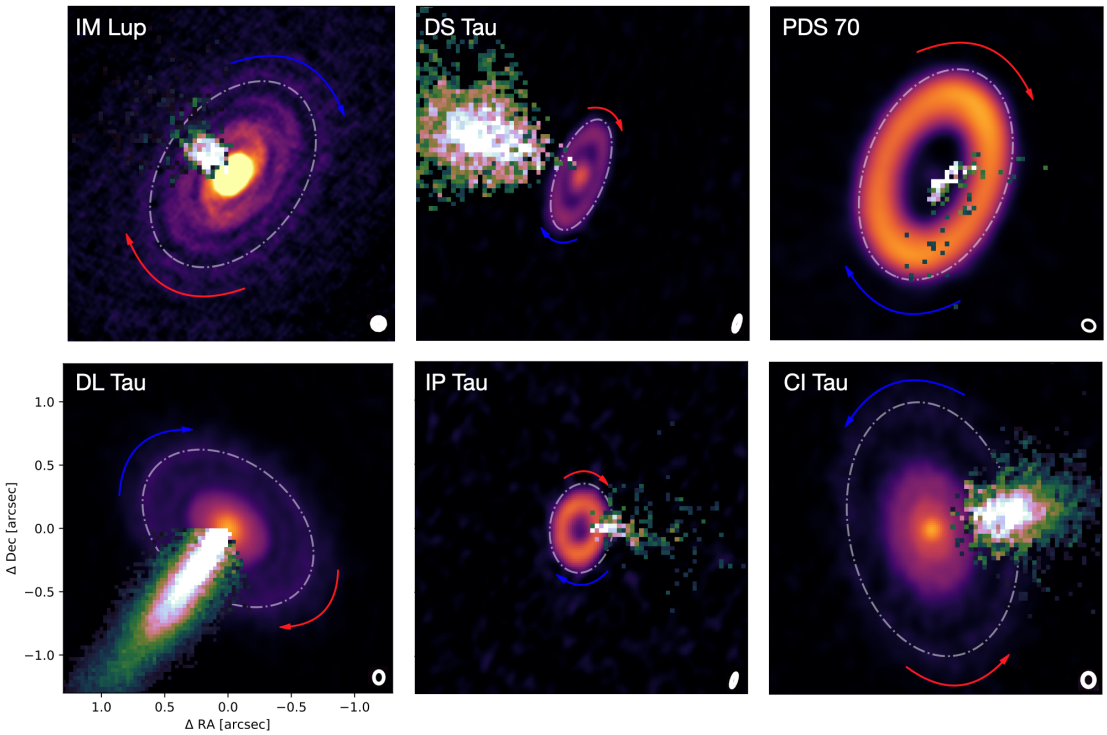

Figure 3.13: Composite images of disk-outflow/jet systems. The outflows/jets are superimposed to the dust continuum disk detected by ALMA Cycle 4 at 1.33 mm (Long et al., 2018). The arrows, representing the redshifted and blueshifted velocity components, shows the disk rotation. With this determination, IM Lup, DS Tau, PDS 70 (the top three panels) and, DL Tau and IP Tau have the disk inclination negative, whereas, CI Tau have its inclination positive. The outflow/jet in CI Tau, IP tau, and DL Tau are emission from [O I] λ6300. For IM Lup, and DS Tau are [N II] λ6583. Lastly, we decided to try out the data set of PDS 70 already published by Haffert et al. (2019) as there is some emission at the center seen in Hα. The disk inclination is -51.7±0.1 and the PA_{dust} is 156.7±0.1° as derived from ALMA Cycle 5 continuum observations at 0.855 mm by Keppler et al. (2019) (see also Isella et al., 2019). We estimated the $PA_{outflow/jet}$ for PDS 70 to be 154.82±5.92°.

3.5 Outflow/jet line profiles and velocity components

The emission of these forbidden optical emission lines have been established to trace outflows/jets and winds in T Tauri stars, and from their line velocity we can characterize whether it is a high velocity or a low velocity component (Edwards et al., 1987; Hartigan et al., 1995). For each spectral frame in the data cube, we sum pixel fluxes over the region defined by the dashed yellow rectangles in Fig.3.2 to obtain a spectrum of the emission. To measure the emission line centroids to sub-pixel precision, we take the line peak from a Gaussian fit to the data (see Fig.3.14, Fig. 3.15, Fig. 3.16, and Fig. 3.17). In Table 3.2, we report the de-projected outflow/jet velocities estimated from the Gaussian fits as follows: $v_{\rm outflow/jet} = c\left(\left(\lambda_{\rm gauss} - \lambda_{ref}\right)/\lambda_{ref}\right)/\cos(\textbf{incl})$ where c is the speed of light, incl is the inclination of the disk (Table 3.1), $\lambda_{\rm gauss}$ is the Gaussian fit centroid, λ_{ref} is the rest wavelength of each forbidden line in air. The errors on de-projected velocities, $v_{\rm outflow/jet}$, in Table 3.2 are propagated from the Gaussian fit and the disk inclination, but do not include the uncertainty in wavelength calibration that is likely between 5 km s^{-1} up to 50 km s^{-1} (see (Xie et al., 2020)). Most of the $v_{\rm outflow/jet}$ that we were able to estimate from the emission lines are blue-shifted and their values correspond mostly, but not limited to, high velocity components. We determine that for each source we only see one side of the outflow/jet, and the receding part of these outflow/jet velocities are obscured by the dust from their protoplanetary disk. Unlike the one-sided blue-shifted sources, we report red-shifted velocities for DS Tau.

The detection of Hα line seems to stand out in the spectra (Fig.3.4, Fig.3.7, and Fig.3.9). However, the Hα emission is seen spread in an area surrounding the line spread function, similar to a high noise intensity that Hα introduces from a high photon count level. This effect is not necessarily seen prominently in DL Tau (Fig. 3.14). This spread is caused by an instrumental artifact and the reason behind of this effect is unknown. Similar effects have been seen and analyzed by Xie et al. (2020), where the Hα line-to-continuum ratio varies across the field. These variations are so high that the residuals due to this instrument issue are stronger than those from photon noise. The noise reduction is taken into account when applying the principal component analysis (PCA; Soummer et al. (2012)) method but the error scale is so high that quantifying the real emission of Hα over the area is difficult.

Table 3.2: Outflow/Jet properties. The outflow/jet is obtained by de-projecting the line centroids from Gaussian fits as explained in Sect. 3.5; the errors reported in this table do not include the uncertainty in wavelength calibration. Symbol '–' means no detection.

Name	[O I] λ6300.30 ± 0.010 Å				[N II] λ6548.05 ± 0.10 Å			
	FWHM (km s^{-1})	$v_{\rm outflow/jet}$ (km s^{-1})	F_λ (erg s^{-1} cm^{-2} Å^{-1})	PA$_{\rm outflow/jet}$ (°)	FWHM (km s^{-1})	$v_{\rm outflow/jet}$ (km s^{-1})	F_λ (erg s^{-1} cm^{-2} Å^{-1})	PA$_{\rm outflow/jet}$ (°)
DL Tau	135.22	-217.8±2.0	7.96×10^{-15}	143.24±0.07	130.89	-216.3±2.0	1.93×10^{-15}	–
CIDA9	–	–	–	–	–	–	–	–
CI Tau	160.90	-209.7±1.3	1.18×10^{-15}	77.68±0.34	–	–	–	–
DS Tau	143.70	161.9±1.6	1.21×10^{-15}	69.01±0.33	–	–	–	–
GO Tau	–	–	–	–	–	–	–	–
IP Tau	204.58	-83.0±2.0	2.87×10^{-16}	83.28±1.54	–	–	–	–
IM Lup	262.19	-95.4±1.3	4.91×10^{-16}	60.72±0.46	–	–	–	–
GW Lup	–	–	–	–	–	–	–	–

The structured spectral line profiles reported here show the intrinsic outflow/jet velocity

Name	Hα λ6562.80 ± 10^{-5} Å				[S II] λ6716.44 ± 0.010 Å			
	FWHM (km s^{-1})	$v_{outflow/jet}$ (km s^{-1})	F_λ (erg s^{-1} cm^{-2} $Å^{-1}$)	$PA_{outflow/jet}$ (°)	FWHM (km s^{-1})	$v_{outflow/jet}$ (km s^{-1})	F_λ (erg s^{-1} cm^{-2} $Å^{-1}$)	$PA_{outflow/jet}$ (°)
DL Tau	121.73	-222.9±2.0	2.28×10^{-14}	142.67±0.08	124.87	-208.0±2.0	7.31×10^{-15}	143.16±0.08
CIDA9	–	–	–	–	–	–	–	–
CI Tau	154.65	-184.8±1.3	5.51×10^{-15}	–	150.17	-195.6±1.3	3.74×10^{-16}	–
DS Tau	–	–	–	–	115.56	151.2±1.6	6.48×10^{-16}	–
GO Tau	–	–	–	–	–	–	–	–
IP Tau	–	–	–	–	–	–	–	–
IM Lup	–	–	–	–	–	–	–	–
GW Lup	–	–	–	–	–	–	–	–

Name	[O I] λ6363.78 ± 0.010 Å				[N II] λ6583.45 ± 0.10 Å			
	FWHM (km s^{-1})	$v_{outflow/jet}$ (km s^{-1})	F_λ (erg s^{-1} cm^{-2} $Å^{-1}$)	$PA_{outflow/jet}$ (°)	FWHM (km s^{-1})	$v_{outflow/jet}$ (km s^{-1})	F_λ (erg s^{-1} cm^{-2} $Å^{-1}$)	$PA_{outflow/jet}$ (°)
DL Tau	135.67	-219.5±2.0	2.64×10^{-15}	143.64±0.15	116.65	-217.8±2.0	4.93×10^{-15}	143.48±0.1
CIDA9	–	–	–	–	–	–	–	–
CI Tau	–	–	–	–	158.72	-225.4±1.3	1.20×10^{-15}	79.52±0.33
DS Tau	–	–	–	–	129.32	194.8±1.6	2.18×10^{-15}	71.49±0.21
GO Tau	–	–	–	–	–	–	–	–
IP Tau	–	–	–	–	–	–	–	–
IM Lup	–	–	–	–	135.32	-124.1±1.3	3.77×10^{-16}	53.03±0.26
GW Lup	–	–	–	–	–	–	–	–

Name	[S II] λ6730.82 ± 0.010 Å			
	FWHM (km s^{-1})	$v_{outflow/jet}$ (km s^{-1})	F_λ (erg s^{-1} cm^{-2} $Å^{-1}$)	$PA_{outflow/jet}$ (°)
DL Tau	122.54	-236.6±2.0	1.16×10^{-14}	142.83±0.06
CIDA9	–	–	–	–
CI Tau	152.89	-189.7±1.3	7.35×10^{-16}	79.91±0.45
DS Tau	130.87	167.9±1.6	1.11×10^{-15}	–
GO Tau	–	–	–	–
IP Tau	–	–	–	–
IM Lup	–	–	–	–
GW Lup	–	–	–	–

peaks or the line-of-sight velocity for the lines that we were able to capture in the spectra (Fig. 3.14, Fig. 3.15, Fig. 3.16, and Fig. 3.17). The velocities values reported here are corrected with the stellar radial velocity that is reported in Table 3.1 from both, Banzatti et al. (2019) and Fang et al. (2018). The [O I]λ6300, Hα, [N II]λ6583, and [S II]λ6730 line profiles (Fig. 3.15, Fig. 3.16, and Fig. 3.17) for DL Tau and CI Tau are considerably blue-shifted with line center velocities much greater than 100 km s^{-1}. The deprojection velocities show that the velocity of the outflow/jet, $v_{outflow/jet}$, for DL Tau and CI Tau are greater or very close to 200 km s^{-1} tracing strong outflows/jets (see Table 3.2). In DL Tau, high-resolution spectra show both a high-velocity and a single low-velocity component (Banzatti et al., 2019), while the MUSE image is dominated by the strong high-velocity component. In addition, DL Tau hosts the most extended and collimated outflow/jet reaching approximately 180 AU. For CI Tau, a strong outflow/jet is reported for the first time; its morphology is different from the DL Tau one, as seen in Fig. 3.10 (*right panel*). By taking 200 km s^{-1} as an approximate velocity of the jets in DL Tau and CI Tau, and the distance of 159 pc and 160 pc, respectively, then, the proper motion of their extended outflow/jet is about 0.″26 per year.

The emission lines of DS Tau, IP Tau, and IM Lup have smaller line-of-sight velocity shifts of less than 100 km s^{-1} (except for DS Tau) and broader line widths considerably overlapping

0 km s^{-1}, which could hide some LVC emission. As mentioned before, DS Tau is the only source in this sample where the line emission appears red-shifted rather than blue-shifted; this is consistent with a high disk inclination (see Table 3.1) observed with ALMA, where the outflow appears only from the back side of the disk (see Fig.3.13). The IP Tau disk is a transition disk as seen in mm continuum emission (Long et al., 2018), and the MUSE data shows a blue-shifted component in the [O I] λ6300 line with properties in between the HVC and the LVC, which is in good agreement with what is observed in high-resolution spectral analysis (Banzatti et al., 2019). Interestingly, this line has been reported to vary over time (Simon et al., 2016). A recent work by Bohn et al. (2021) found no potential misalignment between the inner disk and outer disk in IP Tau when analyzing the VLT/GRAVITY and ALMA data. IM Lup is known to have a blue-shifted LVC- BC measured from the [O I] λ6300 line (Fang et al., 2018).

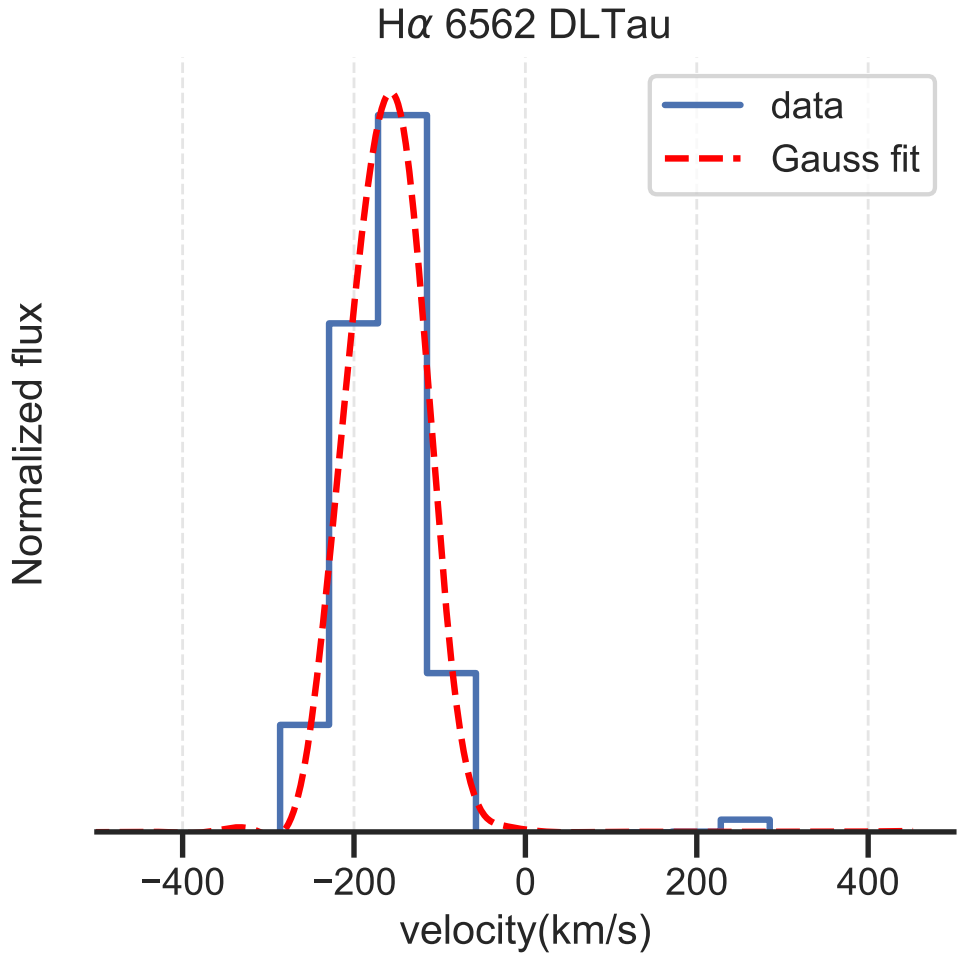

Figure 3.14: H_α line profile identified for DL Tau probing the high line-of-sight velocity component coming from the strong outflow/jet. The red dashed line represent the line-of-sight maximum velocity.

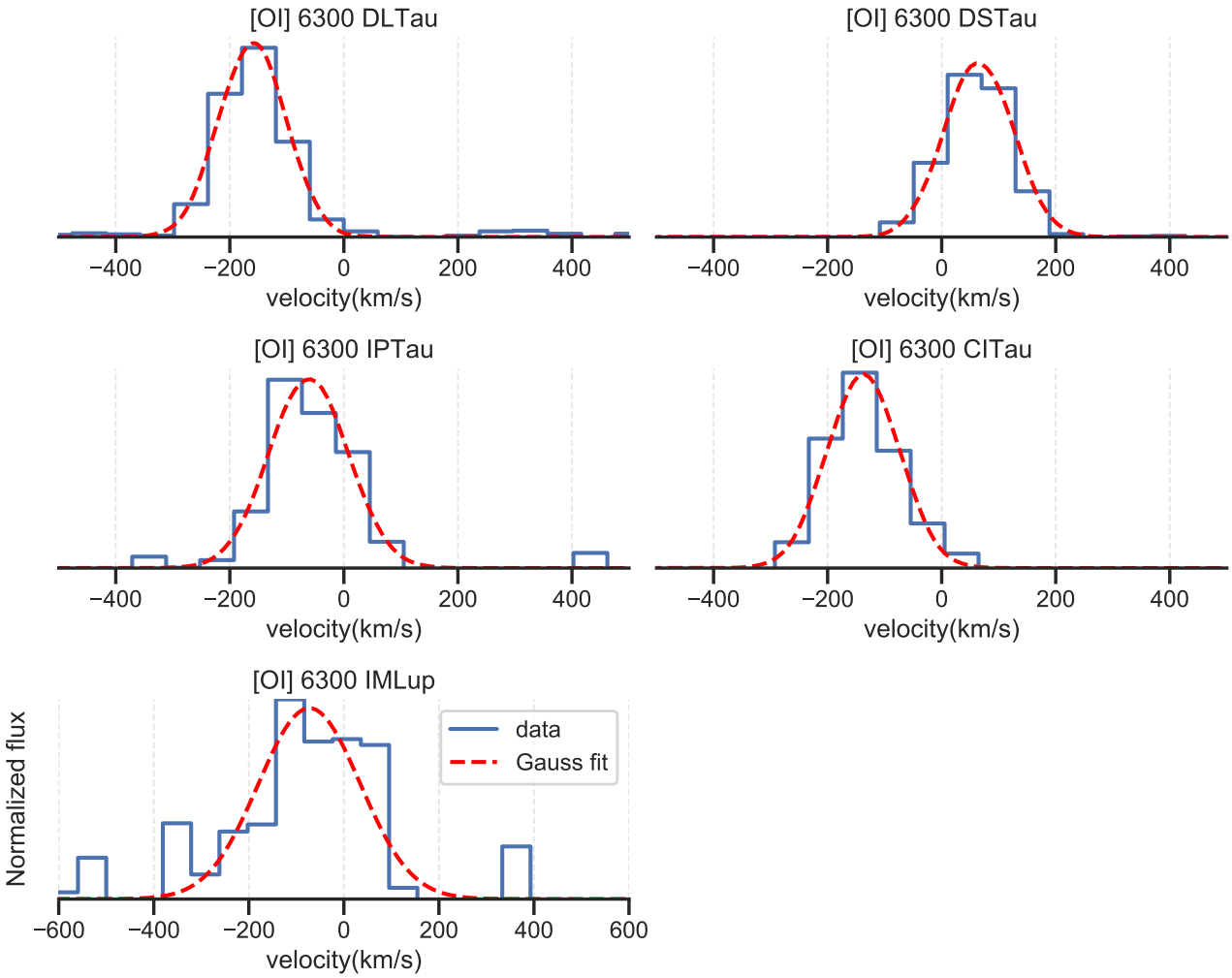

Figure 3.15: [O I]λ6300 line profiles identified in five sources from our sample. DL Tau and CI Tau have their line centered at velocities greater than 100 km s^{-1}, characteristic of jets. Unlike DL Tau and CI Tau, the disks of DS Tau, IP Tau, and IM Lup show smaller shifts of less than 100 km s^{-1} and broader line widths significantly overlapping with 0 km s^{-1}, therefore possibly including the LVC emission. DS Tau has the most centered line.

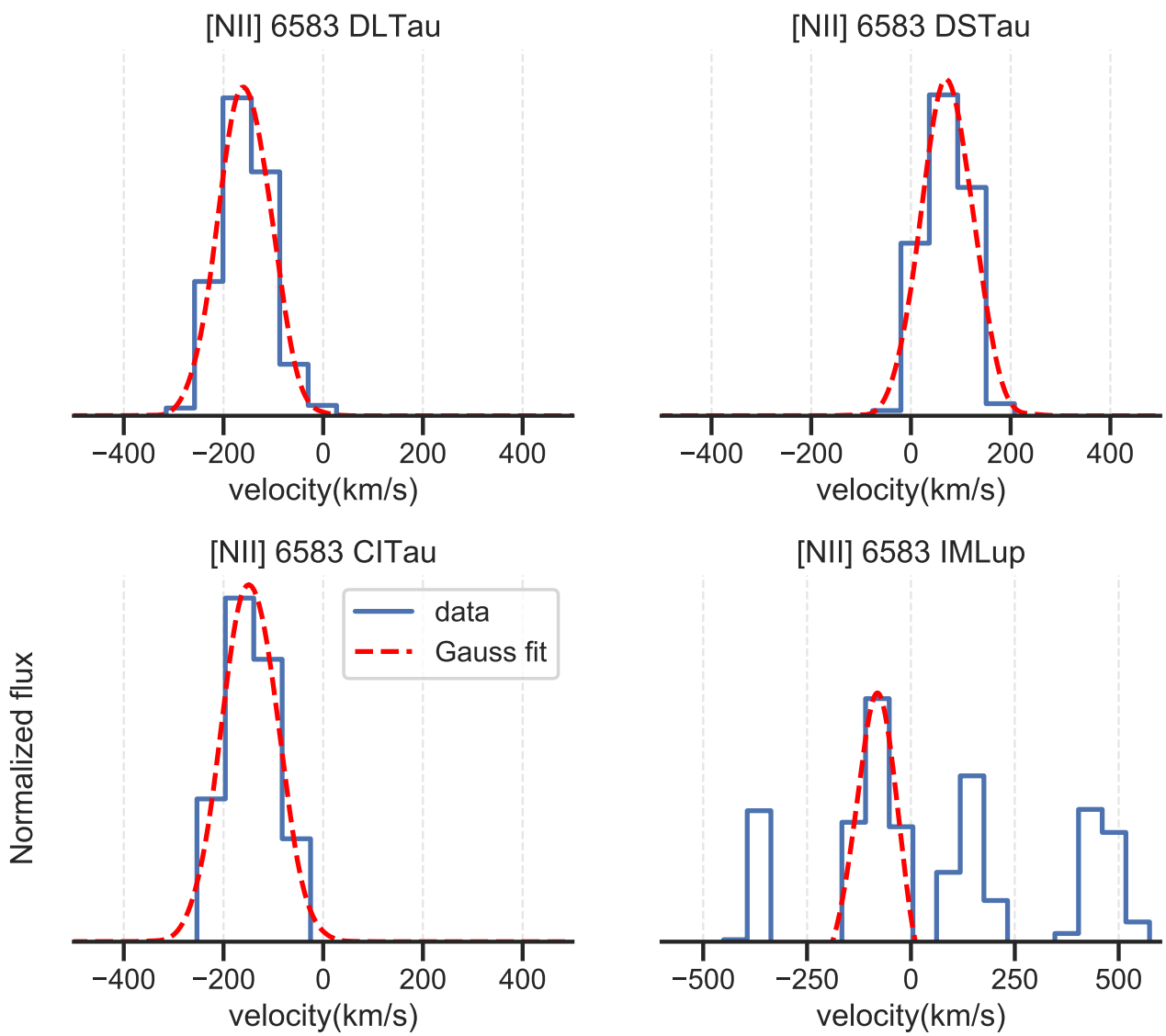

Figure 3.16: [NII]λ6583 line profiles identified in four sources from our sample. Same case as in Fig.3.15, DL Tau and CI Tau probe high velocity components while DS Tau and IM Lup are more centered to zero.

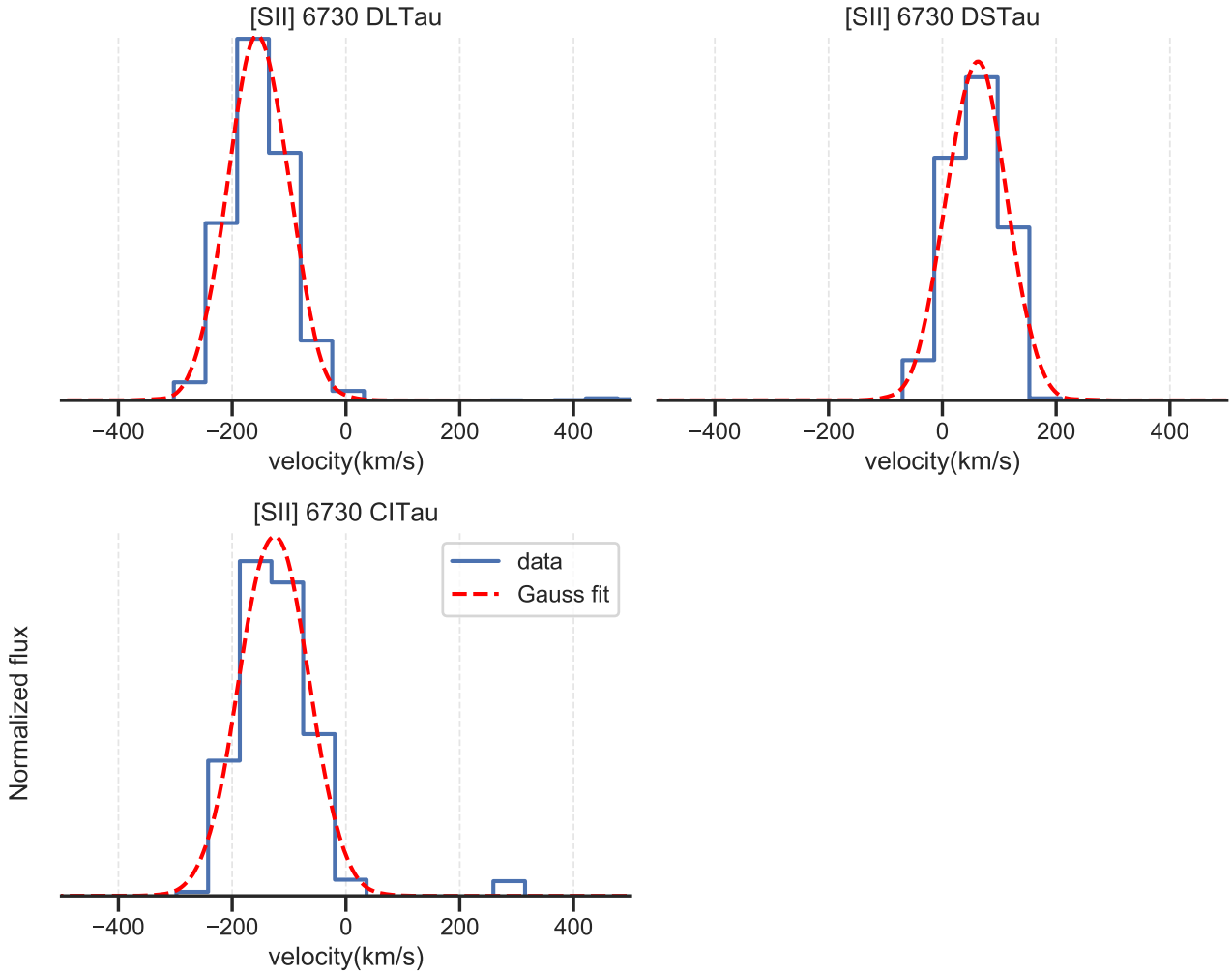

Figure 3.17: [SII]λ6730 line profile identified for DL Tau, CI Tau, and DS Tau.

3.6 What about disk winds?

Disk winds can certainly be present in the forbidden emission lines found in this study. The reason why we do not claim their detection is because of the limited spectral resolution that MUSE provide. In order to analyze disk winds in protoplanetary disks, we need to reach the few tens of km s^{-1} that is required to detect them. The forbidden emission lines with MUSE only have a resolving power between 2381 and 2600, meaning, between 125.9 km s^{-1} to 115.3 km s^{-1} (see Figure 3.19). However, we know that some of the sources analyzed here hosts disk winds in their systems. This is because disk winds have been reported previously using high resolution spectra. The latest contribution is from Banzatti et al. (2019) in which published a big spectral sample of 65 different protoplanetary disks in different molecular clouds. Using the spectral data from Keck-HIRES spectrograph observatory in Mauna Kea in the U.S. state of Hawaii, they track the behavior of four types of [O I] λ6300 LVC: 1) a broad and a narrow component ("BC and "NC" respectively) that is decomposed in two Gaussians that typically have an HVC, 2) single Gaussian in the LVC that is separated between those that have an HVC ("SCJ") and that do not have an HVC ("SC") (Banzatti

et al., 2019). In our sample, DL Tau host a strong HVC > 100 km s^{-1} as well as an HVC < 100 km s^{-1} plus an SCJ$\sim$9 km s^{-1}. On the other hand, RU Lup has a complex line profile which includes a both HVCs and and BC+NC components. Then, DS Tau have been reported with an SC$\sim$1 km s^{-1}, IM Lup with a BC$\sim$-28 km s^{-1}, and IP Tau with a small HVC$\sim$ 34km s^{-1}. Figure 3.18, show their respective spectra. This entail that it is possible that the HVC component we report from MUSE could hide emission from LVC when the down part of the emission line approaches to 0 km s^{-1}.

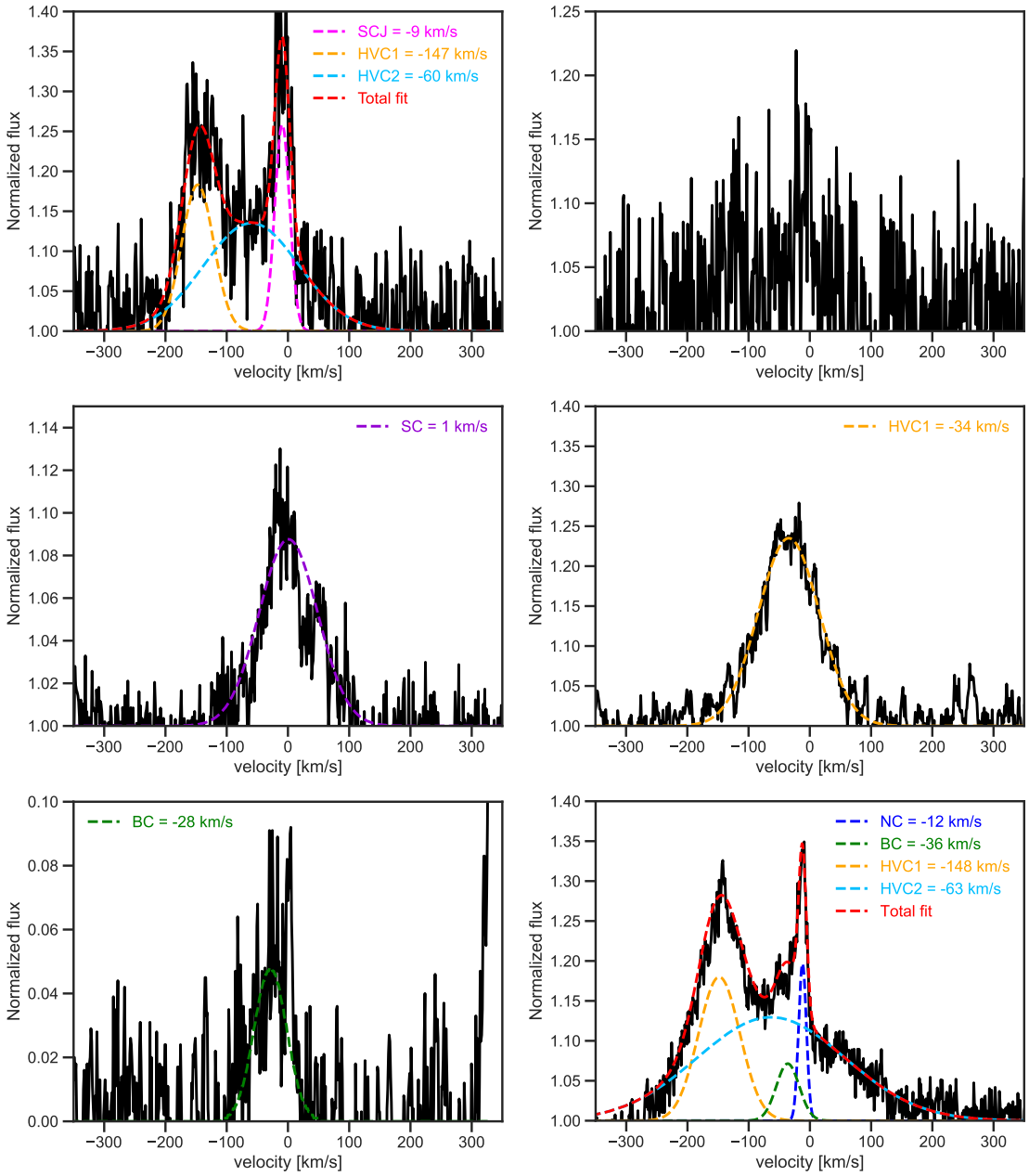

Figure 3.18: Keck-HIRES spectral data of six different protoplanetary disk samples taken from Banzatti et al. (2019). The systems that host disk winds are: DL Tau, DS Tau, IM Lup, and RU Lup. Note that CI Tau have poor signal-to-noise level, and IP Tau does is not reported to have a LVC component.

3.6.1 Resolving the emission lines?

We have classified whether or not the emission lines we report are resolved, marginally resolved, or unresolved (see Table 3.3), depending on the resolution limit that MUSE has at the wavelength of a given emission line (Fig. 3.19). Resolving the line width implies that the emission line width is larger than the line-broadening of MUSE. The [S II] λ6716 line, for example, is marginally equal to the line-broadening FWHM of MUSE (115 km s^{-1}) in DL Tau (Fig.3.20), but in CI Tau is resolved given that the measured width is approximately 150 km s^{-1} (see Fig.3.21) , which is greater than the instrumental resolution. Marginally resolved lines and unresolved lines in particular, should be considered to upper limits rather than precise estimates of the emission line widths (i.e., Eriksson et al., 2020). Note that the Hα line in almost all samples, except in CI Tau, is mostly unresolved, meaning that their measured width is less than or similar to the line-broadening FWHM of MUSE at Hα (119 km s^{-1}). The spectral capability of MUSE has enabled to solve for the velocity components of the forbidden emission lines, leading to a promising venue for the exploration of the momentum transport of the disk as the disk losses mass, in which such estimate depends on the line profile and the resolution limit of the instrument.

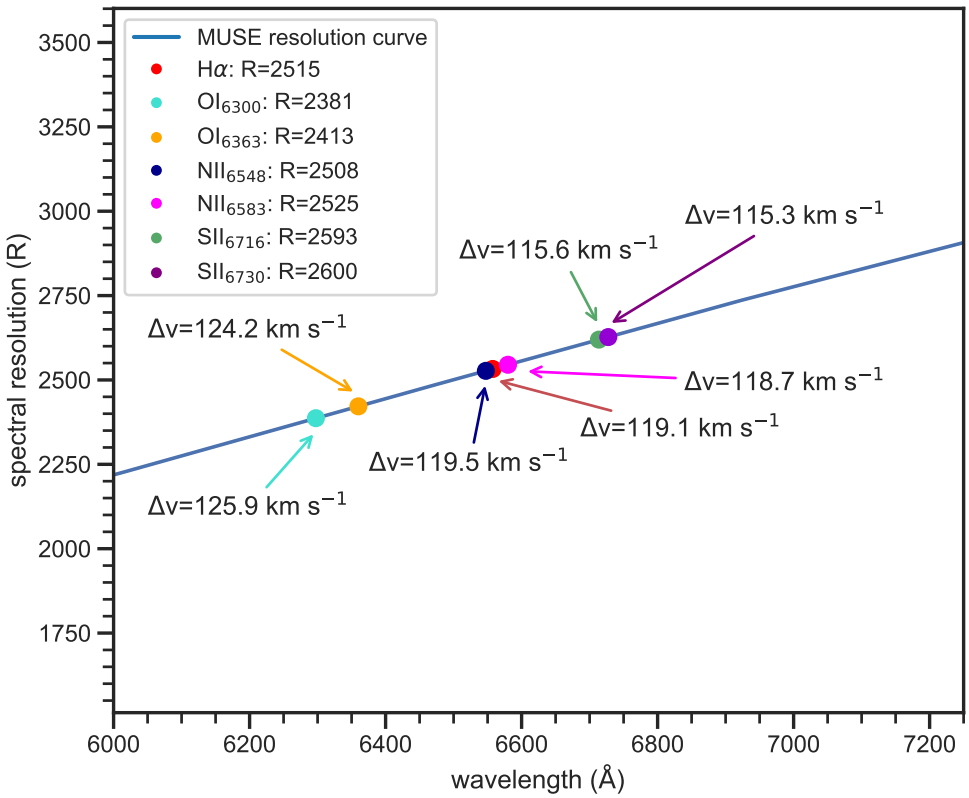

Figure 3.19: Spectral resolution, R=$\lambda/\Delta\lambda$, versus wavelength of the seven forbidden emission lines used in the analysis here. The blue curve shows the resolution curve of MUSE at increments of 500 Å. Each R value for each line is linearly interpolated from the MUSE resolution curve. The values were obtained from the MUSE User Manual (version 11.4, Fig.18).

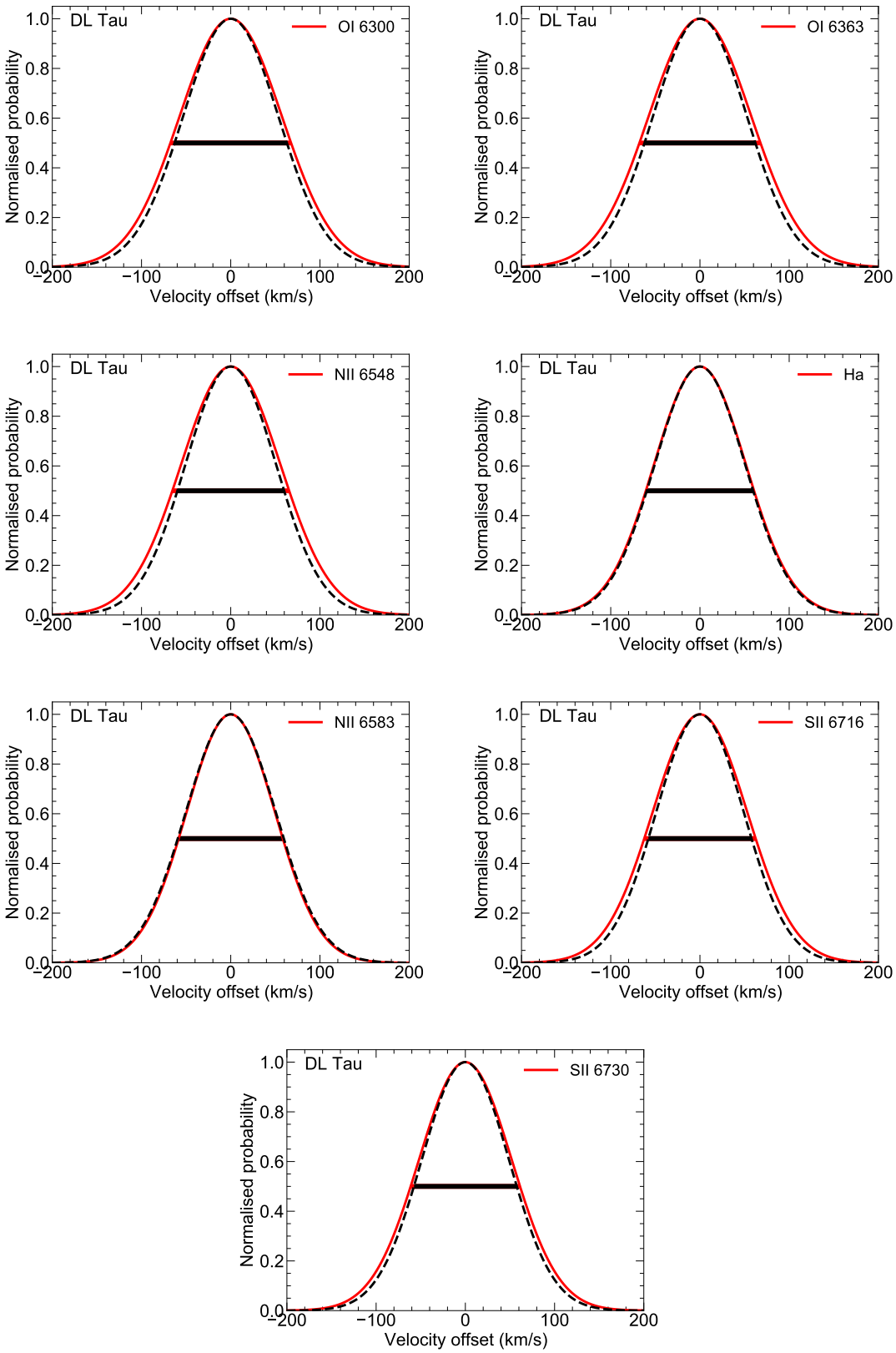

Figure 3.20: DL Tau line widths in red compared to the line-broadening of MUSE in black-dashed line.

Table 3.3: Summary of the spectral width of the disk-outflow/jet systems compared to the line-broadening of MUSE from Fig. 3.19. The λ_{center} refers to the center of the jet area where the flux is brightest.

Source	Line	FWHM $= 2\sqrt{2\log(2)}\sigma$	spatial resolution (mas)	λ_{center} (Å)	line width (km s^{-1})	Resolved?
DL Tau	[O I] λ6300	2.84	71.0	6297.47	135.22	Marginally
	[O I] λ6363	2.87	71.8	6360.69	135.67	Marginally
	[N II] λ6548	2.86	71.5	6544.92	130.89	Marginally
	[N II] λ6583	2.56	64.0	6579.97	116.65	No
	Hα	2.66	66.5	6559.97	121.22	No
	[S II] λ6716	2.79	69.8	6713.38	124.87	Marginally
	[S II] λ6730	2.75	68.8	6727.47	122.54	Marginally
CI Tau	[O I] λ6300	3.38	84.5	6297.71	160.90	Yes
	[N II] λ6583	3.49	87.3	6580.21	158.72	Yes
	[S II] λ6716	3.36	84.0	6713.89	150.17	Yes
	[S II] λ6730	3.43	85.8	6727.71	152.89	Yes
DS Tau	[O I] λ6300	3.02	75.5	6301.51	143.70	Marginally
	[N II] λ6548	3.12	78.0	6550.06	143.18	Marginally
	[N II] λ6583	2.84	71.0	6585.26	129.32	Marginally
	[S II] λ6716	2.59	64.8	6718.01	115.56	No
	[S II] λ6730	2.94	73.5	6732.76	130.87	Marginally
IP Tau	[O I] λ6300	4.30	107.5	6298.50	204.58	Yes
IM Lup	[O I] λ6300	5.51	137.8	6299.17	262.19	Yes
	[N II] λ6583	2.97	74.3	6581.67	135.32	Marginally

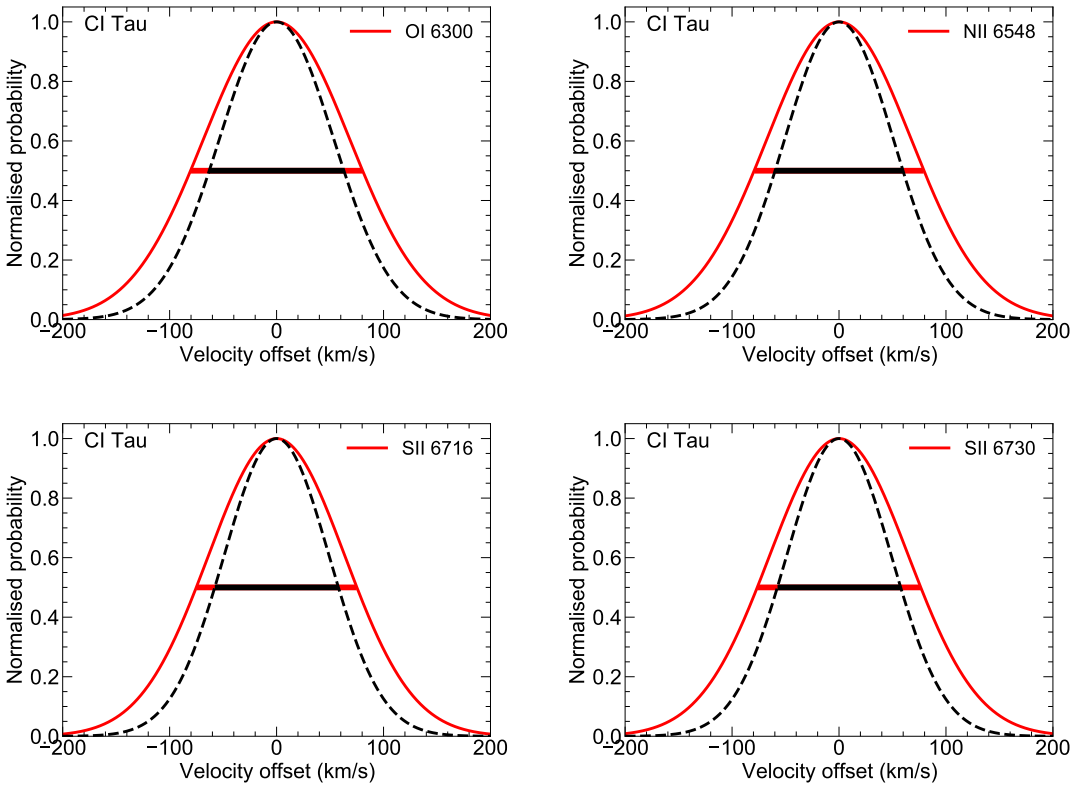

Figure 3.21: CI Tau line widths in red compared to the line-broadening of MUSE in black-dashed line.

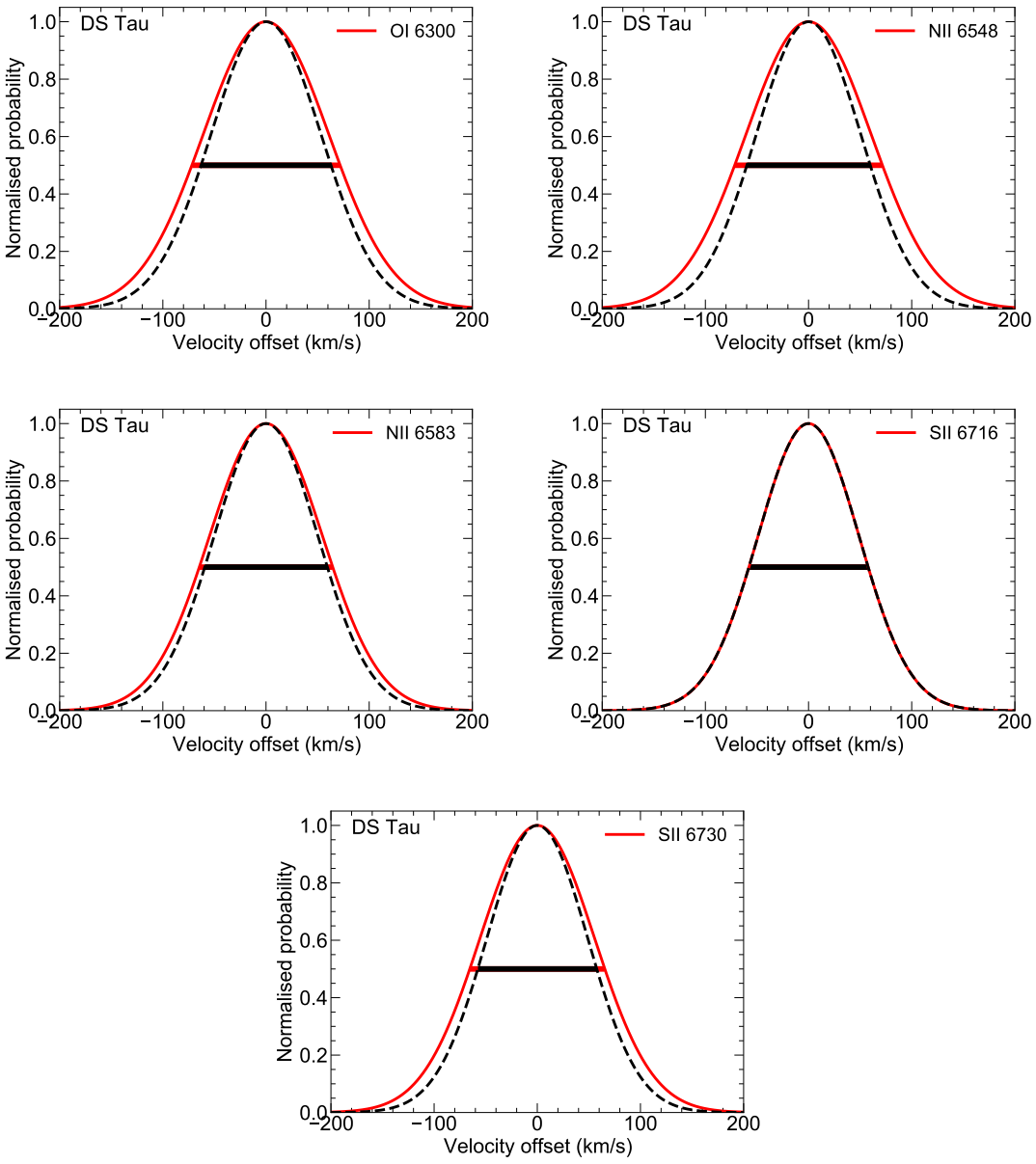

Figure 3.22: DS Tau line widths in red compared to the line-broadening of MUSE in black-dashed line.

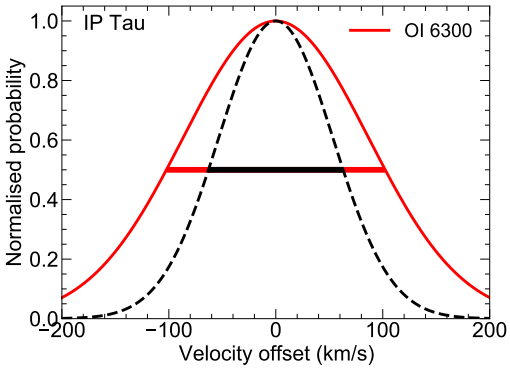

Figure 3.23: IP Tau line widths in red compared to the line-broadening of MUSE in black-dashed line.

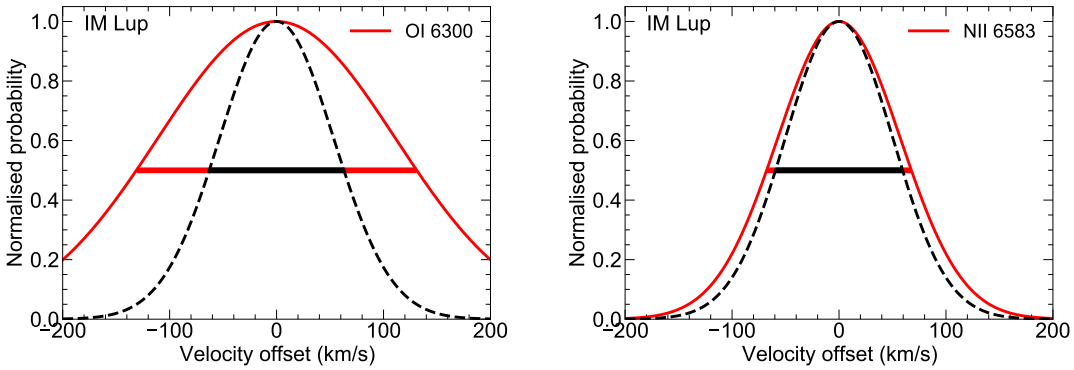

Figure 3.24: IM Lup line widths in red compared to the line-broadening of MUSE in black-dashed line.

3.7 Mass loss rate from line luminosity

The mass loss rate considers the velocity, and the length from the bright [O I]λ6300 line luminosity of the densest bulk of the outflow/jet. The [O I]λ6300 line is optically thin and is used to trace the total mass in the outflow/jet (Hartigan et al., 1994; Giannini et al., 2015; Nisini et al., 2018; Fang et al., 2018). The mass loss rate is

$$\dot{M}_{\rm loss}[M_\odot\ yr^{-1}] = C(T,n_e)\left(\frac{V_\perp}{100\ {\rm km\ s^{-1}}}\right)\left(\frac{l_\perp}{100\ {\rm au}}\right)^{-1}\left(\frac{L_{6300}}{L_\odot}\right) \tag{3.2}$$

where $V_\perp$ is the outflow/jet velocity that is deprojected from the line-of-sight (see Table 3.2). The length of the outflow/jet is $l_\perp = {\rm d_{pc}}\ \theta$ where $\rm d_{pc}$ is the distance of the source given in Table 3.1, and θ is the length of the outflow/jet measured in arsec (see Table 3.4). The length of the jet emission region is measured until the emission flux drops below 10^{-17} erg s^{-1} cm^{-2} Å^{-1}. $C(T,n_e)$ is a coefficient of the [O I] λ6300 line transition from the energy state $2\rightarrow1$, that depends on the gas temperature via thermally excited collisions of electrons. At $T = 10{,}000$ K, we used $C(T,n_e) = 9.0\times10^{-5}$ for a $n_e = 5.0\times10^4$ cm^{-3}, both values provided by Fang et al. (2018). The resulting mass loss rates of the disk-outflow/jet sources are listed in Table.3.4. These mass loss rates range (2-9) $\times10^{-7}$-10^{-8} $M_\odot\ yr^{-1}$ which is in agreement with values reported by Hartigan et al. (1994, 1995); Nisini et al. (2018); Fang et al. (2018). A good advantage of the MUSE data is that the spatial extension of the outflow/jet can be measured. We use the distances of the sources specified in Table 3.1 to convert from angular length (arcsecs) to physical length (au). We adopted the same scaling distance as in Fang et al. (2018) at 100 au as a normalization factor of the extension of the outflow/jet. As noted, the mass loss rate is proportional to the line luminosity of [O I] λ6300 which assumes an ionization fraction that is around 0.1-0.3, a low electron number density that is much lower than the critical density ($n_{\rm H} \sim10^6$ cm^{-3}), and an atomic abundance similar to the standard interstellar medium ($\sim10^{-4}$).

Table 3.4: Mass loss rates for the disk-outflow/jet systems.

Name	log L_{6300} ($L_\odot$)	θ (arcsec)	$l_\perp$ (AU)	$\dot{M}_{\rm loss}$ ($M_\odot\ yr^{-1}$)
DL Tau	-2.20	1.1	180.5	4.6×10^{-7}
CI Tau	-2.99	0.4	60 .8	2.1×10^{-7}
DS Tau	-3.02	0.6	93.6	9.9×10^{-8}
IP Tau	-3.82	0.3	40.8	1.9×10^{-8}
IM Lup	-3.43	0.2	39.8	5.5×10^{-8}

3.8 Outflow/jet width in DL Tau

Fig. 3.25 shows the width of six emission lines of the outflow/jet in DL Tau. The intensity profiles are done by stacking the Gaussian fits of the intensity slices across the outflow/jet as a function of the distance from the outflow/jet axis. The outflow/jet widths in Fig. 3.25 are representative of the average length, namely $\sim$0.5″, of the extension of the outflow/jet in DL Tau. We converted the width of the outflow/jet from pixels using the MUSE spatial resolution of 0.025″ per pixel to angular distance: [O I] λ6300 = 0.16″, [O I] λ6363 = 0.12″, [N II] λ6583 = 0.11″, [S II] λ6716 = 0.31″, [S II] λ6730 = 0.21″, and Hα = 0.17″. Each emission line width in au is shown in the legend box. The only emission line that is not included is the [N II] λ6548 line because it is very faint.

Each line profile traces different layers of the outflow/jet. The [O I] λ6363 line and the [N II] λ6583 line share very similar narrow widths and, compared to the other lines, they both seem to trace the deepest layer of the outflow/jet. These two lines also have similar FWHM (see Table 3.2) encouraging further studies to see if [O I] λ6363 and the [N II] λ6583 could perhaps share the same physical properties of the emitting area. Interestingly, we see similar widths for Hα and [O I] λ6300. On the other hand, we found [S II] λ6716 to be the widest line followed by [S II] λ6730 line.

The brightest and most detected lines are [O I] λ6300 and [N II] λ6583 as a result of collisional excitation of electrons in shock fronts. The [S II] λ6716/[S II] λ6730 and [N II] λ6583/[O I] λ6300 line ratio can help to estimate the physical conditions concurring in these scenarios. Empirical fittings (Proxauf et al., 2014; Ellerbroek et al., 2014) and shock model analysis (Hartigan et al., 1994) suggest that these two line ratios coming from hot and low density regions could have electron densities ranging from 10^3 to 10^4 cm^{-3}, ionization fractions ranging from 0.2 to 10, shock velocities ranging from 60 to 80 km s^{-1}, and magnetic field strengths ranging from 10 to 10^4 μG. Studies of other line ratios also provide useful information on the physical conditions. Previous analysis from the [O I] at λ5577.3 and λ6300.3 line ratio in the LVC emitting region have determined that these are emitted in rather dense gas of $n_e \geq 10^7$ cm^{-3} (or $n_H \geq 10^{10}$ cm^{-3}), where n_e is the electron density and n_H is the gas density relative to hydrogen, and in temperatures between 5000 and 10^4 K, based on models where the excitation energies are due to collisions of electrons in regions dominated by neutral Hydrogen (Natta et al., 2014; Simon et al., 2016; Fang et al., 2018). But regardless of the kinematic components, line ratios seen in LVC could be similar to HVC (Fang et al., 2018), but further analysis should be conducted. Lavalley-Fouquet et al. (2000) mention that from the [N II] λ6583/[O I] λ6300 the line ratio diagnostic, the ratio increases with ionization fraction, in regions where $n_e \geq n_H$. Lavalley-Fouquet et al. (2000) also stated that the [S II] λ6716 and [S II] λ6730 line ratio is a well-known decreasing function of the electronic density until $n_e \geq n_{cr} \sim 10^4$ cm^{-3}, the critical density for collision with electrons of [S II]. We encourage further analysis on the line ratio of these forbidden emission lines in relation to the gas temperature, gas density, electron density, and ionization fraction that is characteristic depending on the region of the emitting area.

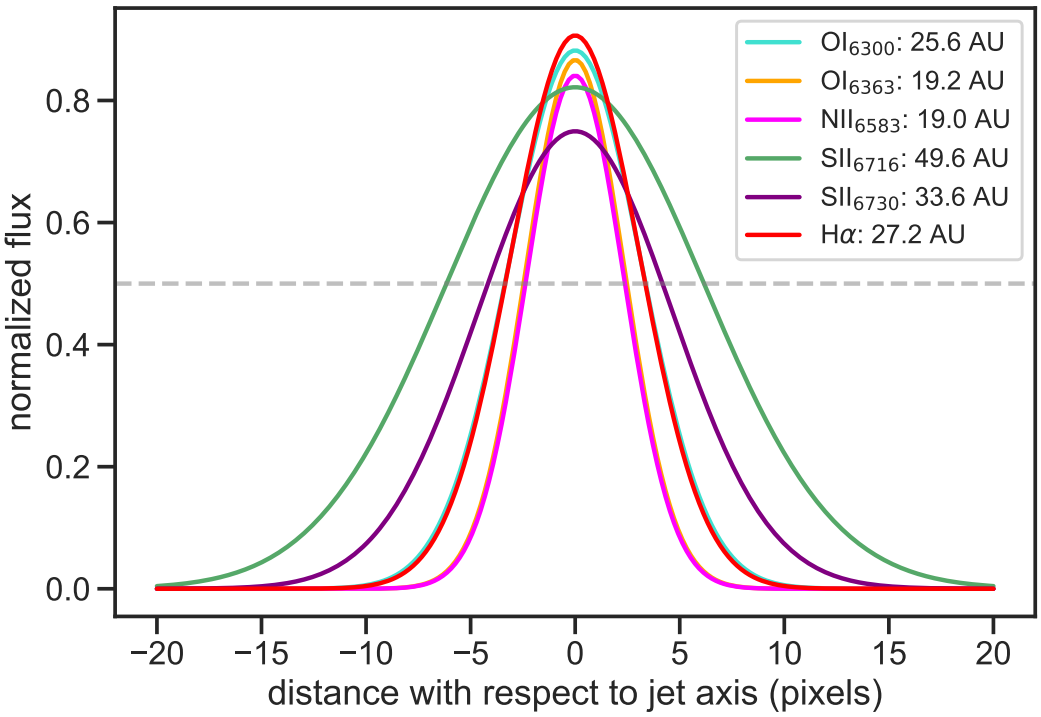

Figure 3.25: Line width profile of the emission lines analyzed in DL Tau. Each line profile is the result of a compilation of the Gaussian fits to intensity slices across the outflow/jet and their maximum intensity peaks are centered at the jet axis. The width of the outflow/jet, in au, is shown in the legend box.

3.9 Jet wiggles, a sign of jet precession?

The outflows/jets show different morphologies. When plotting the Gaussian centers in Fig. 3.26, it seems that, jets that are not too collimated, the amplitude of the wiggles is higher and asymmetric. As the wiggles do not show any clear periodic pattern, these are not associated with any inner disk misalignment. By investigating if there are any photometric variations in the inner disk of these sources could help us understand better whether or not there could be a body orbiting close to the central star (Petrov et al., 2001; Cody & Hillenbrand, 2018). Instead, these are distinctive to the jet launching and evolution mechanism. Fully 3D simulations of MHD jet launching in young binaries, considering tidal forces (Sheikhnezami & Fendt, 2015, 2018), find that inner disks will be warped and that the jet axis, which remains perpendicular to the disk, is subsequently re-aligned as a consequence of the disk precession. The angle of the jet precession cone derived is small and about 8° but it could be much less, perhaps close to the differences between position angles identified here, for T Tauri systems. However, their simulation was run only for one binary orbit and thus could not follow a whole precession period. Similar simulations, run in hydrodynamics, but with forced precession of the jet nozzle, were applied for the precession jet source SS 433(Monceau-Baroux et al., 2014), for example. These simulations show that the expected sinusoidal pattern of jet propagation varies along the jet, with larger amplitude and wavelength for larger distances, similar to our data indicating a jet cone opening up with distance. Further, more complex

model fitting may be necessary in order to derive a conclusive statement about precession.

As an alternative to a precession of the jet axis, a jet kink instability could be the cause of the wiggling jet structure. Depending on the jet magnetization this instability limits the expansion of the jet (Moll et al., 2008). As we do not know the magnetic field structure and strength, making a statement about the viability of kink modes in jets is difficult.

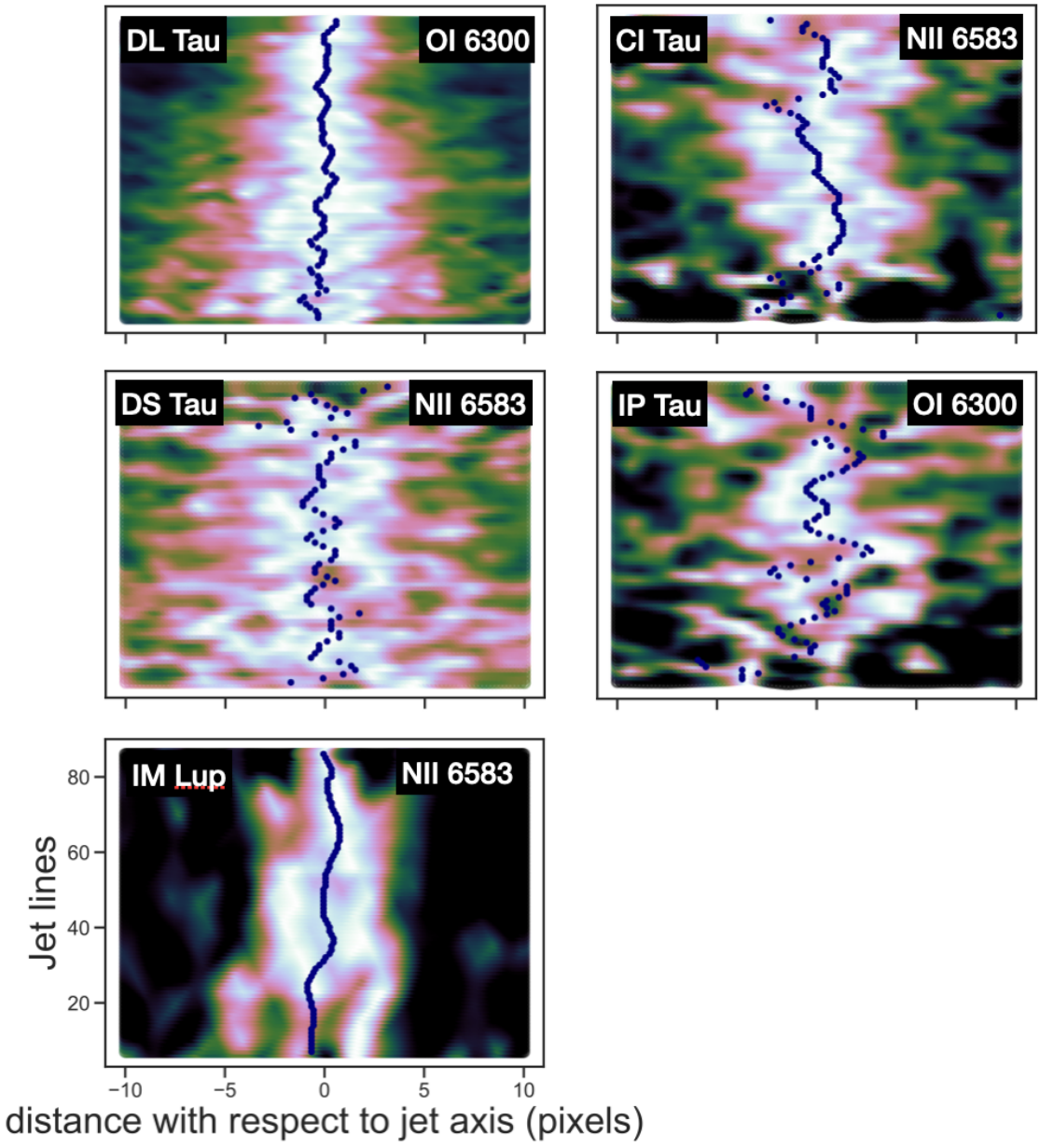

Figure 3.26: Successive Gaussian centers in navy-colored dots. Wiggles are seen in DL Tau and IP Tau at [O I] λ6300, and for CI Tau, DS Tau, and IM Lup at [N II] λ6583.

3.10 Physical conditions from shock diagnostic

The forbidden emission lines along the outflow/jet are a result of collisional excitation reactions in shock fronts. Another way to estimate the mass loss rate of the outflow/jet is by the analysis of the line ratios such as [N II]6583/[O I]6300 and [S II]6716/[S II]6730. To obtain the flux values for each line ratio we perform an aperture sum in the area of the outflow/jet that correspond to the post-shock front. A secondary aperture sum is done outside of the outflow/jet to quantify the flux error that correspond to the most part as background noise.

The electron density is then estimated by [S II]6716/[S II]6730 ratio. We followed the empirical fit from equation 3 in Proxauf et al. (2014) deduced at T = 10,000 K

$$log(n_e[cm^{-3}]) = 0.0543 \tan(-3.0553\ R + 2.8506) + 6.98 - 10.6905\ R + 9.9186\ R^2 - 3.5442\ R^3 \tag{3.3}$$

where R is the [S II]6716/[S II]6730 ratio. The pre-shock number density, magnetic field strength, and the shock velocity can be estimated from Figure 3 from Ellerbroek et al. (2014). These pre-shock parameters were corroborated with the shock model as predicted by Hartigan et al. (1994) (see Figure 11). The average mass flux of these line ratio can be estimated from the pre-shock density ($N_{\rm preshock}$) and the post-shock density ($N_{\rm postshock}$) so the mean hydrogen density is estimated as (Hartigan et al., 1994)

$$< N >= (N_{\rm preshock} \times N_{\rm postshock})^{1/2} =< C >^{-1/2}\ \ N_{\rm postshock} =< C >^{1/2} < I >^{-1}\ \ n_{\rm e} \tag{3.4}$$

where $< C >$ is the compression behind the shock, $< I >$ is the ionization fraction, and $n_{\rm e}$ is the observed electron density in the postshock gas. The $< C >$ and $< I >$ are represented as the averaged weighted by the flux of the [S II] lines. The ionization fraction is the defined as the ratio of the electron density measured from the [S II] lines to the total density (Hartigan et al., 1994). Then, the mass loss rate

$$\dot{M}_{\rm line-ratio}[M_\odot\ yr^{-1}] = \mu m_H < N > v_{\rm outflow/jet} A \tag{3.5}$$

where μ=1.24 is the mean molecular weight for gas with molecular abundances, m_H is the hydrogen mass, the $v_{\rm outflow/jet}$ is the deprojected outflow/jet velocity (as in Table 3.2), and A is the area of the aperture where we quantify the emission in the outflow/jet. The $\dot{M}_{\rm line-ratio}$ and the physical parameters values for each source are specified in Table 3.5, 3.6, 3.7, 3.8, and 3.9. The [O I]6300 and [N II]6583 were the two brightest and most observed lines in our sample. In general, these estimates interestingly tell us crucial information about the physical conditions that dominate in protoplanetary disks. In summary, the line ratio help us estimating that in protoplanetary disks:

- electron density: $10^3 - 10^4$ cm^{-3}
- ionization fraction: 0.2-15

Table 3.5: DL Tau line ratios and physical conditions.

Line ratios	
[S II]6716/[S II]6730	0.57± 0.65
[N II]6583/[O I]6300	0.92± 0.014
Physical conditions	
Position	0.987″
R_{jet}(au)	22±16
n_e (cm^{-3})	36453±2051
$n_{H,pre}$ (cm^{-3})	1000
B (μG)	100
v_{shock} (km s^{-1})	∼60
$< I >$	0.23±0.3
$< C >$	13±10
$< n_H >$ (cm^{-3})	4395.8±966
$\dot{M}_{line-ratio}$ (10^{-10} $M_\odot$ yr^{-1})	9.8±0.76

Notes. The detailed derivation is in the main text.

B were depicted from Fig.3 from Ellerbroek et al. 2014.

Other parameters are based on shock models from Hartigan et al. 1994.

The n_e were obtained from Proxauf et al. 2014.

Table 3.6: CI Tau.

Line ratios	
[S II]6716/[S II]6730	0.55± 0.65
[N II]6583/[O I]6300	0.83± 0.92
Physical conditions	
Position	0.496″
R_{jet}(au)	19.7±16
n_e (cm^{-3})	4356.6±2051
$n_{H,pre}$ (cm^{-3})	1000
B (μG)	1000
v_{shock} (km s^{-1})	∼70
$< I >$	0.31±0.2
$< C >$	13±8.5
$< n_H >$ (cm^{-3})	3897.8±2932.3
$\dot{M}_{line-ratio}$ (10^{-10} $M_\odot$ yr^{-1})	6.72±1.1

- shock velocity: 60-80 km s^{-1}
- Hydrogen number density (pre-shock): $10^2 - 10^4$ cm^{-3}
- magnetic field strength: 10-1000 μG

Table 3.7: DS Tau.

Line ratios	
[S II]6716/[S II]6730	0.66± 1.4
[N II]6583/[O I]6300	2.21± 2.2
Physical conditions	
Position	0.496″
R_{jet}(au)	26±16
n_e (cm^{-3})	1930.8±22.6
$n_{H,pre}$ (cm^{-3})	1000
B (μG)	100
v_{shock} (km s^{-1})	∼55-60
$< I >$	15±0.3
$< C >$	13±1.0
$< n_H >$ (cm^{-3})	3570.1±13.3
$\dot{M}_{line-ratio}$ (10^{-10} $M_\odot$ yr^{-1})	9.31±0.66

Table 3.8: IP Tau.

Line ratios	
[S II]6716/[S II]6730	0.31± 0.80
[N II]6583/[O I]6300	0.64± 1.2
Physical conditions	
Position	0.189″
R_{jet}(au)	12.2±16
n_e (cm^{-3})	22718.2±158.3
$n_{H,pre}$ (cm^{-3})	100
B (μG)	100
v_{shock} (km s^{-1})	∼60
$< I >$	0.22±0.5
$< C >$	3.5±16
$< n_H >$ (cm^{-3})	3469.5±79.2
$\dot{M}_{line-ratio}$ (10^{-11} $M_\odot$ yr^{-1})	9.73±1.3

Table 3.9: IM Lup.

Line ratios	
[S II]6716/[S II]6730	0.45± 0.48
[N II]6583/[O I]6300	1.24± 1.1
Physical conditions	
Position	0.234″
R_{jet}(au)	16.5±16
n_e (cm^{-3})	26557.9±10696.3
$n_{H,pre}$ (cm^{-3})	10000
B (μG)	100
$v_{\rm shock}$ (km s^{-1})	∼90
$< I >$	0.33±0.1
$< C >$	60±10
$< n_H >$ (cm^{-3})	10389.7±3760.1
$\dot{M}_{\rm line-ratio}$ (10^{-10} $M_\odot$ yr^{-1})	7.12±1.0

Table 3.10: RU Lup.

Line ratios	
[S II]6716/[S II]6730	0.91± 0.49
[N II]6583/[O I]6300	0.77± 0.92
Physical conditions	
Position	0.692″
R_{jet}(au)	40.6±16
n_e (cm^{-3})	1097.8±605.6
$n_{H,pre}$ (cm^{-3})	1000
B (μG)	10
$v_{\rm shock}$ (km s^{-1})	65
$< I >$	0.24±0.04
$< C >$	60±10
$< n_H >$ (cm^{-3})	590.5±258.5
$\dot{M}_{\rm line-ratio}$ (10^{-10} $M_\odot$ yr^{-1})	3.71±1.6

3.10.1 Mass loss rate: line luminosity vs. shock diagnostic

This $\dot{M}_{\rm line-ratio}$ method differs from the $\dot{M}_{\rm loss}$, used in equation 3.2 from §3.7, based on a couple of assumptions as described by Hartigan et al. (1994). Both, the $\dot{M}_{\rm loss}$ rate and the $\dot{M}_{\rm line-ratio}$ rate, assume that the mass flux is averaged in the outflow/jet. The mass flux from line luminosity method, though, tends to be higher as it refers to the densest part of the flow. On the other hand, the mass flux from shock diagnostic is concentrated in the area where the maximum emission is coming out of the outflow/jet that traces the post-shock front. The shock diagnostic method assumes that the outflow/jet is uniform at the electron density characterized by a single shock velocity. The electron density calculated from the [S II] lines are essentially the same for [O I] line emitting region because the [O I] radiate more or less in the same region of the post-shock gas. In summary, both mass loss methods should not differ from the physical estimations based on the electron density and ionization fraction. However, since MUSE provides and imaging glimpse of the emitting region of the outflow/jet, both mass loss rate methods could differ from each other when considering the great extension of the outflow/jet, that is considerably larger than the cross sectional area used from shock diagnostic. Finally, both methods are independent from the physical mechanisms that produces the shock emission lines.

3.11 Mass accretion

These systems are thought to be accreting material constantly from the inner disk onto the star. Although the stellar mass, luminosity, and temperature might strongly influence and be the responsible one for the flux emission that is coming in the inner disk through either MHD winds, outflows/jets, and mass accretion onto the star, our understanding of the nature of these forbidden emission lines and the stellar properties dependence is limited as it is unclear what is the strength of the magnetic field in the inner disk for T Tauri sources. The mass accretion of a T Tauri source can be estimated from the 10% Hα line width (Xie et al., 2020).

$$log(\dot{M}_{\rm acc}[M_\odot\ yr^{-1}]) = -12.89(\pm0.3) + 9.7(\pm0.7) \times 10^{-3}{\rm H}\alpha(10\%) \tag{3.6}$$

where the Hα(10%) is the full width at 10% maximum of Hα line in km s^{-1} (Natta et al., 2004). The Hα stellar emission is obtained before the PSF subtracted cube. Figure 3.27 show the intrinsic stellar Hα(10%) for each source. Figure 3.28 (*top*) shows the mass loss ratio of the sources analyzed here. The $\dot{M}_{\rm jet}$ is the $\dot{M}_{\rm line-ratio}$ from shock diagnostic. The upper limits on each source points towards lower efficiency of the mass loss from the outflow/jet. The $\dot{M}_{\rm jet}/\dot{M}_{\rm acc}$ of 0.3 agrees with large statistical samples (0.01-0.5; Natta et al. (2014)). Figure 3.28 (*bottom*) shows the dependence of the $\dot{M}_{\rm jet}/\dot{M}_{\rm acc}$ ratio with $\dot{M}_{\rm acc}$ to be scattered. The sources that have $\dot{M}_{\rm acc}$ between $\sim 10^{-7}\ M_\odot\ yr^{-1}$ have a $\dot{M}_{\rm jet}/\dot{M}_{\rm acc}$ ratio between 0.03 and 0.01 are high accretors. Lower accretors are located above the $\dot{M}_{\rm jet}/\dot{M}_{\rm acc}$ ratio of 0.3. We see the same tendency as shown in Natta et al. (2014) for a larger sample.

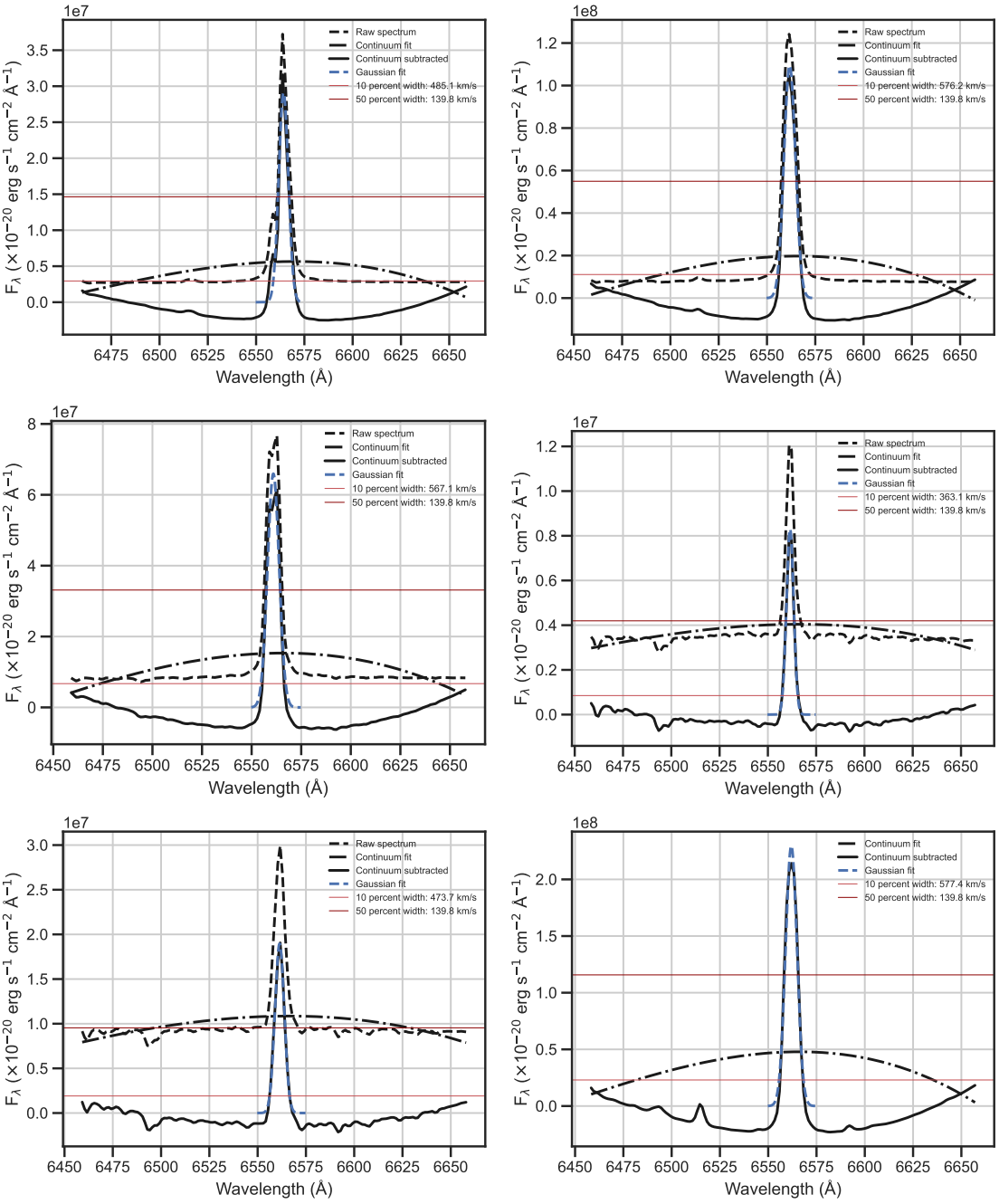

Figure 3.27: Hα stellar emission for each source. The 10% width of Hα is given by the red line.

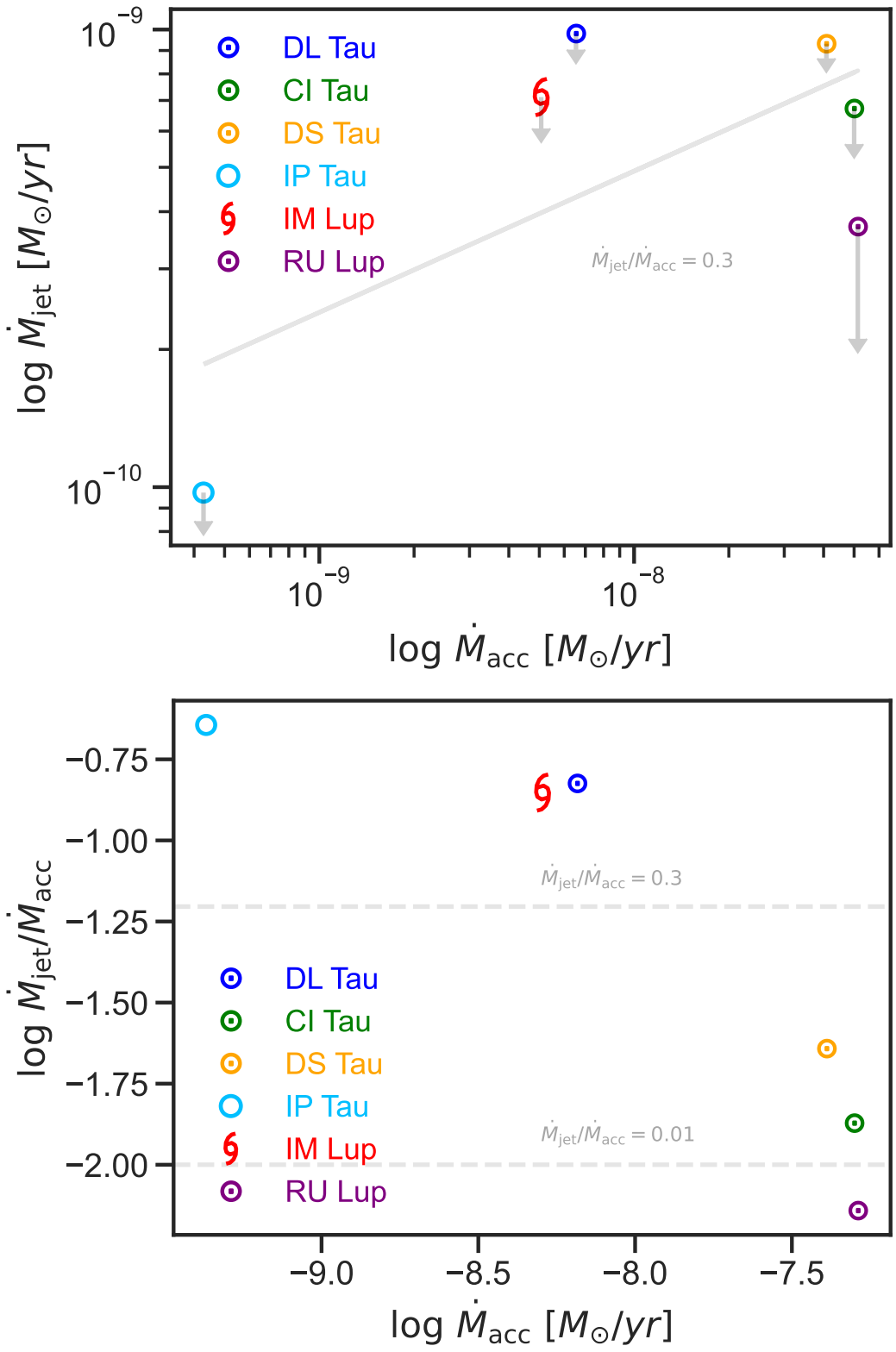

Figure 3.28: *Top.* Mass loss ratio of the source analyzed here. The $\dot{M}_{jet}$ is the $\dot{M}_{line-ratio}$. *Bottom.* $\dot{M}_{jet}/\dot{M}_{acc}$ ratio plotted as a function of the mass accretion rate.

3.12 Luminosity accretion

For every mass accretion value there is a luminosity accretion associated which represent most of the luminosity in the inner disk. The luminosity accretion of a T Tauri source can be empirically measured in two ways: 1) by fitting the spectrum of each class II source to the sum of the photospheric spectrum of a class III source template and the emission of a slab of Hydrogen, then, the best stellar and accretion parameter is the fit that minimizes the χ^2 distribution, as described in Alcalá et al. (2017); 2) is by using the mass accretion and luminosity accretion relation

$$L_{\rm acc}[L_\odot] = \frac{\dot{M}_{\rm acc}}{1.25}\frac{GM_*}{R_*} \tag{3.7}$$

where R_* is the stellar radius and stellar mass are obtained from Banzatti et al. (2019) and Fang et al. (2018). The 1.25 factor includes the truncation radius of the disk that is assumed to be $5R_*$ (Gullbring et al., 1998). The log [O I]λ6300 luminosity has been used to diagnose the presence of HVC for strong outflows and LVC associated with disk winds in protoplanetary disk. We consider the log [O I]λ6300 luminosity for HVC as a function of luminosity accretion and stellar mass obtained from Nisini et al. (2018) and Fang et al. (2018). Figure 3.29 show the [O I]λ6300 luminosity for HVC including the MUSE sources reported here that correlates well with luminosity accretion and stellar mass. When performing the linear regression we found that the [O I]λ6300 luminosity for HVC correlates with $L_{\rm acc}$ as

$$\log(L_{\rm OI6300})[L_\odot] = -3.94 + 0.68\ \log(L_{\rm acc}), r = 0.71 \tag{3.8}$$

and the [O I]λ6300 luminosity for HVC correlates with M_* as

$$\log(L_{\rm OI6300})[L_\odot] = -6.02 + 2.09\ \log(M_*), r = 0.59 \tag{3.9}$$

where r is the correlation factor between $L_{\rm acc}$ and M_*, and the [O I]λ6300 luminosity for HVC. This value means that the proportion of the variance in the [O I]λ6300 luminosity can be explained by both, the $L_{\rm acc}$ and the M_*, in the regression model. With the MUSE data, the $L_{\rm OI6300}$ versus the $L_{\rm acc}$ slope is slightly lower but very close to the one (0.72±0.07) in Fang et al. (2018) and (0.75±0.08) in Nisini et al. (2018). We also noticed that the $L_{\rm OI6300}$ versus the M_* relation is more scattered compared to the $L_{\rm acc}$. In summary, this correlation holds better for $L_{\rm acc}$ that is most likely coming from the EUV luminosity from accretion (Ercolano & Owen, 2016).

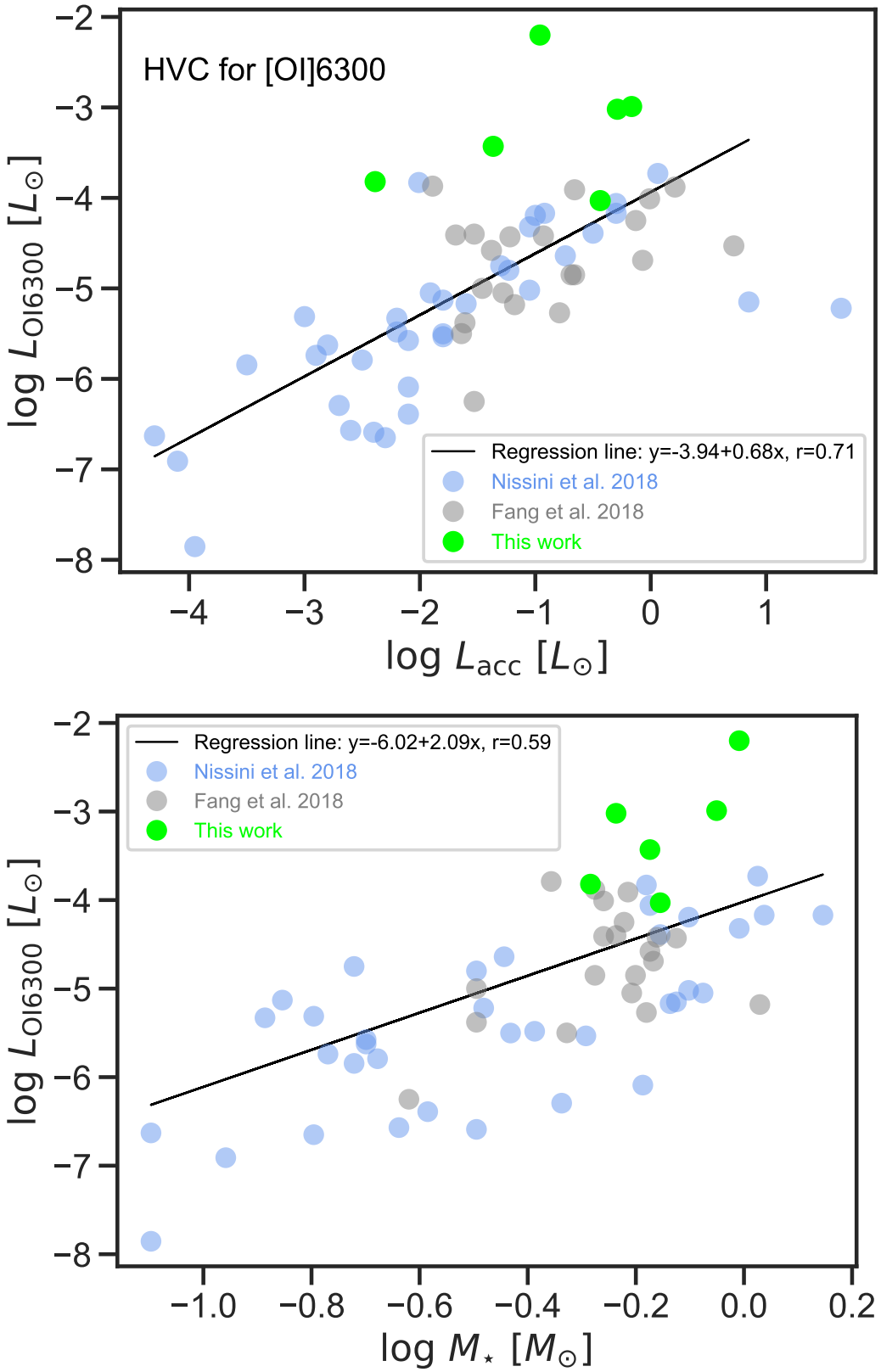

Figure 3.29: *Top.* The log [O I]λ6300 luminosity for HVC as a function of luminosity accretion. *Bottom.* The log [O I]λ6300 luminosity for HVC as a function of the stellar mass. The black solid line in both represents the linear regression described in the legend box.

Table 3.11: Stellar mass, radius, and luminosity of the MUSE sources analyzed here.

Source	M_* ($M_\odot$)	R_* ($R_\odot$)	L_* ($L_\odot$)
DL Tau	0.98	1.47	0.65
CI Tau	0.89	1.64	0.81
DS Tau	0.58	1.16	0.25
IP Tau	0.52	1.37	0.34
IM Lup	0.67	1.98	0.98
RU Lup	0.70	2.48	0.69

Notes. The M_*, R_* and L_* are obtained from Long et al. (2019), and Banzatti et al. (2019). For IM Lup we use Fang et al. (2018).

3.13 Different disk dispersal scenarios

In this section, we briefly present the different disk dispersal scenarios that have been determined before for other forbidden emission line studies detected for many other T Tauri sources (Banzatti et al., 2019). We adopt the same explanation to describe what scenario we found for our sources. From Figure 3.30 our HVCs reported for DL Tau and RU Lup are hosting strong outflow/jets while, at the same time, being supported by MHD winds because of their LVC-narrower and LVC-broader profile reported by Banzatti et al. (2019), respectively. Since Banzatti et al. (2019) did not classify CI Tau because of the low signal-to-noise level, we think the strong HVC reported could also be supported by MHD winds. It is harder for the other sources with less strong HVCs to link the HVC with the LVC detection scenarios. DS Tau seems to host an extended outflow/jet, but because its disk high inclination, it is hard to disentangle to LVC components. For IM Lup, it is unclear also because it is the source we report with the lowest signal-to-noise. However, judging from the very low extension of the emission at the center, it could be said that the LVC component is emitting from a small radius of the star. IP Tau, though, is a transition disk with HVC characteristics, and no LVC has been reported, which makes this source special since outflows/jets are detected where their inner disk is not depleted.

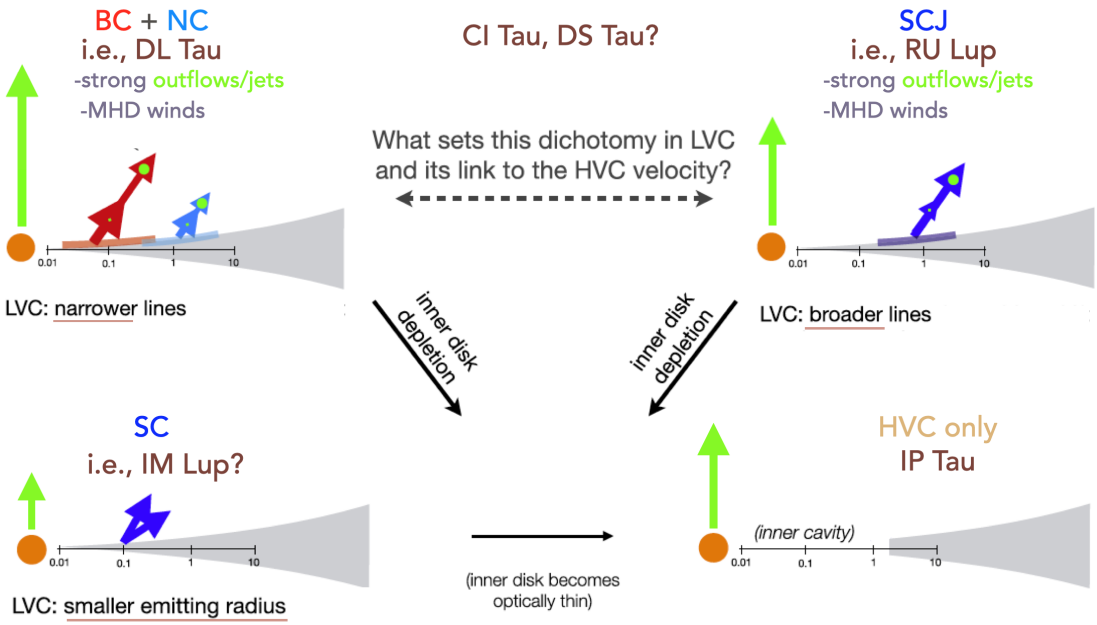

Figure 3.30: We adopt our HVCs sources with this artistic representation to explain the different mechanisms of disk dispersal in combination with previously reported LVCs. Image idea credit from Banzatti et al. (2019).

3.14 Conclusions

We have analyzed spatially resolved [O I] $\lambda\lambda$6300, 6363, [N II] $\lambda\lambda$6548, 6583, Hα, and [S II] $\lambda\lambda$6716, 6730 emission lines in five T Tauris: DL Tau, CI Tau, DS Tau, IP Tau, and IM Lup host outflows/jets. We conduct an analysis to estimate the $PA_{outflow/jet}$ of the emission lines coming from the innermost region of the disk. The average of the position angles for different emission lines is used to compare with the PA_{dust} from the outer disk obtained by previous work. We also performed a simple kinematic analysis to describe the velocity components of the line profiles, and the line width of the outflow/jet in DL Tau. We finally calculated the mass loss rate of the outflow/jet by using the [O I] λ6300 line based on physical parameters derived in this work. Our main conclusions are summarized as follows:

1. The $PA_{outflow/jet}$ values are in good agreement, differences are less than 1° except for IM Lup that is 2.9°, with the previously determined PA_{dust}. Therefore, we do not find evidence for a potential misalignment of the inner disk with respect to the outer disk.

2. The DL Tau and CI Tau emission lines are strongly blue-shifted showing a velocity profile greater than 200 km s^{-1} associated to strong outflows/jets. IP Tau, DS Tau, and IM Lup emission lines are less shifted and closely probing low-velocity components that are more associated with outflows and winds. The velocity components exhibit very distinctive and different outflows/jets and winds morphology in their systems.

3. The line width of the emission lines in DL Tau probes different layers in the outflow/jet, with the [O I] λ6363 line and the [N II] λ6583 line probing the deepest layer and the

[S II] λ6716 line and the [S II] λ6730 line probing the widest layer. The [O I] λ6363 and [N II] λ6583 lines have very similar widths as well as Hα and [O I] λ6300 lines hinting to certain correlation in the ionization fraction and electronic density functions as mentioned in Lavalley-Fouquet et al. (2000).

4. Our estimated values for the mass loss from line luminosity agree to be in the order of (2-9) $\times 10^{-7}$-10^{-8} $M_{\odot}\ yr^{-1}$, including the measurement of the length of the outflow/jet. The mass loss from shock diagnostic is $\times 10^{-11}$-10^{-10} $M_{\odot}\ yr^{-1}$ comparable to previous works for other sources and instruments.

5. The brightest emission lines reported are [N II] λ6583 and [O I] λ6300 suggesting that these environments are highly ionized with an electron density of $10^3 - 10^4$ cm^{-3}, ionization fraction of 0.2-15, Hydrogen pre-shock number density of $10^2 - 10^4$ cm^{-3}, and a magnetic field strength of 10-10,000 μG.

4 Disk Dynamics and Photoevaporation modeling

"If I have seen further, it is by standing on the shoulders of Giants."

by Isaac Newton

4.1 Context

So far, we have seen how the gas dynamics control the turbulence in protoplanetary disks. From the first chapter, we predict that the VSI and the influence of stellar radiation, including X-ray, EUV, and FUV photons, could join forces to outflow gas in the form of mass loss from photoevaporation. In chapter 2, we learned that forbidden emission lines are one key diagnostic of the mass loss in the disk. The motivation of this chapter is to address, from a theoretical point of view, the understanding of the physical and chemical mechanisms that potentially cause the launch of disk winds in very hot and low-density regions in the disk.

Besides planets, other mechanisms that shape the disk evolution are viscosity and mass loss in the form of winds. In the context of accretion disks, the radially outward transport of angular momentum is mainly controlled in regions where the MRI is active, where MHD winds could be generated (Hawley et al., 1995) proven in both local 3D simulations (Suzuki & Inutsuka, 2009) and from a global perspective (Zhu & Stone, 2018). The loss of angular momentum from the disk to the wind is mediated by the vertical gradient of the toroidal B_ϕ component, where the torque in the vertical direction is accelerated at the disk surface (Wardle & Koenigl, 1993; Ferreira & Pelletier, 1995; Ferreira, 1997). Global non-ideal MHD simulations with self-consistent stellar radiation, diffusive re-radiation, thermochemistry, and ambipolar diffusivity coincide with the wind base being around the same location as the FUV-heating layer (Bai, 2017; Béthune et al., 2017; Gressel et al., 2020; Wang et al., 2019). These simulations evolve around a weak magnetic field.

The inclusion of thermal effects at the surface of the disk is of great importance since it could add distinctive wind features (Gressel et al., 2020). While MHD effects play a crucial role in the transport of the angular momentum of the disk, photoevaporative winds are thought to be most responsible for the disk dispersal (Hollenbach et al., 1994). Photoevaporative winds are purely thermally-driven winds caused by the strong influence of stellar

X-ray, EUV, and FUV photons. They are merely atomic, ionic, or molecular gases heated and expanded above the disk surface. These winds do not play a role in the transport of the angular momentum in the disk but can affect other physical mechanisms that drive the transport of the angular momentum in the disk. There have been significant advancements in simulations that couple thermochemistry, stellar radiation, and hydrodynamics that are relevant for photoevaporative winds (Nakatani et al., 2018a,b; Haworth & Owen, 2020). The mass loss rate, the main dispersal factor in the disk, is sensitive to stellar irradiation. The presence of disk winds have been diagnosed in atomic/ionic form as [O I] at 6300 Angstrom (Rigliaco et al., 2013; Natta et al., 2014; Simon et al., 2016; Nisini et al., 2018; Banzatti et al., 2019), [C I] (J=1-0) at 492 GHz (Haworth & Owen, 2020), as well as, in ionic molecular form as HCO^+ (J=4-3) at 356.73 GHz (Drabek-Maunder et al., 2016), and in rotational molecular form CO (J=2-1) at 230 GHz from mm/sub-mm wavelengths (Klaassen et al., 2013). Also, disk winds have been detected in IR emission lines as Ne II 12.8 μm (Pascucci et al., 2011), and CO (ν=1-0) M band around 4.7 μm (Banzatti & Pontoppidan, 2015). Recently, Valegård et al. (2022) stated that dusty winds could be responsible for optical effects seen in SPHERE/VLT at I-band and H-band to explain the elevated dust above the disk.

The physics that describes the thermochemical conditions that occur during photoevaporation processes have been determined by previous work. This chapter presents a description of the work in progress for the following paper that is soon to be published (Flores-Rivera et al. *inPrep.*). Here we revise the gas dynamic configuration used in chapter 1 and include an extra physical term, that is, the radiation pressure in our energy conservation in the equation of fluid dynamics, and analyze the thermodynamical response of the gas of a classical T Tauri system.

4.2 Numerical methods

For the gas and thermodynamics motion we employ PLUTO 4.3 code (Mignone, 2007). The numerical set up is the same as Flores-Rivera et al. (2020) using the second-order piece-wise linear spatial reconstruction method, the HLL Riemann solver and Runge-Kutta for the flux time integration. The CFL is set to 0.25. The system of equations reads

$$\frac{\partial \rho}{\partial t} + \nabla \cdot (\rho \mathbf{v}) = 0, \tag{4.1}$$

$$\frac{\partial (\rho \mathbf{v})}{\partial t} + \nabla \cdot (\rho \mathbf{v}\mathbf{v}) + \nabla P = -\rho \nabla \Phi \tag{4.2}$$

$$\frac{\partial E}{\partial t} + \nabla \cdot [(E + P)\mathbf{v})] = -\rho \mathbf{v} \cdot \nabla \Phi \tag{4.3}$$

where $E = \rho\epsilon + 0.5\rho\mathbf{v}^2$ is the total energy of the system. The conservation of energy (equation 4.3) is now represented as the volume integral of the specific energy and the kinetic energy plus the second term, which is the advection of energy and the pressure through the

control volume surface. The ideal equation of state provides the relationship between the gas pressure and the internal energy as $P = (\Gamma - 1)\rho\epsilon$, where Γ is the adiabatic index. Adopting the ideal gas equation of the state where the pressure is in the form of

$$P = \frac{\mathcal{R}}{\mu} T\rho \tag{4.4}$$

where ρ is the gas density, $\mathcal{R}$ is the ideal gas constant, T is the gas temperature, μ is the mean molecular weight. To correct for radiative effects through the gas temperature, we need to adapt the conservative quantity that represent the thermal energy in PLUTO as the thermal pressure. The thermal pressure over time is described as

$$\frac{dP}{dt} = \frac{\mathcal{R}\rho}{\mu} \frac{T - T_{\rm eq}}{\tau_{\rm cooling}} \tag{4.5}$$

where T is the gas temperature from PLUTO, $T_{\rm eq}$ is the equilibrium temperature, $\tau_{\rm cooling}$ is the cooling timescale. The cooling timescale is a control parameter to support the growth of the VSI by achieving thermal relaxation by damping the pressure towards local equilibrium pressure.

Table 4.1: Initial parameters for PLUTO.

$N_{\rm r} \times N_\theta \times N_\phi$	Δr $[AU]$	$\Delta\theta$ $[AU]$
$1024 \times 1024 \times 1$	0.5:50	0.001:3.1405
Initial parameters		
p	-0.5	
q	-1.0	
R_0	10.0	
H_0	0.07	
Σ_0 [g cm^{-2}]	60	

4.3 Photochemical rates of stellar photons

The photoelectric heating process caused by EUV and FUV photons has been analytically determined by Bakes & Tielens (1994). Here we would like to revise this energy balance that sets the temperature of the gas. These equations have been implemented in the thermo-chemical hydrodynamical simulations led by Nakatani et al. (2018a,b) and the initial stellar parameters used in our model are specified in Table 4.2. Here we use his photochemical table to estimate the gas temperature and electron abundance, as described in the next section.

Table 4.2: Initial values for the model.

Stellar parameters	
Stellar mass	$1M_{\odot}$
Stellar radius	$1R_{\odot}$
X-ray luminosities	$[10^{29}, 10^{30}, 10^{31}]$ erg s^{-1}
EUV photon number rate	$[10^{40}, 10^{41}, 10^{42}]$ photon s^{-1}
FUV luminosities	$[10^{30}, 10^{31}, 10^{32}]$ erg s^{-1}

4.3.1 EUV

The EUV is an ionizing radiation and is repsonsible for heating associated with photoionization ($\mathrm{HI} \rightarrow \mathrm{HII} + \mathrm{e}$). The photoelectric heating rate caused by EUV is given by

$$\Gamma_{\mathrm{EUV}} = \frac{1}{\rho} n_{\mathrm{HI}} \int_{\nu_1}^{\infty} \sigma_{\mathrm{EUV}} h(\nu - \nu_1) F_{\mathrm{EUV}} d\nu, \tag{4.6}$$

where ν is the EUV photon frequency, n_{HI} is the number density of HI, F_{EUV} is the EUV frequency-dependent flux in the field defined as

$$F_{\mathrm{EUV}}(r, \theta, t) = \frac{\Phi_{\nu}(R_*)}{4\pi r^2} e^{-\sigma_{\mathrm{EUV}} N_{\mathrm{H}}}, \tag{4.7}$$

where $\Phi_{\nu}(R_*)$ is the photon number luminosity of the EUV emitted from stellar surface, and σ_{EUV}, shown also in equation 4.6, is the absorption cross section of the EUV photon. We also use equation 4.7 to calculate the flux for FUV and X-ray. The absorption cross section of EUV is defined as

$$\sigma_{\mathrm{EUV}} = 6.3 \times 10^{-18} \left(\frac{h\nu}{h\nu_1} \right)^{-3}, \tag{4.8}$$

in cm^2. The $h\nu$ and $h\nu_1$ is the EUV energy range.

4.3.2 FUV

The grain size and composition become more significant regarding the photoelectric heating caused by FUV photons. For grain sizes of a few microns like PAHs, ∼2-9μm, FUV photons are absorbed, and the kinetic energy it provides is enough for the electrons to collide with each other within the PAH particle. A small fraction of energetic electrons can escape from the surface of the grain, ionizing and heating the gas around it. Then, the ionization degree in the gas is determined based on the balance between photoionization and radiative recombination reactions. PAHs' effect on absorbing the FUV photon and producing energy depends on the ionization rate and the PAHs charge (Tielens, 2005). This mentioned the

photoelectric heating caused by the FUV depends on the ratio of the PAH photoionization rate and PAH recombination rate with electrons

$$\gamma_{\rm FUV} = \frac{G_0 T^{1/2}}{n_e}, \tag{4.9}$$

where G_0 is the initial FUV flux (for convenience we use $\rm F_{FUV}$), T is the temperature of the dust in which we use $T_{\rm dust} = T_{\rm gas} = T$, and n_e is the electron density. If $\gamma_{\rm FUV}$ is small, the PAHs are mostly neutral, and the photoelectric heating is high. For high photodissociation regions, the charge factor significantly reduces the photoelectric heating rate by grains (Tielens, 2005). The photoelectric heating efficiency can be deduced from the PAHs size distribution and the effects of the charge. This photoelectric heating efficiency has been determined analytically as stated in Tielens (2005)

$$\epsilon = \frac{4.87 \times 10^{-2}}{1 + 4 \times 10^{-3} \gamma_{\rm FUV}} + \frac{3.65 \times 10^{-2} (T/10^4)^{0.7}}{1 + 2 \times 10^{-4} \gamma_{\rm FUV}} \tag{4.10}$$

The first term takes into account the ionization balance and the second term reflects a temperature dependence in which, for high temperatures, the electron recombination rate is higher resulting in a decrease of grain charge. Finally, we can come together with the photoelectric heating rate also determined analytically by Bakes & Tielens (1994)

$$\Gamma_{\rm FUV} = 10^{-24} \epsilon F_{\rm FUV} n_{\rm H}, \tag{4.11}$$

in erg $\rm cm^{-3} s^{-1}$ where the $F_{\rm FUV}$ is defined similarly as equation 4.7,

$$F_{\rm FUV}(r, \theta, t) = \frac{\Phi_\nu(R_*)}{4\pi r^2} e^{-\sigma_{\rm FUV} N_{\rm H}}, \tag{4.12}$$

In conclusion, the gas is heated efficiently when FUV photons is absorbed by small grains like PAHs.

4.3.3 Soft X-ray

The X-ray heating rate is substantially less than the photoelectric heating caused by FUV photons due to the low ionization cross section and relatively low photon flux (Tielens, 2005), especially in T Tauri stars. Here we ignore the contribution of heating caused by X-rays since they provide very little to the total cross-section of the medium (Wilms et al., 2000). Same way as Nakatani et al. (2018b), we use the total cross section from Gorti & Hollenbach (2004), which describes the X-ray cross section per hydrogen nuclei for a disk with solar

metallicity

$$\sigma_{\rm Xray} = 1.2 \times 10^{-22} \left(\frac{h\nu}{1{\rm keV}} \right)^{-2.594}, \tag{4.13}$$

in $\rm cm^2$. The heating rate caused by X-ray photons is given by

$$\zeta_{\rm Xray} = \int_{E_1}^{E_2} F_{\rm Xray}(E) e^{-\tau_{\rm Xray}} \sigma_{\rm Xray} n_{\rm H} dE, \tag{4.14}$$

where $E = h\nu$ is the X-ray energy, $F_{\rm Xray}(E)$ is the X-ray flux, $\tau_{\rm Xray}$ is the optical depth of the X-ray through the medium and its definition is represented as the integrated extinction coefficient along the radial direction

$$\tau(\nu_{\rm Xray}, r) = \int_{R_*}^{r} d\tau = \int_{R_*}^{r} \sigma_{\rm Xray} N_{\rm H} dr \tag{4.15}$$

where $\sigma_{\rm Xray}$ is the X-ray absorption cross section, and N_H is the column density. Equation 4.15 is also adopted for the other EUV and FUV flux rates as $\sigma_\nu N_H$. The absorption cross-section gives the pathway to photochemical reaction rates that determine the probability that the photon passing through a medium gets absorbed by any gas or dust agent. Secondary X-ray heating reaction is possible when reacting with cosmic rates, but here, we focus on the primary way, which is given in equation 4.14.

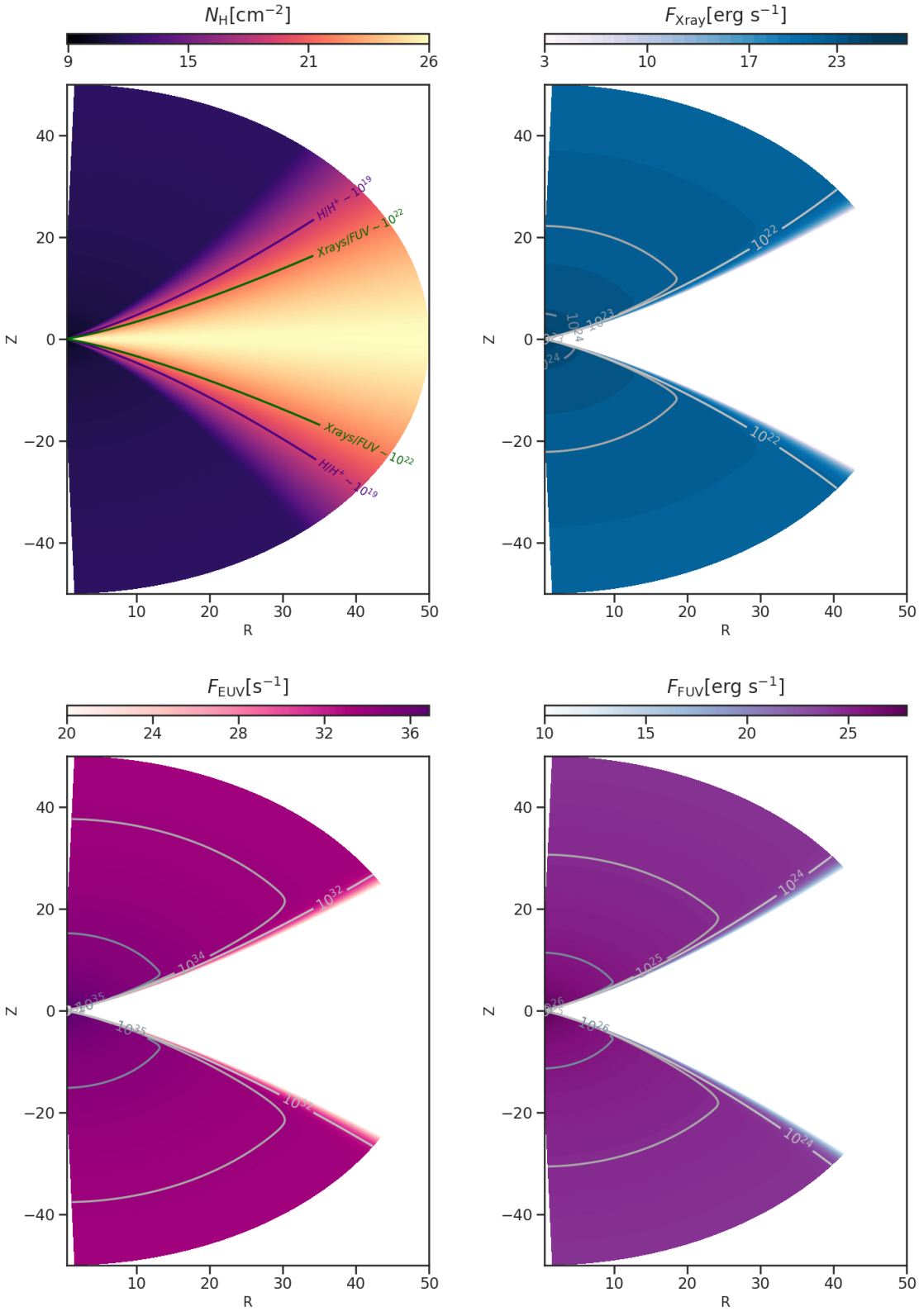

Figure 4.1: Initial configuration of the gas and stellar fluxes.

4.4 Photochemical table outlook

The goal is to analyze the growth of the VSI in combination with disk winds driven by photochemistry. In this work, we build our disk model based on the full radiation hydrodynamical model from Nakatani et al. (2018a,b). This model includes X-ray, EUV, and FUV heating rates and thermochemistry to determine the temperature and electron abundance accurately. The outcome of the photochemical table * is based on six physical parameters such as: the radius (r), the number density ($n_{\rm H}$), the column density ($N_{\rm H}$), X-ray flux ($F_{\rm Xray}$), EUV flux ($F_{\rm EUV}$), and FUV flux ($F_{\rm FUV}$). Then, the temperature, $T(\vec{X})$, $\vec{X} \in \mathbb{R}^6$, is a combination of six parameters prescribed as

$$T(\vec{X}) = \sum_{i=1}^{6} X_i = [X_1, \ldots, X_6]^T \tag{4.16}$$

In the same way, the electron abundance, $n_e(\vec{X})$, $\vec{X} \in \mathbb{R}^6$ function is

$$n_e(\vec{X}) = \sum_{i=1}^{6} X_i = [X_1, \ldots, X_6]^T \tag{4.17}$$

where $\vec{X}$ is the 6D vector function. Each one of the 6 parameters represent the position index in the table as

$$\sum_{i=1}^{6} X_i = \sum_{i=1}^{6} x_i = \frac{\log_{10} x_i^n - \log_{10} x_i^0}{\Delta_i}, \tag{4.18}$$

where n is the arbitrary parametric position, and

$$\sum_{i=1}^{6} x_i = [X_1, \ldots, X_6]^T = [r, n_{\rm H}, N_{\rm H}, F_{\rm Xray}, F_{\rm EUV}, F_{\rm FUV}]^T \tag{4.19}$$

Given that the photochemical table is a 6-dimensional vector function, there are $2^n = 2^6 = 64$ possible combinations for the given parameter set. Then, in order to perform a linear interpolation for n=64 dimensional points, the final temperature and electron abundance value are obtained

$$T_{\rm final}, n_{e,\rm final} = \sum_{i=1}^{6} x_i^{n-1} + (X_i - i)\left[x_i^{n+1} - x_i^{n-1}\right], \tag{4.20}$$

such that we have a element reduction from $64 \rightarrow 32 \rightarrow 16 \rightarrow 4$ until 2. The temperature and the electron density values (equation 4.16 and equation 4.17) were solved self-consistently

*The photochemical table is provided by Riouhei Nakatani.

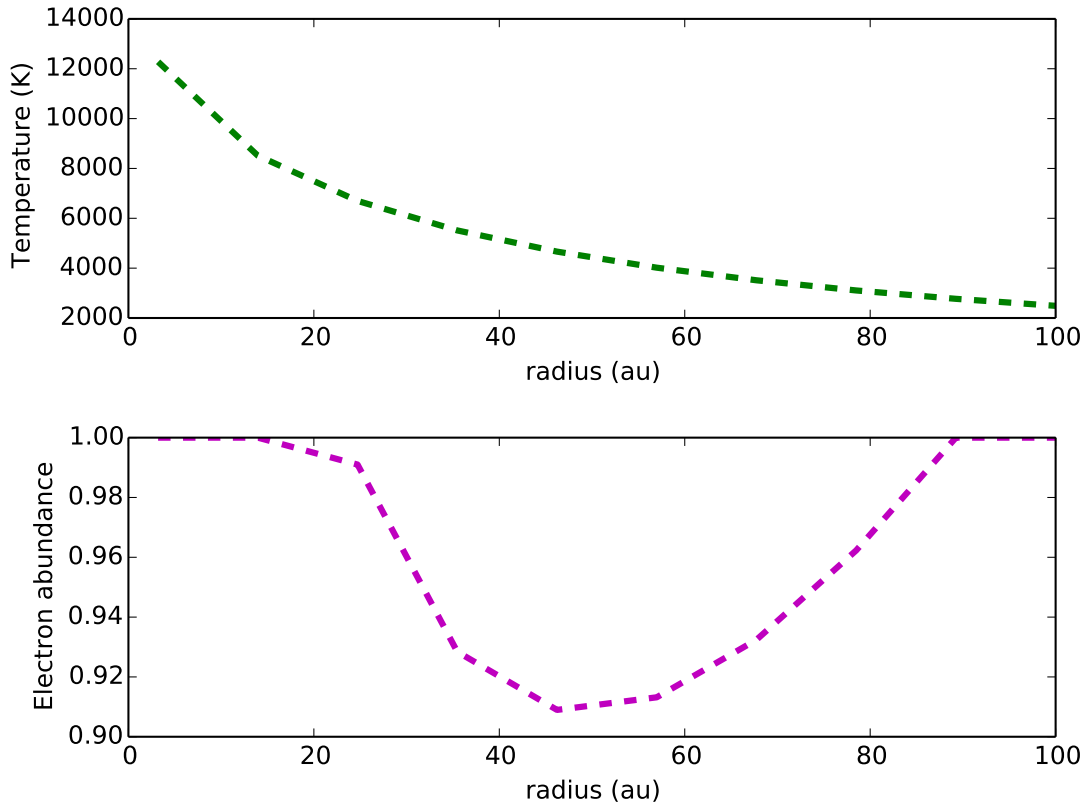

Figure 4.2: 1D plot of the temperature and electron abundance profile as a function of radius for a selected set of parameters: $\rho = 4 \times 10^{-8}$ cm^{-3}, $N_H = 7 \times 10^{14}$ cm^{-2}, EUV, FUV, and X-ray fluxes are taken from $F_{\nu,0}(\frac{R_0}{R})^2$.

with thermochemistry Nakatani et al. (2018a,b). This table contains local points from 27 simulations where each table row is a random local point in the 6D parameter space. Figure 4.3 shows the relation between the temperature and electron abundance combined with different parameters, respectively. The best correlation is the ones that show a clear linear dependence with the temperature. Variations in the spread of the correlations yield a large deviation in temperature and electron abundance because each photon flux calculation depends on the radius, column density, and source luminosities. The determination of the temperature and the electron abundance is a function of both disk radius and scale height for a given set of the six parameters mentioned in the previous section. For the dynamical evolution of the gas, the temperature and electron abundance is iterative at every cell for every time step.

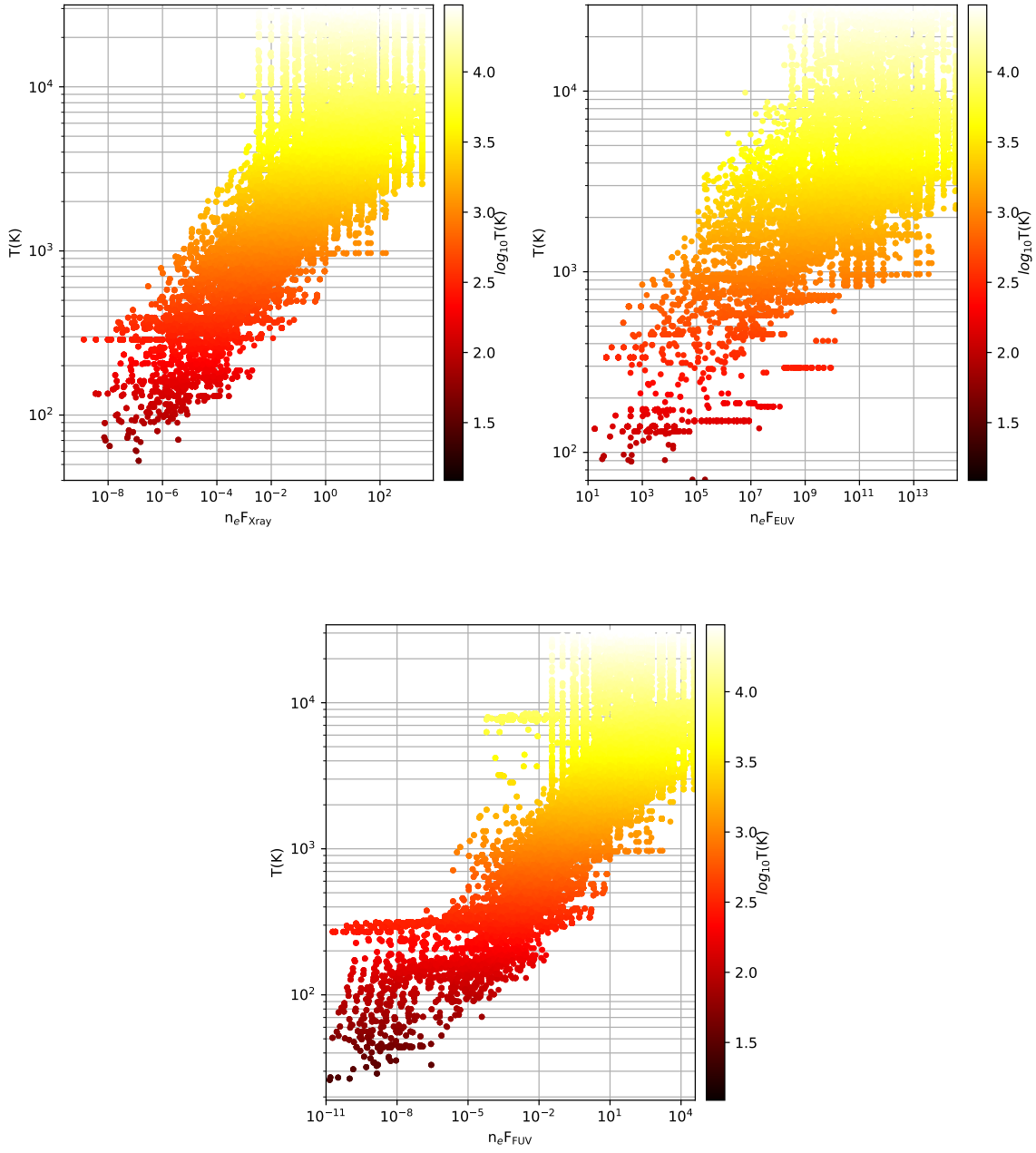

Figure 4.3: Temperature as a function of Xray, EUV, FUV, flux times electron abundance.

4.5 Line radiative transfer

One way to compare our hydro-thermochemical predictions of disk winds with existing spectral data is to produce a synthetic line profile of the gas tracer of interest. In this next part, we will use our simulation data and post-process it with RADMC-3D (Dullemond et al., 2012) to produce the spectra line emission and search for distinct features of disk winds. The main goal is achieved by reproducing the spectral line profile of the gas tracer, comparing its velocity and width, the spatial integrated intensity, and the intensity-weighted velocity distribution. In Figure 4.4 we consider the HCO^+ (J=4-3) as an example to reproduce its spectrum under typical conditions of the formation above the disk surface at a disk scale height of 0.3. The HCO^+ (J=4-3) is the product of ion-molecule reactions caused by the direct influence of X-ray and UVs luminosities. We select non-LTE line treatment for the line radiative transfer calculations under the assumption that all the emission from the gas tracer is never absorbed in optically thin regions. The number density of the collision partners: ortho-H_2 and para-H_2, were taken from Smirnov-Pinchukov et al. (2020). The ortho-H_2 and para-H_2 are required for non-LTE line transfer because the molecule, under highly ionized environments, can be easily excited through collisions between electrons where the nuclear spin-state is exchanged. We follow the gas properties in Table 4.3 for the generation of the HCO^+ (J=4-3) synthetic line profile.

The synthetic line profile of HCO^+ (J=4-3) in Figure 4.4 is done under a few and specific parameters that portray low density and hot regions in the disk atmosphere, which is suitable for promoting outflowing gas. However, when we include the gas, electron density, and temperature from our hydro-photochemical simulations, the spectral line profile for a molecule could be reproduced differently depending on the set of parameters selected for each location above the disk surface. The integrated spectral profile of the gas tracer of interest, as a function of gas density integrated over the disk, could probe distinct signatures described in actual spectral data and estimate how much mass is lost during the photoevaporation process important for the dispersal of the disk.

Table 4.3: Chemical abundances and input parameters for the RADMC-3D line radiative transfer calculations.

n(X)/n(H)	
ortho-H_2	3.75×10^{-1}
para-H_2	1.25×10^{-1}
HCO^+	2.1×10^{-9}
Physical properties.	
Dust-to-gas mass ratio	0.01
n_{gas}	6.0×10^{8} cm^{-3}
T_{gas}	5,000 K
distance	140 pc

Notes. n(X)/n(H) is the fractional abundance relative to H.

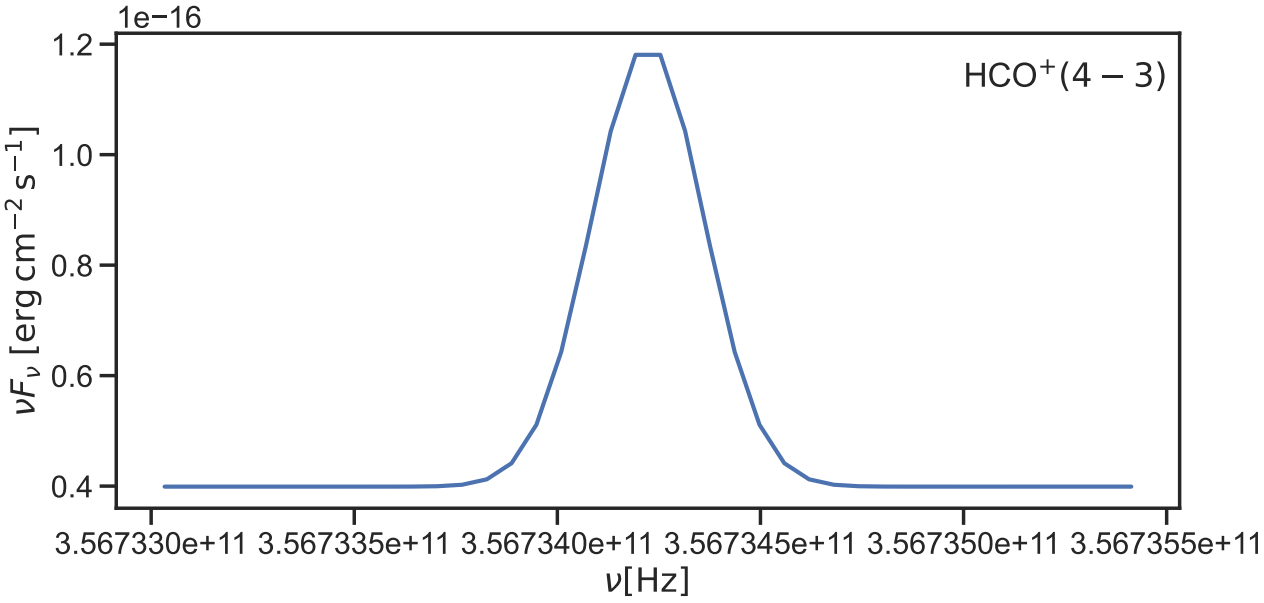

Figure 4.4: Hyperfine spectral line profile of the HCO^+ (J=4-3).

4.6 Photoevaporation rate

The mass loss or photoevaporation rate is one key parameter when describing photoevaporative driven winds. Though photoevaporative winds do not play a role in the angular momentum transport, velocity perturbations of the gas caused by the VSI can affect the transport of material out in the disk. The mass loss rate value between MHD and photoevaporative winds are, in general, comparable ($10^{-7} - 10^{-8}$ $M_\odot$ yr^{-1};Wang et al. (2019); Gressel et al. (2020)). The photoevaporation rate is calculated by integrating the mass flux that is perpendicular to the surface area, $r\Omega$, of the cell

$$\dot{M}_{\rm phot} = \int_\Omega r d\vec{\Omega} \cdot \rho\vec{v} = r^2 \int_\theta \int_\phi \sin\theta d\phi d\theta \rho v_r \tag{4.21}$$

where r is the radius of the surface area, and v_r is the radial velocity. As this is a work in progress, we expect that the resulting values from equation 4.21 would be similar to those estimated by (Nakatani et al., 2018a), which consider an adequate 2D radiative transfer for the photochemical calculations. However, differences in the estimated photoevaporation rate are expected as each stellar photon dominates differently depending on the geometrical structure of the disk. The thermochemical and irradiation effects for solar-like T Tauri stars with a typical magnetic field of ∼500 mGauss, are crucial at the disk surface and even more than the detailed levels of magnetic dissipation at the midplane (Gressel et al., 2020).

5 Conclusions and future work

"The measure of greatness in a scientific idea is the extent to which it stimulates thought and opens up new lines of research"

by Paul Dirac

This thesis covers research from global hydrodynamical simulations of the gas dynamics in protoplanetary disks to the observational analysis of the outflowing gas and jets, constituents of the Class II star-forming stage. In chapter one, we focused on the gas dynamics in protoplanetary disks at a global scale. Due to the vertical differential rotation ($\frac{\partial \Omega}{\partial Z} > 0$) and the relative short cooling timescale ($\tau_{\text{cooling}} < 10^{-2}$ orbits) compared to the dynamical timescale, gas disturbances are generated. This gas perturbation in the disk is mainly attributed to the VSI. The growth rate in the linear phase of the VSI has been determined to be around 0.25 orbits^{-1}. However, when the linear modes reach a saturation level in the kinetic energy, they are subject to the second generation of non-linear modes, so-called body modes. These body modes dominate in the non-linear phase in the vertical column of the disk, and they generate faster when the resolution in the simulations is increased (Flores-Rivera et al., 2020). At the surface layer of the disk, the body modes provide persistent kinetic energy flares powered by subsonic upward flows in low-density regions ($n_\rho < 10^6$ cm^{-3}). This is important for us to consider when analyzing the effects of the wind launch mechanism. It is in the non-linear phase that the VSI is most turbulent. As the VSI is strongly anisotropic, meaning that the magnitude of the vertical velocity is much greater than the magnitude of the radial velocity, this results in a vertical stress-to-pressure ratio of 10^{-2} (Stoll et al., 2017a). Nevertheless, when it comes to angular momentum transport, the stress-to-pressure ratio, α, is found to be between 10^{-3} and 10^{-4} (Manger & Klahr, 2018; Stoll et al., 2017b; Barraza-Alfaro et al., 2021), which is about two orders of magnitude lower than in the vertical direction. In the planet formation scenario context, we found that the VSI activity is also present locally in the midplane, reproducing the same growth rate trend as in the global case.

Nevertheless, other hydrodynamical instabilities can be present at the same time. The VSI can be susceptible to large-scale vortices along the vertical direction (Stoll et al., 2017b; Manger & Klahr, 2018) and to small-scale vortices along the azimuthal direction (Flores-

Rivera et al., 2020). Due to the velocity shear across the fluid interface, these have been recognized as the Kelvin-Helmholtz instability (Nelson, R. P. and Gressel, O. and Umurhan, O. M., 2013; Latter & Papaloizou, 2018). Nevertheless, radial variations in the rate of angular momentum caused by the VSI can also form vorticity rings attributed to the Rossby wave instability (Lovelace et al., 1999; Richard, Samuel and Nelson Richard P., and Umurhan Orkan M., 2016; Li et al., 2000, 2001) and be amplified by the Sub-critical Baroclinic Instability (Klahr & Bodenheimer, 2003). The implications of these instabilities on the planet formation process must consider the dust back-reaction with the gas.

How would the VSI perturb the surface of the disk where the gas is highly ionized? From the observational point of view, Class I and Class II disks have been observed to have outflows in the form of jets and winds. Outflow cavities with outward velocities of just a few km s^{-1} from the central star (Flores-Rivera et al., 2021) produce strong molecular emissions. One explanation for how these molecules do not dissociate in such high thermal environments is that outflows seem to be fueled by MHD or perhaps by photoevaporative winds. The fundamental idea of these environments is that the gas supports electrical currents. This is achieved by excellent charge carriers such as free-free electrons, atomic or molecular ions, or small grain particles like PAHs. At atomic levels, high spectral resolutions have identified forbidden emission lines emitted in highly ionized regions, where the dust-to-gas mass ratio is potentially below 0.01.

The Multi-unit Spectroscopic Explorer (MUSE) instrument installed at the Very Large Telescope (VLT) has a great capability to provide a high spatial resolution of 25 mas with a spectral range from 4650-9300 Angstrom and resolving power of ∼2000 at 4600 Angstrom and ∼4000 at 9300 Angstrom. Thanks to the Integral Field Units (IFU) technology, seven forbidden emission lines were identified in protoplanetary disks. The excellent image quality of the instrument confirms that these emission lines have an origin in the inner parts of the protoplanetary disk as outflows and jets. From the maximum intensity emission along these outflows/jets analyzed in DL Tau, CI Tau, DS Tau, IP Tau, and IM Lup, the position angle of the outflow/jet, $PA_{outflow/jet}$, was reliably measured on most of the identified emission lines. The $PA_{outflow/jet}$ is assumed to be linked with the inner disk when compared with the PA_{dust} from the outer disk that is constrained by previous work. Our estimates of outflows/jets systems analyzed here are aligned within 1° between the inner and outer disk. Further observations must confirm a potential misalignment in IM Lup as this source shows the lowest signal-to-noise ratio. As mentioned, these estimates depend not only on the signal-to-noise but also on the collimation of the outflow/jet. The outflows/jets in CIDA 9, GO Tau, and GW Lup was too compact for a $PA_{outflow/jet}$ to be estimated. Based on kinematics analysis, we confirm that DL Tau and CI Tau host a strong outflow/jet with line-of-sight velocities much greater than 100 km s^{-1}. In contrast, DS Tau, IP Tau, and IM Lup velocities are lower, and their structures encompass low-velocity components to be more associated with winds. Our estimates for the mass loss rate, $\dot{M}_{loss}$, range between (2-9) $\times 10^{-7}$-10^{-8} $M_{\odot}\ yr^{-1}$ for the disk-outflow/jet systems analyzed here.

5.1 What did we learn after all?

Protoplanetary disks are synergistic and complex sources that result in the fascinating birth of planets. Observational imaging and spectral observations of disks with structures demon-

strate that it is not easy to simultaneously bridge the formation of multiple planetesimal bodies. When we talk about *formation of planets* we stress that this is a multi-faceted process that encompasses a great understanding of not only how the dust coagulates to form the rocky planet core but also what is the local chemical composition. At the same time, other parts of the disks are also forming planetesimals. The disk is a non-stopping dynamical engine, so the physics and the chemistry, together with dust and gas turbulence, act together to shape the disk we see. There are still so many unknowns that our commitment contributed just a puzzle to the big picture of planet formation and evolution of the disk. A brief summary of the theory and observational data we tried to contribute in order to understand and connect how different components of the disk work together are as follow:

- The VSI appears to control the gas dynamics in protoplanetary disks. The generation of the turbulent modes develops quickly and brings the material to the wind base, supplying a positive impact for the generation of disk winds.
- Observations based on the velocity components of the forbidden emission lines in disks suggest that outflows and jets can be greatly supported by MHD and photoevaporative winds generated from highly ionized gas in the inner disk. From shock diagnostic from the brightest lines reported suggest that these environments hold electron densities of $10^3 - 10^4$ cm^{-3}, ionization fraction of 0.2-15, Hydrogen pre-shock number density of $10^2 - 10^4$ cm^{-3}, and magnetic field strength of 10-10,000 μG. The relative occurrence between MHD winds and photoevaporative is still an unresolved matter.

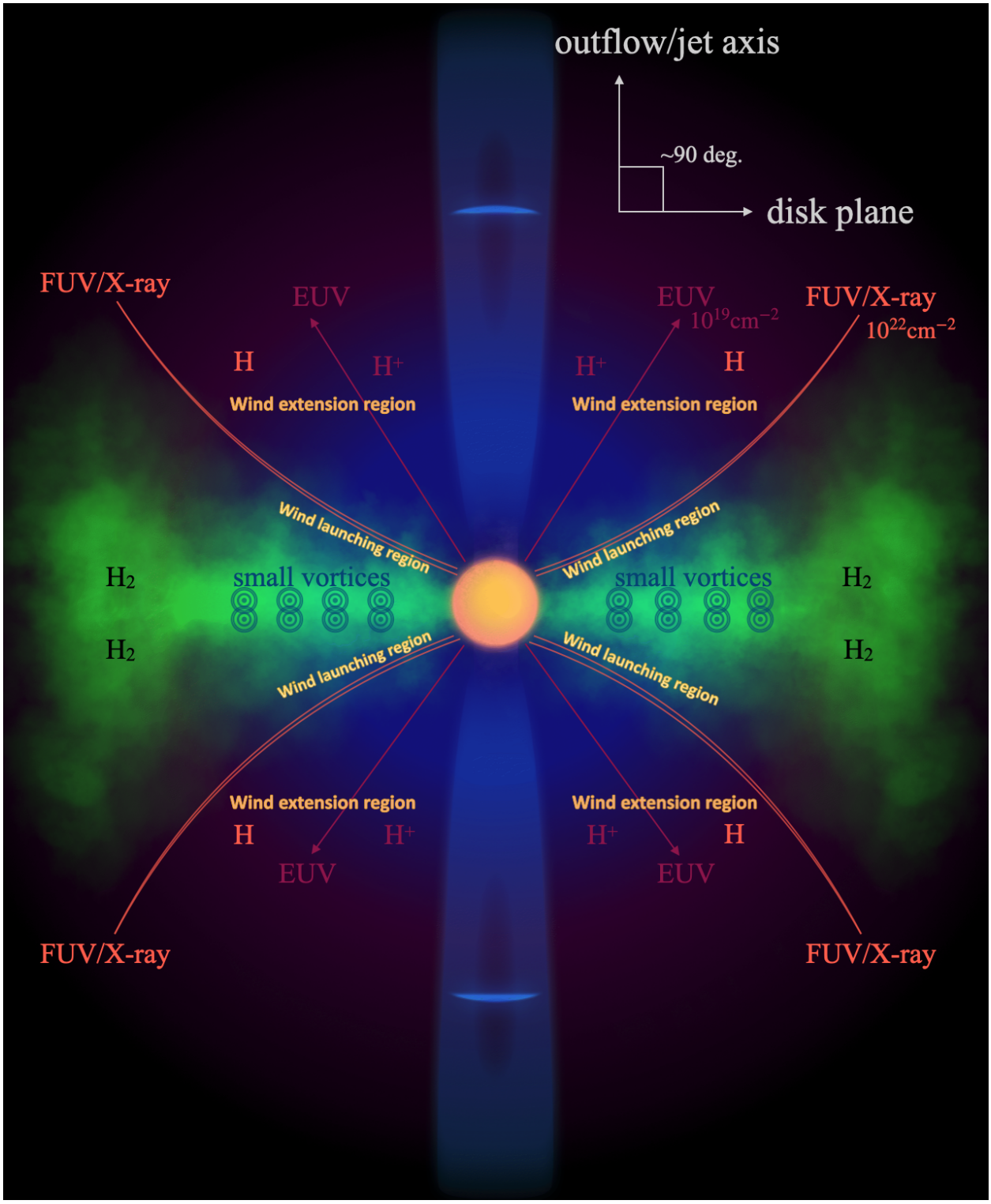

Figure 5.1: Summary of the work presented in this thesis. This artistic representation is the same as in Figure 1.8 from Chapter 1. The idea of bringing this back is to highlight the most relevant components of the interplay of gas dynamics and the different mechanisms contributing to disk dispersal.

5.2 Future work

"In general, scientific progress calls for no more than the absorption and elaboration of new ideas – and this is a call most scientists are happy to heed"

by Werner Heisenberg

5.2.1 Dust module implementation

In terms of dust concentration, it has been suggested that the VSI can stir up dust particles that can be seen as small, turbulent eddies of the vertical motion (Flock et al., 2017; Lin, 2019; Flores-Rivera et al., 2020). Recent work (Lin, 2019) has demonstrated that the VSI is sensitive to 1) the dust settling, 2) a small temperature gradient ($q < 1$), 3) for large particle size (Stokes number=0.01 corresponding to $\sim$ 3mm-90μm) promoting grain growth. In the context of planet formation, the VSI and the Streaming Instability (SI) can interact to promote a high concentration of gas and dust density favorable for planetesimal formation under conditions that can be constrained from observations (Schäfer et al., 2020b; Schäfer & Johansen, 2022). Higher in scale height, the VSI can maintain small particles ($< 100\mu$m) afloat until they become ionized by FUV photons, contributing to heating in the disk atmosphere (Lin, 2019) and potentially causing the generation of winds at the surface of the disk. A detailed thermo-chemistry in the protoplanetary disk, including a full prescription of EUV, FUV, and X-rays photons and dust, must be considered in the future.

For the implementation of dust particles in our setup, we will follow (Mignone et al., 2019; Flock & Mignone, 2021) numerical dust grain module to study the interaction between gas and dust in our global simulation with VSI. The dust particle size will be fixed and given a speck of initial dust to gas mass ratio defined through the ratio of vertically integrated surface density. We will follow self-consistently the evolution of the gas and dust velocities prescribed by (Nakagawa et al., 1986). The parameters to study would correspond to the spaced-averaged dust-to-gas mass ratio at $Z = 0$ (midplane) for particles with a Stokes number of St=0.1 ($\sim$1 mm), and at $Z = 6H_{\rm R}$ (wind base) for particles with St=0.001 ($\sim 1\mu$m).

5.2.2 Switch on magnetic field

Another plan we need to work on is to include the magnetic field process in our hydrodynamical configuration. Without hydrodynamical instabilities, the angular momentum transport is carried by MHD processes. In the innermost part (1-10 AU), the disk is thermally ionized, and the launch of magneto centrifugal outflows is primarily taking place through magnetic tension forces. The plasma parameter, β, which is the ratio of the thermal over the magnetic pressure and the dust-to-gas mass ratio of the ionized model, will help us understand and see the transport of the gas and dust efficiently via winds. The photochemical effects, including EUV, FUV, and X-ray, are very important for the mass loss rate that could potentially have a strong effect and efficiency in the launch of winds (Gressel et al., 2020; Wang et al., 2019). On the other hand, non-ideal MHD diffusivities, such as the ambipolar diffusion and the

Ohmic diffusion, that are more dominant in the outer disk (30-100 AU), could be present in the inner disk as well. As long as the gas is weakly coupled with the magnetic field, then the mass loss is primarily occurring in the thin surface layer of the disk.

List of publications

These scientific publications have been submitted and published during the PhD course, or are in preparation for publication within this year.

1st AUTHOR PUBLICATIONS

1. **Flores-Rivera, L.**, Flock, M., and Nakatani, R., 2020, Astronomy & Astrophysics Journals, 644; A50;
   "Hydrodynamical simulations of protoplanetary disks including irradiation of stellar photons. I. Resolution study for vertical shear instability"

2. **Flores-Rivera, L.**, Terebey, S., Willacy, K., Isella, A., Turner, N., Flock, M., 2021, ApJ, 908; 108;
   "Physical and Chemical Structure of the Disk and Envelope of the Class0/I Protostar L1527 "

3. **Flores-Rivera, L.**, Flock, M., et al. 2022, Astronomy & Astrophysics Journals, *in revision*,
   "Forbidden emission lines of protostellar outflows and jets with MUSE/VLT"

4. **Flores-Rivera, L.**, Flock, M., Nakatani, R., et al. 2022, Astronomy & Astrophysics Journals, *inPrep.*,
   "Hydrodynamical simulations of protoplanetary disks including irradiation of stellar photons. II. Photoevaporative-driven winds"

CONTRIBUTIONS TO PUBLICATIONS INCLUDED IN THIS THESIS

1. Birney, M., Whelan, E., ..., **Flores-Rivera, L.** et al. 2022, to be submitted;
   "Spectro-imaging of the RU Lupi Wind and Jet"

CONTRIBUTIONS TO PUBLICATIONS NOT INCLUDED IN THIS THESIS

1. Dietrich, J., ..., **Flores-Rivera, Lizxandra**, et al. 2022, ApJ, *subm.*,
   "EDEN Survey: Small Transiting Planet Detection Limits and Constraints on the Occurrence Rates for Late M Dwarfs within 15 pc"

2. Tregloan, J., ..., **Flores-Rivera, Lizxandra**, et al. 2022, Astronomy & Astrophysics Journal, *inPrep.*,
   "Colour dependent optical phase curves of Starlink LEO satellites"

Bibliography

Aikawa, Y., Cataldi, G., Yamato, Y., et al. 2021, ApJS, 257, 13 15

Alcalá, J. M., Manara, C. F., Natta, A., et al. 2017, A&A, 600, A20 91

Alexander, R., Pascucci, I., Andrews, S., Armitage, P., & Cieza, L. 2014, in Protostars and Planets VI, ed. H. Beuther, R. S. Klessen, C. P. Dullemond, & T. Henning, 475 31

Alexander, R. D., Clarke, C. J., & Pringle, J. E. 2006a, MNRAS, 369, 216 31

—. 2006b, MNRAS, 369, 229 31

ALMA Partnership, Brogan, C. L., Pérez, L. M., et al. 2015, ApJ, 808, L3 14

Andrews, S. M., Huang, J., Pérez, L. M., et al. 2018, ApJ, 869, L41 14, 55

Antoniucci, S., García López, R., Nisini, B., et al. 2011, A&A, 534, A32 52

Arlt, R., & Urpin, V. 2004, Astronomy & Astrophysics, 426, 755 24, 31

Armitage, P. J. 2007, arXiv e-prints, astro 20

—. 2011, ARA&A, 49, 195 22, 27

—. 2015, arXiv e-prints, arXiv:1509.06382 26, 27

Avenhaus, H., Quanz, S. P., Garufi, A., et al. 2018, ApJ, 863, 44 66

Bacciotti, F., Mundt, R., Ray, T. P., et al. 2000, ApJ, 537, L49 52

Bacon, R., Accardo, M., Adjali, L., et al. 2010, in Society of Photo-Optical Instrumentation Engineers (SPIE) Conference Series, Vol. 7735, Ground-based and Airborne Instrumentation for Astronomy III, ed. I. S. McLean, S. K. Ramsay, & H. Takami, 773508 52

Bai, X.-N. 2017, ApJ, 845, 75 97

Bai, X.-N., & Stone, J. M. 2013, ApJ, 769, 76 51

Bakes, E. L. O., & Tielens, A. G. G. M. 1994, ApJ, 427, 822 99, 101

Balbus, S. A., & Hawley, J. F. 1991, ApJ, 376, 214 20, 51

Ballabio, G., Alexander, R. D., & Clarke, C. J. 2020, MNRAS, 496, 2932 32

Banzatti, A., Pascucci, I., Edwards, S., et al. 2019, ApJ, 870, 76 3, 5, 6, 23, 32, 51, 52, 55, 68, 69, 72, 73, 91, 93, 94, 98

Banzatti, A., & Pontoppidan, K. M. 2015, ApJ, 809, 167 98

Barge, P., & Sommeria, J. 1995, A&A, 295, L1 26

Barker, A.J. and Latter, H.N. 2015, MNRAS, 450, 21 24, 31

Barranco, J. A., & Marcus, P. S. 2005, ApJ, 623, 1157 26

Barranco, J. A., Pei, S., & Marcus, P. S. 2018, ApJ, 869, 127 26

Barraza-Alfaro, M., Flock, M., Marino, S., & Pérez, S. 2021, A&A, 653, A113 21, 111

Benisty, M., Juhasz, A., Boccaletti, A., et al. 2015, A&A, 578, L6 28

Benisty, M., Stolker, T., Pohl, A., et al. 2017, A&A, 597, A42 52

Benisty, M., Juhász, A., Facchini, S., et al. 2018, A&A, 619, A171 52

Benisty, M., Bae, J., Facchini, S., et al. 2021, ApJ, 916, L2 16

Benisty, M., Dominik, C., Follette, K., et al. 2022, arXiv e-prints, arXiv:2203.09991 10, 12

Bergez-Casalou, C., Bitsch, B., Pierens, A., Crida, A., & Raymond, S. N. 2020, A&A, 643, A133 27

Béthune, W., Lesur, G., & Ferreira, J. 2017, A&A, 600, A75 97

Blanco, D., Ricci, L., Flock, M., & Turner, N. 2021, ApJ, 920, 70 21

Blandford, R. D., & Payne, D. G. 1982, MNRAS, 199, 883 51

Bohn, A. J., Benisty, M., Perraut, K., et al. 2021, arXiv e-prints, arXiv:2112.00123 52, 54, 69

Brown, P. J., Fuller, W. A., et al. 1990, Statistical analysis of measurement error models and applications: Proceedings of the AMS-IMS-SIAM joint summer research conference held June 10-16, 1989, with support from the National Science Foundation and the US Army Research Office, Vol. 112 (American Mathematical Soc.) 61

Cabral, B., & Leedom, L. C. 1993, in Proceedings of the 20th Annual Conference on Computer Graphics and Interactive Techniques, SIGGRAPH â€93 (New York, NY, USA: Association for Computing Machinery), 263â€270 41

Cameron, A. G. W. 1978, Moon and Planets, 18, 5 27

Carrasco-González, C., Henning, T., Chandler, C. J., et al. 2016, ApJ, 821, L16 14

Casassus, S., Avenhaus, H., Pérez, S., et al. 2018, MNRAS, 477, 5104 52

Casassus, S., Marino, S., Lyra, W., et al. 2019, MNRAS, 483, 3278 28

Casse, F., & Ferreira, J. 2000, A&A, 353, 1115 51

Casse, F., & Keppens, R. 2002, ApJ, 581, 988 51

Chambers, J. E. 2014, Icarus, 233, 83 27

Clarke, C. J., Gendrin, A., & Sotomayor, M. 2001, MNRAS, 328, 485 31

Cody, A. M., & Hillenbrand, L. A. 2018, The Astronomical Journal, 156, 71 82

Colella, P., & Woodward, P. R. 1984, Journal of Computational Physics, 54, 174 38

Cui, C., & Bai, X.-N. 2020, The Astrophysical Journal, 891, 30 37, 47

Debes, J. H., Poteet, C. A., Jang-Condell, H., et al. 2017, ApJ, 835, 205 52

Dong, R., Liu, S.-y., Eisner, J., et al. 2018, ApJ, 860, 124 28

Dougados, C., Cabrit, S., Lavalley, C., & Ménard, F. 2000, A&A, 357, L61 52

Drabek-Maunder, E., Mohanty, S., Greaves, J., et al. 2016, ApJ, 833, 260 98

Dullemond, C. P., Juhasz, A., Pohl, A., et al. 2012, RADMC-3D: A multi-purpose radiative transfer tool, Astrophysics Source Code Library, record ascl:1202.015, ascl:1202.015 107

Dullemond, C. P., Birnstiel, T., Huang, J., et al. 2018, ApJ, 869, L46 20, 21

Dzyurkevich, N., Turner, N. J., Henning, T., & Kley, W. 2013, ApJ, 765, 114 31

Edwards, S., Cabrit, S., Strom, S. E., et al. 1987, ApJ, 321, 473 52, 67

Ellerbroek, L. E., Podio, L., Dougados, C., et al. 2014, A&A, 563, A87 81, 84

Emsellem, E., Schinnerer, E., Santoro, F., et al. 2021, arXiv e-prints, arXiv:2110.03708 53

Ercolano, B., Drake, J. J., Raymond, J. C., & Clarke, C. C. 2008, ApJ, 688, 398 31

Ercolano, B., & Owen, J. E. 2016, MNRAS, 460, 3472 91

Ercolano, B., & Pascucci, I. 2017, Royal Society Open Science, 4, 170114 31, 51

Eriksson, S. C., Asensio Torres, R., Janson, M., et al. 2020, A&A, 638, L6 74

Fang, M., Pascucci, I., Edwards, S., et al. 2018, ApJ, 868, 28 32, 51, 52, 55, 68, 69, 80, 81, 91, 93

Fendt, C., & Zinnecker, H. 1998, A&A, 334, 750 64

Ferreira, J. 1997, A&A, 319, 340 97

Ferreira, J., Dougados, C., & Cabrit, S. 2006, A&A, 453, 785 22

Ferreira, J., & Pelletier, G. 1995, A&A, 295, 807 97

Flock, M., & Mignone, A. 2021, A&A, 650, A119 26, 115

Flock, M., Nelson, R. P., Turner, N. J., et al. 2017, The Astrophysical Journal, 850, 131 22, 115

Flock, M., Turner, N. J., Mulders, G. D., et al. 2019, A&A, 630, A147 32

Flock, M., Turner, N. J., Nelson, R. P., et al. 2020, arXiv e-prints, arXiv:2005.11974 26, 42

Flores-Rivera, L., Flock, M., & Nakatani, R. 2020, Astronomy & Astrophysics Journal, 644, A50 24, 98, 111, 115

Flores-Rivera, L., Terebey, S., Willacy, K., et al. 2021, ApJ, 908, 108 9, 112

Fricke, K. 1968, ZAp, 68, 317 24, 31

Gaia Collaboration, Brown, A. G. A., Vallenari, A., et al. 2020, arXiv e-prints, arXiv:2012.01533 55, 61

Gammie, C. F. 2001, ApJ, 553, 174 27

Garufi, A., Benisty, M., Stolker, T., et al. 2017, The Messenger, 169, 32 10

Giannini, T., Antoniucci, S., Nisini, B., Bacciotti, F., & Podio, L. 2015, The Astrophysical Journal, 814, 52 80

Goldreich, P., & Lynden-Bell, D. 1965, MNRAS, 130, 125 26

Goldreich, P. and Schubert, G. 1967, ApJ, 150, 571 23, 24, 31

Gorti, U., Dullemond, C. P., & Hollenbach, D. 2009, ApJ, 705, 1237 31

Gorti, U., & Hollenbach, D. 2004, ApJ, 613, 424 101

Gorti, U., & Hollenbach, D. 2008, The Astrophysical Journal, 683, 287 35

Gressel, O., Ramsey, J. P., Brinch, C., et al. 2020, arXiv e-prints, arXiv:2005.03431 32, 47, 97, 108, 115

Gullbring, E., Hartmann, L., Briceño, C., & Calvet, N. 1998, ApJ, 492, 323 91

Haffert, S. Y., Bohn, A. J., de Boer, J., et al. 2019, Nature Astronomy, 3, 749 5, 16, 52, 66

Hamann, F. 1994, ApJS, 93, 485 51, 52

Hartigan, P., Edwards, S., & Ghandour, L. 1995, ApJ, 452, 736 51, 52, 67, 80

Hartigan, P., Morse, J. A., & Raymond, J. 1994, ApJ, 436, 125 80, 81, 84, 88

Hashimoto, J., Aoyama, Y., Konishi, M., et al. 2020, AJ, 159, 222 52

Hawley, J. F., Gammie, C. F., & Balbus, S. A. 1995, ApJ, 440, 742 97

Haworth, T. J., & Owen, J. E. 2020, MNRAS, 492, 5030 98

Hirth, G. A., Mundt, R., & Solf, J. 1997, A&AS, 126, 437 52

Hogerheijde, M. R. 2011 (Springer Berlin Heidelberg), 1357–1366 9

Hollenbach, D., Johnstone, D., Lizano, S., & Shu, F. 1994, ApJ, 428, 654 22, 31, 97

Huang, J., Andrews, S. M., Dullemond, C. P., et al. 2018a, ApJ, 869, L42 3, 23

—. 2018b, ApJ, 869, L42 53, 55, 61

Hunter, J. D. 2007, Computing in Science & Engineering, 9, 90 130

Isella, A., Benisty, M., Teague, R., et al. 2019, ApJ, 879, L25 5, 16, 66

Izquierdo, A. F., Testi, L., Facchini, S., Rosotti, G. P., & van Dishoeck, E. F. 2021, A&A, 650, A179 17

Johansen, A., & Klahr, H. 2005, ApJ, 634, 1353 21

Kamann, S., Wisotzki, L., & Roth, M. M. 2013, A&A, 549, A71 53

Kamann, S., Husser, T. O., Dreizler, S., et al. 2018, MNRAS, 473, 5591 53

Keppler, M., Benisty, M., Müller, A., et al. 2018, A&A, 617, A44 16

Keppler, M., Teague, R., Bae, J., et al. 2019, A&A, 625, A118 5, 66

Klaassen, P. D., Juhasz, A., Mathews, G. S., et al. 2013, A&A, 555, A73 98

Klahr, H. 2007, in Convection in Astrophysics, ed. F. Kupka, I. Roxburgh, & K. L. Chan, Vol. 239, 405–416 26

Klahr, H., & Hubbard, A. 2014, ApJ, 788, 21 26

Klahr, H., Pfeil, T., & Schreiber, A. 2018, Instabilities and Flow Structures in Protoplanetary Disks: Setting the Stage for Planetesimal Formation, 138 32

Klahr, H. H., & Bodenheimer, P. 2003, ApJ, 582, 869 112

Kuiper, G. P. 1951, 1â€14 27

Lambrechts, M., & Johansen, A. 2012, A&A, 544, A32 27

Latter, H., & Papaloizou, J. 2018, MNRAS, 474, 3110 42, 112

Lavalley-Fouquet, C., Cabrit, S., & Dougados, C. 2000, A&A, 356, L41 52, 81, 95

Lesur, G., Kunz, M. W., & Fromang, S. 2014, Astronomy & Astrophysics Journal, 566, A56 21

Lesur, G., & Papaloizou, J. C. B. 2009, A&A, 498, 1 26

—. 2010, A&A, 513, A60 26

Lesur, G., Ercolano, B., Flock, M., et al. 2022, arXiv e-prints, arXiv:2203.09821 20

Li, H., Colgate, S. A., Wendroff, B., & Liska, R. 2001, ApJ, 551, 874 112

Li, H., Finn, J. M., Lovelace, R. V. E., & Colgate, S. A. 2000, ApJ, 533, 1023 112

Lin, M.-K. 2019, MNRAS, 485, 5221 31, 47, 115

Lin, M.-K., & Youdin, A. N. 2015, The Astrophysical Journal, 811, 17 24, 31

Lithwick, Y. 2009, The Astrophysical Journal, 693, 85 26

Long, F., Pinilla, P., Herczeg, G. J., et al. 2018, ApJ, 869, 17 4, 5, 53, 55, 56, 66, 69

Long, F., Herczeg, G. J., Harsono, D., et al. 2019, The Astrophysical Journal, 882, 49 4, 55, 56, 61, 93

Lovelace, R. V. E., Li, H., Colgate, S. A., & Nelson, A. F. 1999, ApJ, 513, 805 112

Lyra, W., & Umurhan, O. M. 2019, PASP, 131, 072001 32

Manger, N., & Klahr, H. 2018, MNRAS, 480, 2125 42, 111

Manger, N., Klahr, H., Kley, W., & Flock, M. 2020, MNRAS, 499, 1841 21

Marcus, P. S., Pei, S., Jiang, C.-H., et al. 2015, ApJ, 808, 87 26

Marino, S., Perez, S., & Casassus, S. 2015, ApJ, 798, L44 52

Marleau, G. D., Aoyama, Y., Kuiper, R., et al. 2021, arXiv e-prints, arXiv:2111.12099 52

Mattia, G., & Fendt, C. 2020, ApJ, 900, 59 51

Mignone, A. 2007, ApJ, 170, 228 32, 98, 130

—. 2014, Comput. Phys., 270, 784 33

Mignone, A., Flock, M., & Vaidya, B. 2019, ApJS, 244, 38 115

Moll, R., Spruit, H. C., & Obergaulinger, M. 2008, A&A, 492, 621 83

Monceau-Baroux, R., Porth, O., Meliani, Z., & Keppens, R. 2014, A&A, 561, A30 82

Muro-Arena, G. A., Benisty, M., Ginski, C., et al. 2020, A&A, 635, A121 52

Murphy, E. J., Bolatto, A., Chatterjee, S., et al. 2018, in Astronomical Society of the Pacific Conference Series, Vol. 517, Science with a Next Generation Very Large Array, ed. E. Murphy, 3 21

Nakagawa, Y., Sekiya, M., & Hayashi, C. 1986, Icarus, 67, 375 115

Nakatani, R., Hosokawa, T., Yoshida, N., Nomura, H., & Kuiper, R. 2018a, The Astrophysical Journal, 857, 57 22, 35, 47, 98, 99, 104, 105, 108

—. 2018b, The Astrophysical Journal, 865, 75 22, 35, 47, 98, 99, 101, 104, 105

Natta, A., Testi, L., Alcalá, J. M., et al. 2014, A&A, 569, A5 52, 55, 81, 88, 98

Natta, A., Testi, L., Muzerolle, J., et al. 2004, A&A, 424, 603 88

Nelson, R. P. and Gressel, O. and Umurhan, O. M. 2013, A&A, 435, 2610 19, 21, 23, 24, 31, 33, 37, 41, 112

Nisini, B., Antoniucci, S., Alcalá, J. M., et al. 2018, A&A, 609, A87 51, 52, 80, 91, 98

Öberg, K. I., Guzmán, V. V., Walsh, C., et al. 2021, ApJS, 257, 1 14

Ormel, C. W., & Klahr, H. H. 2010, A&A, 520, A43 27

Ormel, C. W., Shi, J.-M., & Kuiper, R. 2015, MNRAS, 447, 3512 32

Owen, J. E., Clarke, C. J., & Ercolano, B. 2012, MNRAS, 422, 1880 31

Owen, J. E., Ercolano, B., & Clarke, C. J. 2011, MNRAS, 412, 13 31

Owen, J. E., Ercolano, B., Clarke, C. J., & Alexand er, R. D. 2010, MNRAS, 401, 1415 31

Pan, L., & Yu, C. 2020, ApJ, 898, 7 26

Pascucci, I., Cabrit, S., Edwards, S., et al. 2022, arXiv e-prints, arXiv:2203.10068 17, 22

Pascucci, I., Sterzik, M., Alexander, R. D., et al. 2011, ApJ, 736, 13 32, 98

Pascucci, I., Banzatti, A., Gorti, U., et al. 2020, ApJ, 903, 78 51

Petersen, M. R., Stewart, G. R., & Julien, K. 2007, ApJ, 658, 1252 26

Petrov, P. P., Pelt, J., & Tuominen, I. 2001, A&A, 375, 977 82

Pfeil, T., & Klahr, H. 2019, ApJ, 871, 150 32

—. 2020, arXiv e-prints, arXiv:2008.11195 26, 32

Piétu, V., Dutrey, A., & Guilloteau, S. 2007, A&A, 467, 163 4, 62

Pinilla, P., Benisty, M., Cazzoletti, P., et al. 2019, ApJ, 878, 16 52

Pinte, C., Dent, W. R. F., Ménard, F., et al. 2016, ApJ, 816, 25 20

Pinte, C., Teague, R., Flaherty, K., et al. 2022, arXiv e-prints, arXiv:2203.09528 15, 17

Pinte, C., Price, D. J., Ménard, F., et al. 2020, ApJ, 890, L9 66

Piqueras, L., Conseil, S., Shepherd, M., et al. 2017, arXiv e-prints, arXiv:1710.03554 130

Podio, L., Bacciotti, F., Nisini, B., et al. 2006, A&A, 456, 189 55

Pollack, J. B., Hubickyj, O., Bodenheimer, P., et al. 1996, Icarus, 124, 62 9, 27

Proxauf, B., Öttl, S., & Kimeswenger, S. 2014, A&A, 561, A10 81, 84

Richard, Samuel and Nelson Richard P., and Umurhan Orkan M. 2016, MNRAS, 456, 3571 42, 112

Rigliaco, E., Pascucci, I., Gorti, U., Edwards, S., & Hollenbach, D. 2013, ApJ, 772, 60 52, 98

Rodenkirch, P. J., Klahr, H., Fendt, C., & Dullemond, C. P. 2020, A&A, 633, A21 51

Rosotti, G. P., Ilee, J. D., Facchini, S., et al. 2021, MNRAS, 501, 3427 66

Rüdiger, G., Arlt, R., & Shalybkov, D. 2002, A&A, 391, 781 23, 33

Schäfer, U., & Johansen, A. 2022, arXiv e-prints, arXiv:2208.08451 115

Schäfer, U., Johansen, A., & Banerjee, R. 2020a, A&A, 635, A190 31, 47

—. 2020b, Astronomy & Astrophysics Journal, 635, A190 115

Schmid, H. M., Bazzon, A., Roelfsema, R., et al. 2018, A&A, 619, A9 10

Shakura, N. I., & Sunyaev, R. A. 1973, A&A, 24, 337 20

Sheikhnezami, S., & Fendt, C. 2015, ApJ, 814, 113 82

—. 2018, ApJ, 861, 11 82

Sheikhnezami, S., Fendt, C., Porth, O., Vaidya, B., & Ghanbari, J. 2012, ApJ, 757, 65 51

Shu, F., Najita, J., Ostriker, E., et al. 1994, ApJ, 429, 781 31

Simon, M., Guilloteau, S., Di Folco, E., et al. 2017, ApJ, 844, 158 66

Simon, M. N., Pascucci, I., Edwards, S., et al. 2016, ApJ, 831, 169 22, 47, 51, 52, 55, 69, 81, 98

Smirnov-Pinchukov, G. V., Semenov, D. A., Akimkin, V. V., & Henning, T. 2020, A&A, 644, A4 107

Solf, J., & Boehm, K. H. 1993, ApJ, 410, L31 52

Soummer, R., Pueyo, L., & Larkin, J. 2012, ApJ, 755, L28 67

Squire, J., & Hopkins, P. F. 2018, MNRAS, 477, 5011 26

Stepanovs, D., & Fendt, C. 2016, ApJ, 825, 14 51

Stolker, T., Dominik, C., Avenhaus, H., et al. 2016, A&A, 595, A113 52

Stoll, M. H. R., & Kley, W. 2014a, A&A, 572, A77 24

—. 2014b, A&A, 572, A77 31

—. 2016, A&A, 594, A57 24

Stoll, M. H. R., Kley, W., & Picogna, G. 2017a, A&A, 599, L6 111

Stoll, M. H. R., Picogna, G., & Kley, W. 2017b, A&A, 604, A28 111

Suzuki, T. K., & Inutsuka, S.-i. 2009, ApJ, 691, L49 97

Teague, R., Bae, J., Bergin, E. A., Birnstiel, T., & Foreman-Mackey, D. 2018a, ApJ, 860, L12 17

Teague, R., Bae, J., Birnstiel, T., & Bergin, E. A. 2018b, ApJ, 868, 113 17

Terebey, S., Shu, F. H., & Cassen, P. 1984, ApJ, 286, 529 9

Tielens, A. G. G. M. 2005, The Physics and Chemistry of the Interstellar Medium 100, 101

Tobin, J. J., Sheehan, P. D., Megeath, S. T., et al. 2020, ApJ, 890, 130 10

Turner, N., Fromang, S., Gammie, C., et al. 2014, in Protostars and planets VI, ed. H. Beuther, R. Klessen, C. Dullemond, & T. Henning, Space science series (United States: University of Arizona Press), 411–432 31

Umurhan, O. M., Nelson, R. P., & Gressel, O. 2016a, A&A, 586, A33 24

Umurhan, O. M., Shariff, K., & Cuzzi, J. N. 2016b, ApJ, 830, 95 26

Urpin, V. 2003, Astronomy & Astrophysics, 404, 397 24

Valegård, P. G., Ginski, C., Dominik, C., et al. 2022, arXiv e-prints, arXiv:2209.01969 98

Wang, L., Bai, X.-N., & Goodman, J. 2019, ApJ, 874, 90 32, 47, 97, 108, 115

Ward-Thompson, D., & Whitworth, A. P. 2011, An Introduction to Star Formation (Cambridge University Press) 15

Wardle, M., & Koenigl, A. 1993, ApJ, 410, 218 97

Weilbacher, P. M., Streicher, O., & Palsa, R. 2016, MUSE-DRP: MUSE Data Reduction Pipeline, ascl:1610.004 52

Weilbacher, P. M., Streicher, O., Urrutia, T., et al. 2012, in Society of Photo-Optical Instrumentation Engineers (SPIE) Conference Series, Vol. 8451, Software and Cyberinfrastructure for Astronomy II, ed. N. M. Radziwill & G. Chiozzi, 84510B 52

Weilbacher, P. M., Streicher, O., Urrutia, T., et al. 2014, in Astronomical Society of the Pacific Conference Series, Vol. 485, Astronomical Data Analysis Software and Systems XXIII, ed. N. Manset & P. Forshay, 451 52

Weilbacher, P. M., Palsa, R., Streicher, O., et al. 2020, A&A, 641, A28 53

Wilms, J., Allen, A., & McCray, R. 2000, ApJ, 542, 914 101

Woitas, J., Ray, T. P., Bacciotti, F., Davis, C. J., & Eislöffel, J. 2002, ApJ, 580, 336 52

Xie, C., Haffert, S. Y., de Boer, J., et al. 2020, A&A, 644, A149 53, 67, 88

Yang, C.-C., & Johansen, A. 2014, ApJ, 792, 86 26

Yang, C.-C., Johansen, A., & Carrera, D. 2017, A&A, 606, A80 26

Youdin, A. N., & Goodman, J. 2005, ApJ, 620, 459 26

Zhu, Z., & Stone, J. M. 2018, The Astrophysical Journal, 857, 34 97

Zhu, Z., Stone, J. M., & Bai, X.-N. 2015, The Astrophysical Journal, 801, 81 21

Acknowledgements

"No self is of itself alone. It has a long chain of intellectual ancestors. The "I" is chained to ancestry by many factors ... This is not mere allegory, but an eternal memory."

by Erwin Schrödinger

First, I would like to express my deeply gratitude to my great supervisor Dr. Mario Flock, who made this possible. Dr. Mario Flock believed in my performance and encouraged me to do my best to achieve this huge accomplishment in my life. I dedicate this thesis to him. Thank you very much for having patience and great student-to-supervisor communication, which was a key to success during my Ph.D. career. I also could not have undertaken this journey without my defense committee with Prof. Dr. Andreas Quirrenbach for being part of my thesis referee, Simon Glover, and Luca Amendola. I am also grateful for my Ph.D. committee members with Prof. Cornelius Dullemond. Additionally, this endeavor would not be possible without the knowledge of Prof. Dr. Anna Pasquali. To my fantastic collaborator from Japan, Ryo Nakatani, for providing the photochemical network and useful discussions, and to all my other collaborators. Next, I want to thank Dr. Christian Fendt and Huong Witte-Nguy from the International Max Planck Research School for Astronomy & Cosmic Physics at the University of Heidelberg (IMPRS-HD) program for the great welcome and guidance before arriving in Germany and for the fun activities held during my Ph.D. years. I am very grateful to Prof. Dr. Thomas Henning for sharing his great knowledge during his last years as a director of the Planet and Star Formation (PSF) department at MPIA. To the Unveiling planet Formation by Observations and Simulations (UFOS) group composed of former postdoc Dr. Gesa H.M. Bertrang and the recently official Dr. Marcelo F. Barraza-Alfaro for the amazing support, especially, during the time we used to go for lunch together every single day (before Covid) and in the afternoon we used to go for coffee breaks.

I had the most fabulous time with my 14th IMPRS-HD generation with Jacob Isbell, Oliver Voelkel, Alina Boecker, Mischa Breuhaus, Francesco Conte, Christoph Engler, Caroline Gieser, Thomas Jackson, Gustavo Medina Toledo, Paz Bluhm, Ismael Pessa, Giancarlo Mattia, Theodoros Soultanis, Theodora Xylakis, and Vincent Carpenter, thank you to all for those moments we spent mostly during the first year of seminars and, after that, the gathering and suppers at the Zeughaus-Mensa in Marstall, and more. To my close fellows: Samantha Brown, Camille Bergez-Cassalou, Sofia Savvidou, Timmy Delage, Nicolas Kurtovic, Riccardo Franchescci, and Greg Smirnov-Pinchukov, for bringing useful research

discussions and presentations as well as emotional support during our group meetings and extracurricular activities. I am also profoundly grateful to Bertram Bitsch, Dimitry Semenov, and Paola Pinilla for their excellent guidance toward us. To my chileans friends, whom I met in Heidelberg, who were very nice and supportive during the *fiestas*.

This work would not be possible if it were not for my peers and colleagues from Puerto Rico. To Yese Felipe, Ariana Beltran, Karimar Ledesma, and Alexander Rodriguez for their strong friendship and support throughout my professional career. Most importantly, to my beloved family, including my parents, sisters, nephews, and my pets, Choco and Poly, who are in Puerto Rico, for their trust, communication, comprehension, and love during my Ph.D. years. To my incredible former supervisors: Dr. Juan G. Gonzalez, Dr. Susan Terebey, and Dr. Neal Turner, for their professional guidance and example. Last but definitely not least, I would like to express my deepest gratitude to my boyfriend Nicolas Kurtovic, for all his love, professional knowledge, and emotional support towards me. Thank you for being a role model and for making me laugh every single time we are together.

Lastly, I would like to extend my sincere thanks the *European Research Council (ERC)* project under the European Union's Horizon 2020 research and innovation programme number 757957. I would also like to acknowledge Andrea Mignone for the creation of the publicly available package PLUTO (Mignone, 2007), the matplotlib team (Hunter, 2007) for the good quality tool in order to better visualize the data. To Piqueras et al. (2017) for the mpdaf software to analyze the MUSE data.

Declaration of Originality

Declaration of Originality

I hereby declare that this thesis is my own work and that I have used no other than the stated sources and aids.

Declaration

Ich versichere, dass ich diese Arbeit selbstständig verfasst habe und keine anderen als die angegebenen Quellen und Hilfsmittel benutzt habe.

Heidelberg, der 19. September 2022

Lizxandra Flores-Rivera